

**INVESTIGATION OF OPTICAL PROPERTIES OF POLYMETHINES
FOR POTENTIAL APPLICATION IN ALL-OPTICAL SIGNAL
PROCESSING**

A Dissertation
Presented to
The Academic Faculty

by

Hyeongeu Kim

In Partial Fulfillment
of the Requirements for the Degree
Doctor of Philosophy in the
School of Chemistry and Biochemistry

Georgia Institute of Technology
May 2015

COPYRIGHT 2015 BY HYEONGEU KIM

**INVESTIGATION OF OPTICAL PROPERTIES OF POLYMETHINES
FOR POTENTIAL APPLICATION IN ALL-OPTICAL SIGNAL
PROCESSING**

Approved by:

Dr. Joseph W. Perry, Advisor
School of Chemistry and Biochemistry
Georgia Institute of Technology

Dr. Angus P. Wilkinson
School of Chemistry and Biochemistry
Georgia Institute of Technology

Dr. Robert M. Dickson
School of Chemistry and Biochemistry
Georgia Institute of Technology

Dr. Kenneth R. Brown
School of Chemistry and Biochemistry
Georgia Institute of Technology

Dr. Rick Trebino
School of Physics
Georgia Institute of Technology

Date Approved: 03/27/2015

To my parents and my brother

ACKNOWLEDGEMENT

First and foremost, I would like to thank sincerely my PhD advisor, Dr. Joseph Perry for accepting me into his group when I was a budding, yet, underqualified young scientist back in December 2008. I would owe my deepest gratitude for his continuous support of my doctoral research, advice over the years (both academic and life-related), mentorship, enthusiasm, knowledge, patience, and most importantly his understanding.

I would also like to thank all my thesis committee members: Dr. Ken Brown, Dr. Jean-Luc Brédas, Dr. Angus Wilkinson, Dr. Rick Trebino, and Dr. Rob Dickson for all the questions, and scientific discussions over the years, and most importantly, their genuine care for the interests of the students like myself.

I would like to thank especially Dr. Joel Hales and Dr. Sarah Chi for their mentorship, training, and friendship without which I would not have been able to complete this doctoral research. I also extend my gratitude to Dr. O'neil Smith, Luke Johnstone, Dr. Canek Fuentes, and Dr. Anthony Giordano who have, at one point or another, helped me with the work contained in this thesis.

I would also like to extend my appreciation to all my collaborators including Dr. Yulia Getmanenko, Dr. Zhong'an Li, Dr. Robert Norwood and Dr. Seth Marder. Without their collaborative efforts, this thesis would not have been possible.

My thanks also goes to the current and former members of the Perry group including Dr. Ariel Marshall, Dr. Yunsang Kim, Luke Johnstone, John Tillotson, Taylor Allen, Dr. Mohan Kathaperumal, Dr. Vincent Chen, Dr. Nathan Jarnagin, Dr. Matt Sartin, Dr. Wojtek Haske, and Mr. Matteo Cuzzoul whose friendship had been vital in making this journey as enjoyable as it has been.

I would also like to thank the long-time friends from Georgia Tech including Dr. Michael Bayless, Dr. Ariel Marshall, Dr. Megan Lydon, Dr. Matt Hagy, Dr. Emily Herman, Dr. Amy Jablonski, Dr. O'neil Smith, and Mr. Marshall Johnson.

Lastly, I would like to thank sincerely my family who has been extremely supportive and encouraging throughout this journey.

TABLE OF CONTENTS

	Page
ACKNOWLEDGEMENTS	iv
LIST OF TABLES	x
LIST OF FIGURES	xii
LIST OF SYMBOLS AND ABBREVIATIONS	xvi
SUMMARY	xvii
S.1 References	xix
<u>CHAPTER</u>	
1 Introduction	1
1.1 Conventional Means of Optical Signal Transmission and Processing	2
1.1.1 Si-based Optical Devices and their Limitations	2
1.1.2 Organic Materials in All-Optical Signal Processing Applications	4
1.2 Material Figures-of-Merit for Nonlinear Refractive Index based AOS	6
1.2.1 Mach-Zehnder Interferometer and Nonlinear Phase Shift	6
1.2.2 The Limits Imposed on $\Delta\phi$ and the Associated Figures-of-Merit	8
1.3 $\chi^{(3)}$ Response of π -Conjugated Organic Materials	10
1.4 Strategy for Implementaion: Silicon-Organic Hybrid Approach	14
1.5 Aim and Organization of the Thesis	19
1.6 References	21
2 Third-Order Optical Responses and the Characterization Techniques	28
2.1 Third-Order Polarizability	29
2.1.1 Macroscopic Electric Susceptibility	29

2.1.2	Microscopic Molecular Polarizability	31
2.1.3	Relationship between γ and $\chi^{(3)}$	33
2.1.4	Units of γ and $\chi^{(3)}$	34
2.2	Characterization Methods	35
2.2.1	Prism Coupling	35
2.2.2	Z-scan	39
2.2.3	Femto-second Transient Absorption Spectroscopy	43
2.2.4	Non-degenerate Two-photon Absorption Spectroscopy	45
2.3	References	49
3	Polymethines with Large Nonlinear Refractive Index, Low Linear and Nonlinear Optical Loss in Near Infrared	51
3.1	Introduction	51
3.1.1	Spontaneous Symmetry-breaking	52
3.1.2	Aggregaton	53
3.2	Effects of Metallation on the Optical Properties of <i>bis</i> (dioxaborine) (DOB) Polymethines	55
3.2.1	Linear Optical Properties	57
3.2.2	Nonlinear Optical Properties	59
3.3	Effects of Out-of-Plane Steric Bulk Substitution on the Optical Properties of Chalcogenopyrylium-terminated Heptamethines	61
3.3.1	Linear Optical Properties	65
3.3.2	Nonlinear Optical Properties	70
3.4	Effects of Square-planar “Front” Substitutions on the Optical Properties of Chalcogenopyrylium-terminated Heptamethines	73
3.5	Summary	78
3.6	Experimental Details	79
3.6.1	Synthesis of Polymethines	79

3.6.2	Film Preparation	80
3.6.3	Characterization of Linear Absorption, Refractive Index, and Linear Optical Loss	80
3.6.4	Nonlinear Optical Characterization Technique	81
3.7	References	83
4	Anionic Polymethines with Varying Counterions for Enhanced Compatibility with Host Polymer	86
4.1	Introduction	86
4.2	Effects of Various Counterions on the Optical Properties of TCF-terminated Heptamethine-Amorphous Polycarbonate (APC) Blend Film	89
4.2.1	Linear Optical Properties	89
4.2.2	Nonlinear Optical Properties	93
4.2.3	SOH Application	96
4.3	Effects of Multiply-charged Counterions on Optical Properties of TCF-terminated Polymethines	97
4.3.1	Linear Optical Properties of TCF-heptamethine/Multi-cation Counterion Pairs	99
4.3.2	Molecular Nonlinearities of TCF-heptamethine/Multi-cation Counterion pairs	105
4.3.3	Macroscopic Nonlinearities of TCF-heptamethine/Multi-cation Counterion Pairs	109
4.4	Summary	110
4.5	Experimental Details	112
4.5.1	Preparation of Guest-host Films	112
4.5.2	Refractive Index and Linear Optical Loss	112
4.5.3	Two-photon Induced Fluorescence (TPIF)	113
4.6	References	115

5	Implementation of Polymethine-Host Polymer Blends in Silicon-Organic Hybrid (SOH) Constructs	117
5.1	Introduction	117
5.1.1	Numerical Aperture of Waveguides and Single-mode Propagation	117
5.1.2	Solution-Processing of Organic Cladding	118
5.2	Linear Dispersion Behaviors and Optical Nonlinearities of Host Polymers and Dye/APC Guest-Host Film	119
5.2.1	Dispersive Behaviors of Neat APC, PMMA, and a Dye-doped Polymer Blend	120
5.3	Improving Cladding Infiltration via Substrate Surface Modification	127
5.3.1	Surface Modification	128
5.3.2	Characterization of Functionalized Surfaces	130
5.4	Summary	139
5.5	Experimental Details	140
5.5.1	Preparation of Blade-cast Thick Films for Ellipsometry	140
5.5.2	Prism Coupling Experiments on Thin Films	140
5.5.3	Preparation of Functionalized Surfaces	140
5.5.4	Characterization Techniques for Functionalized Surfaces	141
5.6	References	142
6	Conclusions and Future Outlook	145
6.1	References	147
APPENDIX	A.1 Third-Order Susceptibilities of Amorphous Polycarbonate	148
	A.2 Third-Order Nonlinearities of Various Solvents in Liquid-core Optical Fibers (LCOF)	149
	A.3 References	152
VITA		153

LIST OF TABLES

	Page
Table 2.1: Nonlinear optical properties of references at 1.55 μ m	40
Table 3.1: Linear and nonlinear optical properties of A1-3	59
Table 3.2: Linear and nonlinear ^a optical properties of chalcogenopyrylium-terminated heptamethines at 1550 nm in chloroform and in films (50 wt% in APC unless otherwise stated)	69
Table 3.3: Linear and nonlinear ^a optical properties of <i>Bis</i> (triphenylphosphine) – palladium substituted heptamethines at 1550nm in chloroform and in 50 wt% films	76
Table 4.1: The linear and nonlinear optical properties at 1.55 μ m of thick guest-host APC films doped with 50 wt.% polymethine salt	92
Table 4.2: Molecular nonlinearities of 6.0~6.5 mM A2-A5 in DCM at 1550 nm	94
Table 4.3: Comparison of relative oscillator strengths (<i>f</i>) and extinction coefficients per chromophore of C1 , C2 , and C6 at dilute and concentrated solutions	101
Table 4.4: The molecular third-order polarizabilities of dyes measured in diluted and concentrated CHCl ₃ solutions using the femtosecond pulsed Z-scan method at 1.3 μ m	105
Table 4.5: The molecular third-order polarizabilities of dyes measured in diluted and concentrated CHCl ₃ solutions using the femtosecond pulsed Z-scan method at 1.55 μ m	105
Table 4.6: The molecular third-order polarizabilities of dyes measured in diluted and concentrated CHCl ₃ solutions using the femtosecond pulsed Z-scan method at 1.3 μ m.	109
Table 4.7: The molecular third-order polarizabilities of dyes measured in diluted and concentrated CHCl ₃ solutions using the femtosecond pulsed Z-scan method at 1.55 μ m.	109
Table 5.1: Refractive indexes of neat APC, poly(methyl methacrylate) (PMMA), and 50 wt% B6 /APC film determined using prism coupling	122
Table 5.2: Cauchy and Sellmeier coefficient using single-term expressions	126
Table 5.3: Cauchy and Sellmeier coefficient using the conventional forms	126

Table 5.4: Thicknesses of the self-assembled layers of the silane coupling agents on SiO ₂ substrate	131
Table 5.5: Root mean square (RMS) surface roughness, and phase of the bare, and PB modified substrate from AFM images	135
Table 5.6: Critical surface tensions of different substrate surfaces	136
Table A.1: Third-order nonlinearity of neat APC host polymer	149
Table A.2: Intensity-dependent refractive indexes and corresponding $\text{Re}(\chi^{(3)})$ s of solvents used in LCOF demonstration	150

LIST OF FIGURES

	Page
Figure 1.1: Examples of π -conjugated organic materials previously investigated for AOSP applications; clockwise from the top right: squaraine, substituted polythiophene, <i>p</i> -toluenesulfonyl diacetylene (pTS), and substituted poly(<i>p</i> -phenylenevinylene).	5
Figure 1.2: Nonlinear Mach-Zehnder interferometer (MZI) performing switching functions via cross-phase modulation.	7
Figure 1.3: Huckel molecular orbital diagram and the corresponding energy of a) butadiene, and b) pentadienyl anion	10
Figure 1.4: A plot of third-order polarizability (second hyperpolarizability) vs. the degree of charge separation in two-resonant structures of polyene and the corresponding bond-length alternation.	11
Figure 1.5: State-energy schematics of a) polyenes with the twice the excitation energy, $2\hbar\omega$, below the two-photon resonance, E_{ge} , and b) cyanine-type molecules with $\hbar\omega$ lying just below E_{ge} , and $2\hbar\omega$ positioned in between $E_{g\text{ }vb}$ and E_{ge} , two-photon resonances.	12
Figure 1.6: SEM micrographs of single-mode $4 \times 4 \mu\text{m}$ perfluoropolymer channel waveguide.	15
Figure 1.7: Cross-section of a silicon-organic hybrid strip waveguide.	16
Figure 1.8: Simulation of E_x in SOI showing mode profile with normalized field amplitudes: a) conventional strip waveguide b) slot waveguide.	17
Figure 2.1: Oscillatory motion of the electron cloud in response to an applied electric field.	29
Figure 2.2: The effects of an induced phase change (illustrated in the samples) on incident phase fronts.	32
Figure 2.3: a) Simplified diagram of a prism coupler. A thin film is pressed against a face of a prism via pneumatically-operated coupling head (not shown). b) Plot of percent intensity vs. mode index, a function of the incidence angle and the refractive index of the prism.	36
Figure 2.4: a) Prism coupler in loss measurement mode, b) intensity vs distance pattern; the large intensity drop in the first ~ 150 steps (0.75cm) caused by extraneous light scattering near the prism can be mitigated by installing a loss shield.	38

Figure 2.5: Simplified schematic of Z-scan experiment:	39
Figure 2.6: Examples of Z-scan data and the corresponding fitting functions. (left) Open aperture data of 410 μ m GaAs; (right) closed aperture data of 1mm fused SiO ₂ .	41
Figure 2.7: The layout of the pump-probe transient absorption and ND-2PA spectroscopy	44
Figure 3.1: Example of spontaneous symmetry breaking in pyridinium tridecamethine.	52
Figure 3.2: a) H- and b) J- aggregation bands in benzimidazolecarbocyanines induced using two different ionic liquids.	54
Figure 3.3: The chemical structures of bis(2,2'-bipyridyl dioxaborine)heptamethines. A1: model compound, A2: rhodium-terminated, and A3: iridium-terminated	56
Figure 3.4: Normalized linear absorption spectra of a) A1, b) A2, and c) A3 in CH ₂ Cl ₂ (dashed) and in neat films (solid).	58
Figure 3.5: Transient absorption spectrum of A1 in CH ₂ Cl ₂ ; the sample concentration, 9.3 μ M; the pump wavelength, 830 nm; pump energy, 4.1 μ J.	60
Figure 3.6: M_{ge} vs L (top) and E_{ge} vs 1/L (bottom) for symmetrically substituted polymethines with various terminal groups.	62
Figure 3.7: Rigid steric group substitution scheme for chalcogenopyrylium-terminated polymethines.	64
Figure 3.8: Normalized absorption spectra of chalcogenopyrylium heptamethines in a) dilute chloroform solution and b) in 50 wt% blends with amorphous polycarbonate (APC)	65
Figure 3.9: Linear absorption spectra of neat films (solid) and 50 wt% dye-APC blends (dashed)	67
Figure 3.10: Closed (following the division by open aperture scan) and open aperture Z-scans of selected 50 wt% dye/APC blends at 1550nm	72
Figure 3.11: Structures of <i>bis</i> (triphenylphospine)palladium-modified (left) thiopyrylium and (right) <i>bis</i> (benzoindole)thiopyrylium polymethines.	74
Figure 3.12: Normalized linear absorption spectra of 50 wt% dye/APC blend films	77
Figure 4.1: Chemical and DFT optimized structure of tricyanofuran-terminated heptamethines: a) crystal packing in presence of a small dimeric cation (Na ⁺ shown) b) <i>syn</i> - conformer c) <i>anti</i> - conformer.	87

Figure 4.2: Structures of various counterions paired with TCF-terminated heptamethines	89
Figure 4.3: The absorption spectra of polymethines in (a) dilute DCM solutions (concentration of $\sim 2 \times 10^{-6}$ M) and (b) thin guest-host APC films doped with 50 wt% of chromophores	89
Figure 4.4: Optical transmission micrographs of thick guest-host APC films doped with 50 wt% of polymethine salt under different magnifications.	91
Figure 4.5: Prism coupling intensity plots for thick (~ 1.5 μm) guest-host APC films doped with 50 wt.% polymethine salts	92
Figure 4.6: Left: non-degenerate two-photon absorption (ND-2PA) spectra of 5.4mM A3 in chloroform overlaid with the degenerate TPA cross-sections, δD , (1 GM = 10-50 cm ⁴ s photon ⁻¹) obtained from Z-scan. Right: 50 wt. % A3: APC film overlaid with TPA coefficients, β . The dashed line represents linear absorption.	95
Figure 4.7: a) Calculated optical mode pattern for TE ₀ mode of the asymmetric slot waveguide. b) SEM micrograph of the cross-section showing 100 and 310 nm width silicon rails with 180 nm slot	96
Figure 4.8: Optical spectrum showing idler wavelength generated by near-degenerate four wave mixing in silicon organic hybrid slotted waveguide device coated with 25 wt.% A3 in amorphous polycarbonate.	97
Figure 4.9: Structures of TCF-polymethines and the counterions	98
Figure 4.10: Normalized Vis-NIR spectra of dyes in CHCl ₃	101
Figure 4.11: Normalized Vis-NIR spectra of C1, C2, and C6 in toluene	102
Figure 4.12: Normalized Vis-NIR spectra of C1, C2, and C6 in neat films	103
Figure 4.13: Overlay of linear absorption and two-photon absorption spectra C1 , C2 , and C6 , obtained using two-photon induced fluorescence and Z-scan on 5mM (per molecule basis) solutions in chloroform.	109
Figure 5.1: Structure of B6 , a modified thiopyrylium-terminated heptamethine	121
Figure 5.2: Dispersion curves of neat host polymer ca. 2 μm thick a) APC, and b), generated using a least square fit of the measured indexes to Cauchy's and Sellmeier's equations, and spectral ellipsometry.	123

Figure 5.3: Dispersion curves of c) 50 wt% B6 /APC film ca. 1.2 μm thick, generated using a least square fit of the measured indexes to Cauchy's and Sellmeier's equations, and spectral ellipsometry. d) Plot of the real and imaginary part of complex refractive index, n (blue) and k , (red) respectively, generated using effective medium approximation	124
Figure 5.4: Cross-sectional SEM images of polymer clad waveguides	128
Figure 5.5: Structures of alkoxy coupling silane agents	128
Figure 5.6: Structure of amorphous polycarbonate (APC) and the binding of PB on silica substrate	129
Figure 5.7: XPS spectra of fused SiO_2 surface modified with PB and PM layers	131
Figure 5.8: AFM topographical (left) image and phase image (right) from a $5 \times 5 \mu\text{m}$ area of a) oxygen-plasma etched, and b) benzoylpropyl trimethoxysilane (PB) modified fused silica substrate measured using amplitude-modulation mode	133
Figure 5.9: AFM topographical (left) image and phase image (right) from a $1 \times 1 \mu\text{m}$ area of a) oxygen-plasma etched, and b) benzoylpropyl trimethoxysilane (PB) modified fused silica substrate measured using amplitude-modulation mode	134
Figure 5.10: Images of distilled water droplets on various surfaces taken using contact-angle goniometer	136
Figure 5.11: Optical micrographs of 50% wt. dye-APC blend cast on a) unmodified SiO_2 substrate, and b) 3-benzoylpropyl trimethoxysilane (PB) functionalized substrate.	138
Figure A.1: 5 μm thick melt-processed APC disk used for Z-scan measurements	148
Figure A.2: Closed (following the division by open aperture scan) and open aperture Z-scans of 5 μm thick melt-processed APC disc 1550nm	149
Figure A.3: Closed aperture Z-scans of various solvents	151

LIST OF SYMBOLS AND ABBREVIATIONS

β	two-photon absorption coefficient	
		mode index
		second-order polarizability
δ	two-photon absorption cross-section	
n_2	intensity dependent refractive index	
γ	third-order polarizability (atomic/molecular quantity)	
$\Delta\varphi$	differential (or induced) phase shift	
$\chi^{(3)}$	third-order susceptibility (material quantity)	
2PA or TPA	two-photon absorption	
Ad	adamantyl-	
AOS	all-optical switching	
AOSP	all-optical signal processing	
BLA	bond length alternation	
FCA	free-carrier absorption	
FOM	figure-of-merit	
M_{ij}	transition dipole moment (between states i and j)	
NA	numerical aperture	
ND	non-degenerate	
NLO	nonlinear optical	
Ph	phenyl-	
tBu	<i>tert</i> -butyl-	

SUMMARY

While silicon has traditionally been a popular choice of material for photonic circuits due to its large refractive index and transparency in the telecommunication wavelengths, demonstration of ultrafast all-optical signal processing (AOSP) using silicon as the active material has been limited by large two-photon absorption loss and long lifetimes of the resulting free carriers. For all-optical signal processing at speeds in the terahertz, an order of magnitude faster than that the fastest current electronic counterpart,[1, 2] a class of π -conjugated organic molecules called polymethines provides a promising alternative to silicon as they possess large third-order nonlinearities, and ultrafast polarization response to an incident field. In this work, the linear and nonlinear optical properties of various polymethines have been characterized extensively for elucidation of ideal molecules for phase-based AOSP. Moreover, the unique challenges associated with translating their molecular properties into bulk material properties and integrating these materials in silicon-organic-hybrid systems have been addressed.

First, molecules' resistance to deleterious spontaneous symmetry breaking and aggregation was enhanced. The metallation of the terminal groups of *bis*(dioxaborine)-(DOB) cyanines causes bathochromic shifts in the linear absorption spectra and results in one- and two-photon dispersion enhancement. This approach provides a method to extend the effective conjugation length without extending the physical length of the molecule, thereby circumventing the risks of spontaneous symmetry breaking. The substitution of

rigid steric groups above and below the π -conjugated plane of polymethine chain prevented the deleterious effects of aggregation: namely, linear and two-photon absorption loss, and reduction in $\text{Re}(\chi^{(3)})$. Chalcogenopyrylium polymethines with rigid out-of-plane steric substituents at multiple sites along the chain were found highly effective at resisting aggregation in solid-state, as demonstrated by the drastic improvement in linear absorption spectra, and the unprecedentedly high two-photon figure-of-merit, $|\text{Re}(\chi^{(3)})/\text{Im}(\chi^{(3)})|$, of the films. Guest-host polymer blends using these chromophore possess a unique combination of large $\text{Re}(\chi^{(3)})$, low linear and two-photon absorption loss, and processability.

In addition, the optical quality of the polymethine-containing polymer films was drastically improved by modifying the counterions of polymethine salts for stronger solid-state miscibility with the host polymer. Specifically, the polymethine salts containing polarizable aryl based counterions with diffuse electrons and moderate ground state dipole moment resulted in a highly homogeneous solid-state mixture in the host amorphous polycarbonate (APC) polymer. The resulting dye-polymer blend film showed a significant reduction in the linear absorption loss, motivating its integration into a slot waveguide. The magnitude of the third-order susceptibility, $|\chi^{(3)}|$, of the polymethines-clad slot waveguide showed a good agreement with the $|\chi^{(3)}|$ of the thin film on a featureless slab waveguide, and that extrapolated from the molecular third-order polarizability, γ .

The use of multiply-charged counterions in polymethine salts results in constraints on the orientations of the chromophores in low-dielectric screening media, and by extension, the

electronic configuration of the molecules. The localized ion-pairing between the chromophores and multiply-charged counterions limits the effects of intermolecular chromophore-chromophore interaction as evidenced by the lack of change in the linear and nonlinear optical properties over a range of concentrations.

To enable engineering of the waveguide dimensions for single mode propagation in silicon-organic-hybrid (SOH) constructs, the dispersion curves of the neat polymers and dye-containing polymer blends were generated using prism coupling and ellipsometry. The dispersion curves in the near-infrared wavelengths determined by Cauchy and Sellmeier modeling of indexes from prism coupling are in a good agreement with the dispersion obtained by applying effective medium approximation on the ellipsometric data. For facile integration of the promising organic materials into SOH, the substrate surface was functionalized with a silane coupling agent containing compatibilizing moiety. The presence of a monolayer of this surface modifier greatly reduced the surface energy mismatch between the film and the substrate, and allowed for improved wetting, coverage and infiltration of the organic film onto the substrate containing microfeatures.

S.1. References

1. Lin, Y.-M., et al., *100-GHz Transistors from Wafer-Scale Epitaxial Graphene*. Science, 2010. **327**(5966): p. 662.
2. Alloatti, L., et al., *42.7 Gbit/s electro-optic modulator in silicon technology*. Optics Express, 2011. **19**(12): p. 11841-11851.

CHAPTER 1

INTRODUCTION

Optical fiber is the preferred means of data transmission for bit rates over a few tens of megabits per second, and distances over a kilometer. As the global IP traffic has been estimated to have reached over 62×10^{18} bytes per month,[3] conventional copper cables in many homes are rapidly being replaced by optical fibers. The signals transmitted over these optical fibers, however, do not stay in the optical domain for the duration of their travel from the transmitter to receiver. The optical signals are passed through electronic devices that process their headers and rerouted to appropriate output ports.[4] In addition, the destinations of these optical signals are most often modern computational tools that operate in the electrical domain. Thus, the conversion of the optical signals to electrical signals, a costly process that requires an input of energy, is unavoidable. An all-optical signal processing (AOSP) device such as an all-optical switch (AOS) can eliminate the need for this conversion altogether, allowing for the reduction in cost and delays in networking. It also offers potential for terahertz operation speed, an order of magnitude faster than the fastest-known electronic counterpart to-date.[1, 2] Finally, all-optical switches serve as a crucial building block for other optical logic elements and optical computing.

As with any other switch, an optical switch either interrupts or diverts transmission of signals; the signals are just in the form of photons, rather than electrons. The difficulty in building an all-optical switch – a device that allows one optical signal to control the transmission of another optical signal – is in the fact that photons normally behave as

non-interacting particles. While this is great for transmitting the signal over long distances as the signals will be insensitive to the environmental disturbances,[5] performing switching function on these signals would prove to be a challenging endeavor as it requires the use of nonlinear optical (NLO) media that would permit light-matter interactions to mediate the control of a photon with another photon.

There are a number of nonlinear optical phenomena that can be exploited to facilitate AOS; some involve optical gain (e.g., stimulated emission /induced transparency),[5, 6] others take advantage of optical loss (e.g., TPA/ stimulated Raman scattering).[7, 8] In this thesis, the NLO process of primary focus for AOS application will be nonlinear refraction since, under ideal conditions, this phenomenon can circumvent the problems associated with dissipation of energy in the medium unlike the absorptive or Raman scattering processes.

1.1 Conventional Means of Optical Signal Transmission and Processing

1.1.1 Si-based Optical Devices and their Limitations

The information in the optical domain is carried by an optical waveguide made of a “passive” material that does not alter the signal significantly. The most obvious example of such waveguide is an optical fiber, consisting of metal-oxide doped silica core and ultrapure silica cladding.[9] While silica derivatives are a common choice for both core

and cladding for their low loss-transmission, immunity to electromagnetic interference, ease of integration and low material cost, the diameter of these fibers is limited to a few orders of the wavelength ($> 10 \mu\text{m}$) of the light being carried due to a relatively small refractive index mismatch, rendering them unsuitable for miniaturization of photonic/optical circuits. Hence, waveguiding in submicron regime has been most frequently facilitated by crystalline silicon which exhibits a high refractive index and near- to mid-infrared transparency. In a widely used “silicon-on-insulator” (SOI) configuration of crystalline Si, light in telecommunication wavelength ($1.3\sim 1.55 \mu\text{m}$) can easily be confined down to $< 0.2 \mu\text{m}^2$ in the effective mode area - while maintaining single mode propagation for minimal modal dispersion.[10, 11] The propagation loss through the crystalline Si at this wavelength is also sufficiently low, making it an ideal waveguiding platform for miniaturized devices.

Silicon, while effective at confining and guiding light at the nanoscale, is also known to show non-negligible nonlinear optical responses at telecommunication wavelengths – namely, nonlinear refraction (optical Kerr effect), two-photon absorption (TPA or 2PA), free carrier plasma dispersion, and free carrier absorption (FCA).[12-15] This has led to numerous efforts to exploit Si, not only as a “passive” transmission medium, but as an “active” medium for signal processing, leading to an independent area of research termed silicon nanophotonics. Various designs of the Si-based active all-optical and electro-optical devices have been demonstrated since the late-80s, including amplifiers, photodetectors, demultiplexers, and modulators.[8, 16-21] However, most of these designs suffer one or more shortcomings that hamper fluid integration of Si into compact photonic circuits including, 1) large size due to its relatively weak nonlinear refraction,

and the weak dependence of refractive index on free carrier concentration, 2) slow speed of operation due to the long lifetime associated with the free carriers generated either by TPA (≈ 1 ns), or introduced by Group III/V dopants, 3) elaborate fabrication process often associated with doping of Si to overcome the indirect nature of Si band gap, 4) the requisite use of auxiliary tools such as visible light source to induce sufficient refractive index change,[21-23] or an external voltage source to deplete the buildup of free carriers.[18] In addition, at the typical irradiances required for inducing nonlinear optical responses in Si, substantial TPA[24] and the subsequent two-photon generated FCA incur moderate to severe propagation loss, and concomitant reduction in maximum data rate.[25, 26] Hence, there exists a strong demand for both novel materials and device architectures that would allow for fast and efficient nonlinear optical response while avoiding the losses intrinsic to silicon.

1.1.2 Organic Materials in All-Optical Signal Processing (AOSP) Applications

Because of the aforementioned shortcomings with silicon and silicon derivatives, much of the research efforts in the last two decades have been focused on identifying and characterizing materials with high optical nonlinearity, low optical loss (both linear and nonlinear), and ultrafast nonlinear response for AOSP applications. Organic materials with highly delocalized π electrons (**Figure 1.1**) have been gaining attention as potential candidates that can fulfill these requirements.[27-29]

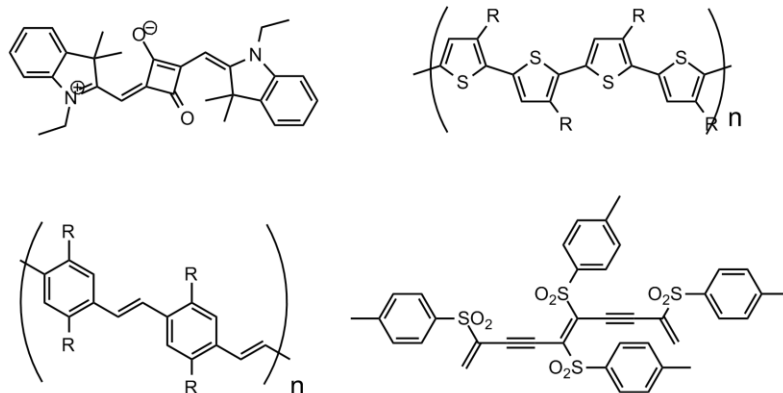


Figure 1.1. Examples of π -conjugated organic materials previously investigated for AOSP applications; clockwise from the top right: squaraine, substituted polythiophene, *p*-toluenesulfonyl diacetylene (pTS), and substituted poly(*p*-phenylenevinylene).

There are numerous advantages in using the π conjugated organic materials for AOSP over the conventional semiconductors and inorganic dielectrics. First, the nonlinear optical responses in the π -conjugated systems are of electronic origin, hence the response time is automatically faster than the duration of optical bits required for terahertz operation ($<10^{-13}$ s).[28, 30] Second, because of the strong coupling of the oscillators (excitons, electrons, and holes) across the lengths of the molecule, many π conjugated organics exhibit substantially larger nonlinearities than silicon. Materials such as cyanines, squaraines, phthalocyanines, porphyrins, polydiacetylenes, polyarylenes vinylenes, polythiophenes, and polyanilines[30-37] have shown third-order susceptibilities, $\chi^{(3)}$, a measure of nonlinear response, exceeding that of Si by four-fold in the non-resonant regime, and up to 5 orders of magnitude greater near resonance.[30] Third, organic materials often offer simplified routes of fabrication via solution processing as many of the earliest characterizations of third-order nonlinearities in polymers were performed on the films cast from solutions.[31, 38] Lastly, the well-

established methods of synthetic modification for organics allow for facile tuning of their key molecular and bulk material properties including the strengths and positions of one and two-photon electronic resonances, the overall magnitude of third-order optical response, the propensity for aggregation or a particular molecular orientation, and the compatibility with another medium.

1.2 Material Figures-of-Merit for Nonlinear Refractive Index Based AOS

In order to gauge quantitatively the applicability of candidate organic materials, it is necessary to define the material figures-of-merit (FOM) for AOS. A simple switching scheme is described in this section to illustrate the basic requirements for an active optical material, and the pertinent parameters involved.

1.2.1 Mach-Zehnder Interferometer and Nonlinear Phase Shift

Upon exposure to intense light, all materials can experience an increase or a decrease in their refractive indexes. This change in refractive index induces a phase lag in the field propagating through the medium. Thus, with suitable device geometry, it is possible to control the interference pattern of two or more fields, effectively allowing for the modulation of a beam using another beam. Mach-Zehnder interferometer (MZI), and nonlinear loop mirrors (NOLM) are examples of such devices.[39-42] In a traditional MZI, the difference in the path lengths of the split beams causes one of them to

experience a phase lag relative to the other one. When the two beams emerge, they add either in or out of phase, resulting in a single outbound beam with either amplified or attenuated amplitude. This phenomenon can be used to create an all-optical switch; but instead of using the difference in the physical path lengths, one can incorporate a nonlinear optical material into one of the channels. (**Figure 1.2**) When a separate control pulse is applied to this NLO material, it causes a change in its refractive index which, in turn, produces the necessary phase shift for the propagating signal.

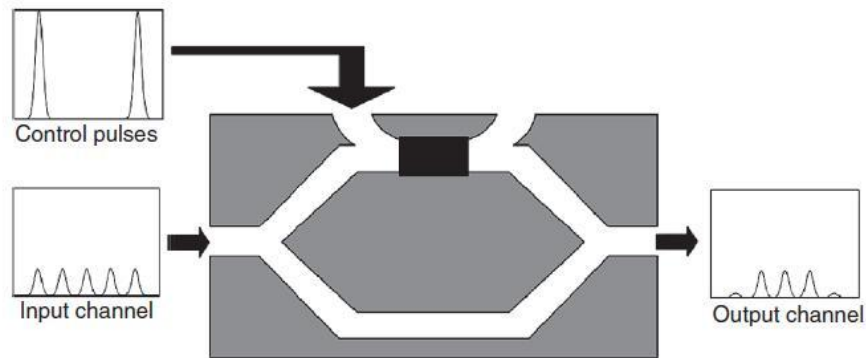


Figure 1.2. Nonlinear Mach-Zehnder interferometer (MZI) performing switching functions via cross-phase modulation. Reprinted with permission from the authors [43] (Copyright 2011 © CRC Press).

For efficient operation and ease of miniaturization, the change in refractive index of the NLO material in the presence of the control pulse should be as large as possible for telecommunication wavelengths. To obtain the material parameters responsible for nonlinear refraction, the overall refractive index of the NLO material is expressed in terms of static and intensity-dependent refractive indexes,

$$n(\lambda, I) = n_0(\lambda) + n_2(\lambda)I \quad (\text{Eq. 1.1})$$

where both n_0 and n_2 , are functions of the incident field frequency. Assuming that the control pulse is close to monochromatic, and that the signal beam is either much weaker than the control pulse, or exhibits a top-hat profile in intensity,ⁱ the overall induced phase shift, $\Delta\phi$, can then be expressed simply using the irradiance of the control pulse, I , the intensity-dependent refractive index, n_2 , and the propagation length in the medium, L . [44, 45]

$$\Delta\phi(\lambda, I) = k_0 \Delta n L = \frac{2\pi}{\lambda} n_2(\lambda) I L \quad (\text{Eq. 1.2})$$

Since the wavelength of the control pulse, λ , and the propagation length through the nonlinear medium are often predefined, $\Delta\phi$ can be construed predominantly as a function of the pulse intensity of the control beam.

1.2.2 The Limits Imposed on $\Delta\phi$ and the Associated Figures-of-Merit

Under the approximation that the optimal $\Delta\phi$ for a complete destructive interference in MZI is π ,ⁱⁱ Stegeman et al. investigated cases where the maximum differential phase shift is limited by the linear and nonlinear absorption losses. From these case studies, they were able to establish the following inequalities to describe the one- and two-photon figures-of-merits (2PA-FOM) for NLO materials, [39, 46, 47]

$$W = \frac{n_2 I}{\alpha_0 \lambda} > 1 \text{ and } T = \frac{\beta \lambda}{n_2} < 1 \quad (\text{Eq. 1.3})$$

ⁱ to avoid the effects of self-phase modulation

ⁱⁱ Solving the coupled mode equations and modeling the transmission characteristics revealed that the differential phase shift in real devices involving two-level saturable system can be smaller than π for 80% modulation depth, depending on the relative power density in each arm.

where α_0 and β are one- and two-photon absorption coefficients, respectively. By analyzing the total energy exchanged per unit time and volume between the control beam and the molecular ensemble, the nonlinear index, n_2 , and the two-photon absorption coefficient, β , can be further expressed as functions of the real and imaginary parts of the macroscopic third-order susceptibility tensor, $\chi^{(3)}$, a measure of induced polarization in a bulk material in response to an intense electric field.[44]

$$n_2 = \frac{3}{4 \epsilon_0 n_0^2 c^2} \text{Re}(\chi^{(3)})$$

$$\beta = \frac{3\pi}{\epsilon_0 c n_0^2 \lambda} \text{Im}(\chi^{(3)}) \quad (\text{Eq. 1.4})$$

Hence, the two-photon FOM can be expressed solely using the $\chi^{(3)}$.

$$T = \left| \frac{\text{Re}(\chi^{(3)})}{\text{Im}(\chi^{(3)})} \right| > 4\pi \quad (\text{Eq. 1.5})$$

It is evident that in order to devise a successful phase-shift based AOS, it is critical to identify candidate materials that show a large $\text{Re}(\chi^{(3)})$,ⁱⁱⁱ and small $\text{Im}(\chi^{(3)})$. Along with linear loss (α_0), the above ratio will be an important material parameter discussed throughout this thesis.

1.3 $\chi^{(3)}$ Response of π -Conjugated Organic Materials

ⁱⁱⁱ or equivalently, a large molecular third-order polarizability, $\text{Re}(\gamma)$, see Section 2.1

To identify the materials with a suitable 2PA-FOM, it is important to understand the correlation between the molecular structures and the $\chi^{(3)}$ responses of π -conjugated molecules. For this purpose, the energy levels of a pair of representative π -conjugated molecules, a neutral polyene in butadiene, and a charged polymethine in pentadienyl anion are depicted using a Huckel molecular orbital (MO) model.[48] The molecular structures and the π -orbital energy diagrams are shown below.

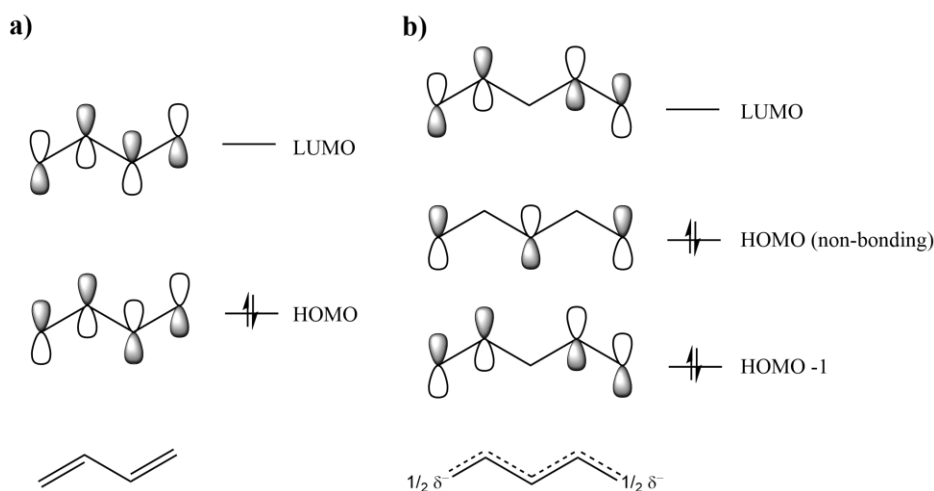


Figure 1.3. Huckel molecular orbital diagram and the corresponding energy of a) butadiene, and b) pentadienyl anion

As can be seen from **Figure 1.3**, the frontier molecular orbitals – the highest occupied and the lowest unoccupied molecular orbital (HOMO/LUMO) – of the butadiene molecule have a non-zero probability density of π electrons centered around the carbon atoms with the nodes located on the bonds. The arrangement of bonding and anti-bonding characters in the overlapping p_z orbitals of adjacent carbon atoms results in a significant bond-length alternation (BLA) – the average difference in the lengths of successive double and single bonds over the conjugated chain. In contrast to butadiene, the frontier

MOs of a pentadienyl anion show that the probability density of π -electrons is largely localized on alternate carbons with the nodes present both on the atoms and the bonds.[49] Hence, a large degree of charge alternation between adjacent carbon atoms is observed; the amount of bonding and anti-bonding characters across the carbon atoms remains roughly the same, leading to a vanishing BLA across the π backbone.[50]

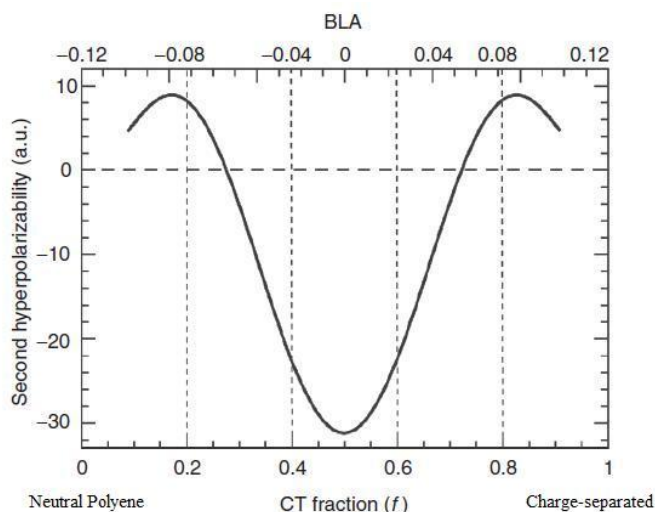


Figure 1.4. A plot of third-order polarizability (second hyperpolarizability) vs. the degree of charge separation in two-resonant structures of polyene and the corresponding bond-length alternation. Reprinted with permission from the authors of [43] (Copyright 2011 © CRC Press.)

Numerous studies have established that the nonlinear optical responses of π -conjugated organics are highly dependent on the BLA.[28, 51, 52] When the static molecular third-order polarizability, γ , ($\propto \chi^{(3)}$) is mapped as a function of the BLA, the evolution of γ shows two positive maxima near the polyene and zwitterions regime, while the largest magnitude is associated with the negative maximum at zero BLA, often referred to as the “cyanine limit.”[53] (**Figure 1.4**) The extent of ground state polarization and the resulting

BLA in π -conjugated organics can be controlled through a number of means including substitution of donor and/or acceptor groups of various strengths, modification of the length and topology of the π -conjugated bridge, and induction of the reaction field by the surrounding medium.[54] Among the different types of π -conjugated molecules, donor-acceptor substituted polyenes and polymers, as well as symmetrically substituted polymethines have been shown to approach these extrema the closest, and thus, are considered as the most suitable candidates for AOS application.

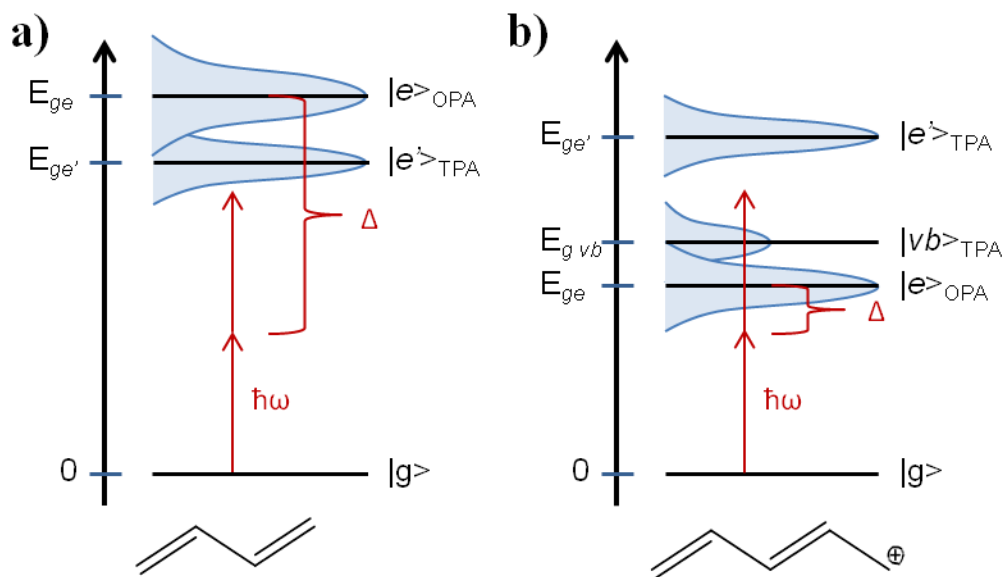


Figure 1.5. State-energy schematics of a) polyenes with the twice the excitation energy, $2\hbar\omega$, below the two-photon resonance, $E_{ge'}$, and b) cyanine-type molecules with $\hbar\omega$ lying just below E_{ge} , and $2\hbar\omega$ positioned in between $E_{g\ vb}$ and $E_{ge'}$ two-photon resonances.

The MO picture also reveals important differences in the electronic transitions of these two classes of molecules and the implications for the AOS applicability. In butadiene, and in other polyenes by extension, any promotion of electrons from HOMO to LUMO is accompanied by a reversal of bonding and anti-bonding characters across the adjacent

carbons. This give rise to a markedly different equilibrium geometry of the excited state from that of the ground state, resulting in a transition that shows a broad absorption band with a vibronic progression. For cyanine molecules like the pentadienyl anion, the same HOMO to LUMO transition involves the shift in the π electron density from even-numbered to odd-numbered carbons,^{iv} (**Figure 1.3**) while the bonding and anti-bonding characters remain largely unaltered. The equilibrium geometry of the excited state is very similar to that of the ground state, giving rise to a sharp, vertical one-photon transition with large transition dipole moment, M_{ge} . In addition, compared to the polyenes of similar π -bridge length, the E_{ge} of polymethines are smaller than that of the polyenes by the virtue of the non-bonding MO that appears energetically halfway between bonding and anti-bonding orbitals.[55] These differences in transition energetics are important in the framework of AOSP. From the simplified sum-over-states expression^v,[56] it is predicted that the magnitude of γ is dominated by the fourth power of M_{ge} , and is also inversely proportional to cube of the detuning energy from the one-photon resonance, $\Delta = E_{ge} - \hbar\omega$. Therefore, comparatively large M_{ge} , and small E_{ge} of polymethines offer a greater potential for an exceptionally large NLO response in the telecommunication wavelengths than polyenes.

A more detailed look into the excited state energy schematics also reveals an approach in which TPA loss can be minimized while preresonant enhancement of γ can be maximized. Polyenes present an energy schematic where the lowest one-photon allowed (OPA) excited state lies close in energy to the lowest two-photon excited state at $\sim 1.3 E_{ge}$.[57, 58] To minimize TPA loss in this case, the control pulse frequency must be

^{iv} or in case of pentadienyl cation, from odd- to even-numbered carbons

^v derived from the simplified perturbation theory; described in detail in the next chapter

sufficiently detuned from the one-half of the energy of the two-photon allowed E_{ge} . Such a constraint results in a rather small γ , or $\chi^{(3)}$, as the incident photon energy is too far removed from the lowest one-photon allowed excited state for preresonant enhancement. Polymethines, on the other hand, possess two TPA excited states near the lowest-lying OPA state: a weakly absorbing, vibronically coupled lower lying two-photon state at $\sim 1.1 E_{ge}$, and a strongly absorbing electronic two-photon state at $\sim 1.7 E_{ge}$. [59-61] (**Figure 1.5**) If the input photon frequency or the energy schematic of a molecule is controlled such that twice the photon energy falls between these two states to avoid the TPA loss, $\hbar\omega$ would automatically fall in the region where the Δ is drastically reduced and the γ can be preresonantly enhanced, provided that the OPA transition is sufficiently narrow such that linear loss can be avoided. By employing this strategy, Hales et al. have reported promising candidate cyanines for AOSP such as selenopyriliium-terminated pentamethine which showed the molecular FOM, $|\text{Re}(\gamma)/\text{Im}(\gamma)|$, of 160 at $1.550\mu\text{m}$, well above the 4π limit discussed in the previous section. [62]

1.4 Strategy for Implementation: Silicon-Organic Hybrid Approach

For the reasons discussed in the preceding sections, an ideal approach for AOSP would be to combine the “passive” waveguiding properties of SOI and the “active” optical properties of π -conjugated organics. One of the methods to facilitate such composite properties is to fabricate the waveguides directly using the organic materials. Successful polymeric waveguides have been demonstrated using polydiacetylene, perfluoropolymer,

methacrylate-fluoromethacrylate copolymer, andOrmocore.[63-66] However, due to the relatively low refractive indexes of these π conjugated organics with respect to Si^{vi}, [67, 68] all of these polymeric waveguides exhibited large effective modal area, and the lower effective irradiance compared to the Si counterpart. With the limited confinement, the researchers were forced to rely on high power operation, thermo-optic effect, and near-resonant regime operation, risking large optical loss to produce sufficient signal modulation. Another major issue with polymeric channel waveguides is the difficulty in creating pattern definitions, cutting and polishing as the fabrication of these waveguides involves costly dry-etching process in addition to the traditional photo- or e-beam lithography.[69, 70]

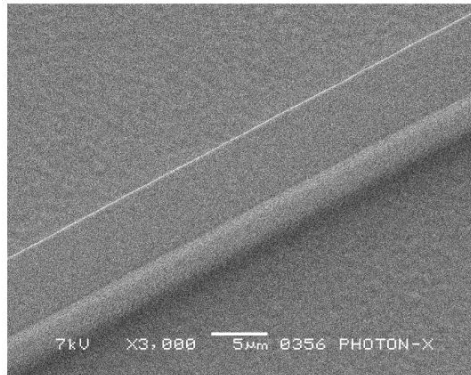


Figure 1.6. SEM micrographs of single-mode $4 \times 4 \mu\text{m}$ perfluoropolymer channel waveguide. Reprinted with permission from the authors [66] (Copyright 2004 © *IEEE/OSA J. Lightwave Technol.*)

An alternate approach is to use a composite architecture, often referred to as silicon-organic hybrid (SOH) design, to combine the waveguiding properties of Si and the large NLO response of π -conjugated organics. In this scheme, a thin layer of organic film (1~2

^{vi} Many π electron rich organic materials with exceptionally high linear polarizability such as thiophene, or quinoxaline containing polymers exhibit refractive indexes < 2 at 1550 nm. [66,67]

μm) is deposited on top of an existing Si waveguide, allowing the evanescent field from the waveguide to couple into the organic cladding. Given finite cross-sectional waveguide dimensions, a transverse interaction length, and input power of the control beam, the phase shift in the signal beam can be controlled primarily by two inherent material properties: static refractive index of the cladding which determines the mode power distribution, and $\chi^{(3)}$ of the cladding material. Mickelson et al. were one of the first pioneers that demonstrated the validity of this approach.[71, 72] They deposited a squarylium dye doped polymethylmethacrylate (PMMA)-styrene-acrylonitrile blend on top of a prefabricated ion exchange waveguide and built a micro-interferometer that was used to measure the overall $\chi^{(3)}$ of the hybrid construct via self-phase modulation with the ability to separate out the $\chi^{(3)}$ contribution from purely the organic cladding.

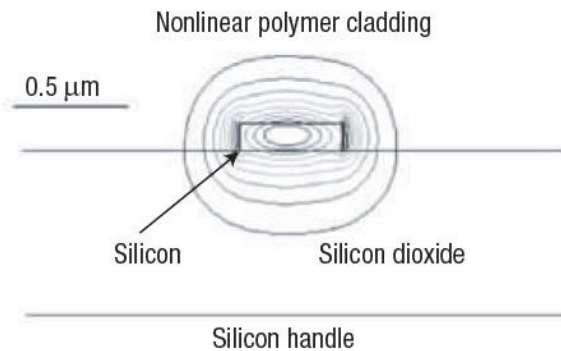


Figure 1.7 Cross-section of a silicon-organic hybrid strip waveguide. Contours represent 10% increments of power. Reprinted with permission from the authors [73] (Copyright 2006 © Nature Publishing Group, *Nature Mater.*)

A decade later, Hochberg et al. achieved terahertz signal modulation using the SOH design by taking advantage of the large nonlinearity and fast response of polarized

carotenoid and azobenzene polymer. The authors successfully observed directly time-domain intensity modulation speeds that reached the limit of their detection (~ 10 GHz) and proved that modulation frequency in excess of 1 THz is possible with the SOH architecture based on the spectral evidence from four-wave mixing (FWM) signal.[73] However, in their study, the majority of optical power was still confined to the Si core as seen from **Figure 1.7**, with the device exhibiting only a third of the $\chi^{(3)}$ of the polymer across the length of the NLO “arm”. This limitation resulted in a rather small differential phase shift of 0.04 rad, and 7% modulation depth (0.3 dB) along with a moderately high 7 dB cm^{-1} waveguide loss.

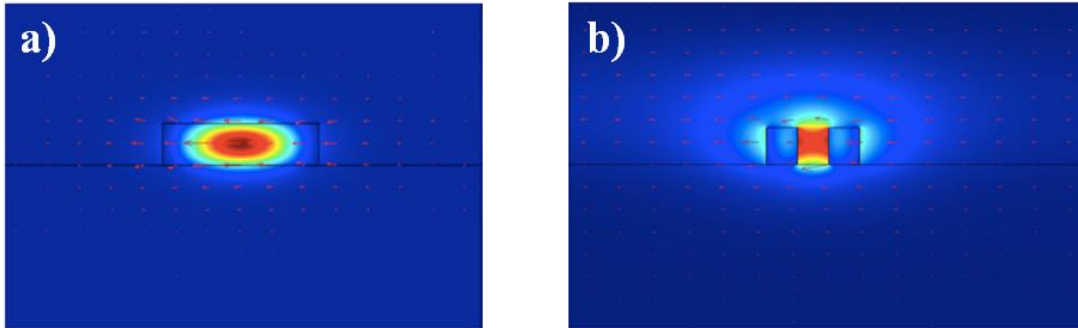


Figure 1.8. Simulation of E_x in SOI showing mode profile with normalized field amplitudes: a) conventional strip waveguide b) slot waveguide. Adapted from Alan Mickelson, *Silicon Photonic Slot Guides for Optics*, Nonlinear International Conference on Microwaves and Photonics, ICMAP 2013, 13-15 December, 2013, Dhanbad, India.

A breakthrough in the waveguide design, pioneered by Lipson group,[74] circumvented the constraints imposed by the relatively weak optical power in evanescent field, and the optical loss of Si which limited the full potential of SOH. By incorporating a slot waveguide design, they facilitated the confinement of optical power in the low-index voids embedded between two high-index slabs. The discontinuity of TE mode electric

field at the high index contrast interfaces concentrates the majority of optical power in the low-index slot with the field enhancement factor proportional to $n_{\text{Si}}^2/n_{\text{slot}}^2$.^{vii}[75]

This architecture has allowed Koos et al. to demonstrate a donor-acceptor polyene containing SOH optical time-domain demultiplexer that was able to convert a 171 GHz signal to a 43 GHz sideband via FWM, over an order of magnitude faster than an equivalent device built using strip Si waveguides.[76] Moreover, by confining the optical power within the narrow low-index slot the propagation loss and modulation depth were dramatically improved to 1.2 dB cm^{-1} , and 7.7dB, (~80%) respectively. While the DDMEBT polyene film used in this demultiplexer showed a near-infrared (NIR) transparency and an acceptable 2PA-FOM of ~10,[77] its smaller Kerr coefficient compared to many polymethine dyes^{viii}, and the necessity for vapor deposition in vacuum for film homogeneity limit its potential for ubiquitous application in AOSP. Hence, the next logical direction in improving further upon the design would be to engineer a more efficient and processable external NLO material for these micro/nano-slots.

^{vii} In air, the enhancement factor ≈ 12 . For a polymer cladding of $n_0=1.7$, the enhancement factor ≈ 4 .
^{viii} $n_2 \approx 1.7 \times 10^{-17} \text{ m}^2 \text{ W}^{-1}$, $\text{Re}(\chi^{(3)}) \approx 1.4 \times 10^{-11} \text{ esu}$

1.5 Aim and Organization of the Thesis

With numerous studies in past having identified a class of π -conjugated molecules with efficient NLO response in polymethines, and a suitable architecture for implementation in SOH configuration, this thesis is mainly concerned with the design and characterization of structure-property relationships among polymethine molecules with improved linear and nonlinear optical properties for AOS applications. This thesis also emphasize (as well as demonstrates) the importance of developing a suitable method to translate their optimized molecular properties into the macroscopic solid-state material properties for device incorporation.

In Chapter 3, the effects of various substitutions on the linear and nonlinear properties of dioxaborine and chalcogenopyrylium terminated polymethine cations are investigated. In particular, we seek to answer 1) the effectiveness of the substitution of metallated terminal groups as a strategy for extending π delocalization and increasing the molecular polarizability, thereby overcoming spontaneous symmetry breaking often observed in longer cyanines;^[78] 2) the effectiveness of steric substituents in preventing the deleterious effects of aggregation while retaining the NLO properties characteristics of cyanines.

In Chapter 4, the challenges associated with the charged nature of cyanine dyes, and the impacts of their interactions with the surrounding medium are addressed. The main issues of interests are 1) the effects of different counterions on the solid-state miscibility of the cyanines, and their ability to form optical quality films with host polymers, and 2) the effects of multiply-charged counterions on the orientations and the electronic

configurations of the chromophores in low-dielectric screening media, and the subsequent effects on the NLO properties.

Chapter 5 focuses on the investigation of other physical properties important in facilitating straightforward implementation of organics onto an existing SOH platform including 1) linear and nonlinear optical properties of common polymer hosts, 2) dispersion characteristics and wetting properties of cyanine-polymer blends, and 3) the effects of substrate surface modifications on cladding infiltration.

Through the thesis, extensive characterization of different cyanines was undertaken to determine their one- and two-photon figures-of-merits for AOS. In the process, we also seek to establish an experimental database from which a better synthetic guideline for optimal molecular and material structure – NLO property relationship can be deduced.

1.6 References

1. Lin, Y.-M., et al., *100-GHz Transistors from Wafer-Scale Epitaxial Graphene*. Science, 2010. **327**(5966): p. 662.
2. Alloatti, L., et al., *42.7 Gbit/s electro-optic modulator in silicon technology*. Optics Express, 2011. **19**(12): p. 11841-11851.
3. *Cisco Visual Networking Index: Forecast and Methodology, 2013–2018*. [White Paper] 2014; Available from: http://www.cisco.com/en/US/solutions/collateral/ns341/ns525/ns537/ns705/ns827/white_paper_c11-481360.pdf.
4. Ramaswami, R., K. Sivarajan, and G. Sasaki, *Optical Networks: A Practical Perspective*. 2009: Elsevier Science.
5. Lukin, M.D. and A. Imamoglu, *Controlling photons using electromagnetically induced transparency*. Nature, 2001. **413**(6853): p. 273-276.
6. Harris, S., J. Field, and A. Imamoglu, *Nonlinear optical processes using electromagnetically induced transparency*. Physical Review Letters, 1990. **64**(10): p. 1107.
7. Strasser, T.A. and M.C. Gupta, *Optical loss measurement of low-loss thin-film waveguides by photographic analysis*. Applied Optics, 1992. **31**(12): p. 2041-2046.
8. Haché, A. and M. Bourgeois, *Ultrafast all-optical switching in a silicon-based photonic crystal*. Applied Physics Letters, 2000. **77**(25): p. 4089-4091.
9. Hecht, E., *Optics*. 2002: Addison-Wesley.
10. Normandin, R., D.C. Houghton, and M. Simard-Normandin, *All-optical, silicon based, fiber optic modulator using a near cutoff region*. Canadian Journal of Physics, 1989. **67**(4): p. 412-419.
11. Tsang, H.K., et al., *Optical dispersion, two-photon absorption and self-phase modulation in silicon waveguides at 1.5 μm wavelength*. Applied Physics Letters, 2002. **80**(3): p. 416-418.
12. Soref, R.A. and B.R. Bennett, *Electrooptical effects in silicon*. Quantum Electronics, IEEE Journal of, 1987. **23**(1): p. 123-129.

13. Lin, Q., et al., *Dispersion of silicon nonlinearities in the near infrared region*. Applied physics letters, 2007. **91**(2): p. 21111-21111.
14. Bristow, A.D., N. Rotenberg, and H.M. van Driel, *Two-photon absorption and Kerr coefficients of silicon for 850–2200nm*. Applied Physics Letters, 2007. **90**(19): p. 191104.
15. Dinu, M., F. Quochi, and H. Garcia, *Third-order nonlinearities in silicon at telecom wavelengths*. Applied Physics Letters, 2003. **82**(18): p. 2954.
16. Soref, R.A. and J. Lorenzo, *All-silicon active and passive guided-wave components for $\lambda = 1.3$ and 1.6 micron*. Quantum Electronics, IEEE Journal of, 1986. **22**(6): p. 873-879.
17. Liu, A., et al., *A high-speed silicon optical modulator based on a metal-oxide-semiconductor capacitor*. Nature, 2004. **427**(6975): p. 615-618.
18. Liao, L., et al. *40 Gbit/s silicon optical modulator for high-speed applications*. Electronics Letters, 2007. **43**, 1196-1197.
19. Park, H., et al., *A hybrid AlGaInAs-silicon evanescent waveguide photodetector*. Optics Express, 2007. **15**(10): p. 6044-6052.
20. Yin, T., et al., *31 GHz Ge n-i-p waveguide photodetectors on Silicon-on-Insulator substrate*. Optics Express, 2007. **15**(21): p. 13965-13971.
21. Stepanov, S. and S. Ruschin, *Modulation of light by light in silicon-on-insulator waveguides*. Applied Physics Letters, 2003. **83**(25): p. 5151-5153.
22. Kang, J.-W., E. Kim, and J.-J. Kim, *All-optical switch and modulator using photochromic dye doped polymer waveguides*. Optical Materials, 2003. **21**(1–3): p. 543-548.
23. Kang, J.-W., J.-J. Kim, and E. Kim, *All-optical Mach–Zehnder modulator using a photochromic dye-doped polymer*. Applied physics letters, 2002. **80**(10): p. 1710-1712.
24. Yin, L. and G.P. Agrawal, *Impact of two-photon absorption on self-phase modulation in silicon waveguides*. Optics Letters, 2007. **32**(14): p. 2031-2033.
25. Mizrahi, V., et al., *Two-photon absorption as a limitation to all-optical switching*. Optics Letters, 1989. **14**(20): p. 1140-1142.

26. Liu, X., et al., *Self-phase modulation and nonlinear loss in silicon nanophotonic wires near the mid-infrared two-photon absorption edge*. Optics Express, 2011. **19**(8): p. 7778-7789.
27. Nalwa, H.S. and S. Miyata, *Nonlinear optics of organic molecules and polymers*. 1996: CRC press.
28. Bredas, J.L., et al., *Third-Order Nonlinear Optical Response in Organic Materials: Theoretical and Experimental Aspects*. Chemical Reviews, 1994. **94**(1): p. 243-278.
29. Haque, S.A. and J. Nelson, *Toward Organic All-Optical Switching*. Science, 2010. **327**(5972): p. 1466-1467.
30. Nalwa, H.S., *Organic Materials for Third-Order Nonlinear Optics*. Advanced Materials, 1993. **5**(5): p. 341-358.
31. Krug, W., et al., *Optical absorption and scattering losses of PTS and poly(4-BCMU) thin-film waveguides in the near infrared*. Journal of the Optical Society of America B, 1989. **6**(4): p. 726-732.
32. Hambir, S.A., G.J. Blanchard, and G.L. Baker, *Disorder induced enhancement of the third order optical nonlinearity in a conjugated polymer*. The Journal of Chemical Physics, 1995. **102**(6): p. 2295-2301.
33. *Spectrally resolved third-order nonlinearities in polydiacetylene microcrystals: influence of particle size*. Journal of the Optical Society of America B: Optical Physics, 1998. **15**(12): p. 2937.
34. Thienpont, H., et al., *Saturation of the hyperpolarizability of oligothiophenes*. Physical Review Letters, 1990. **65**(17): p. 2141-2144.
35. Yang, L., et al., *Direct evidence of polaron resonance enhancement of cubic susceptibility in polythiophene*. Synthetic Metals, 1991. **43**(1-2): p. 3197-3200.
36. Osaheni, J.A., et al., *Nonlinear optical properties of polyanilines and derivatives*. The Journal of Physical Chemistry, 1992. **96**(7): p. 2830-2836.
37. Lawrence, B., et al., *Large purely refractive nonlinear index of single crystal P-toluene sulphonate (PTS) at 1600 nm*. Electronics Letters, 1994. **30**(5): p. 447-448.

38. Rao, D.N., et al., *Third order nonlinear optical interactions in thin films of poly-p-phenylenebenzobisthiazole polymer investigated by picosecond and subpicosecond degenerate four wave mixing*. Applied Physics Letters, 1986. **48**(18): p. 1187-1189.
39. Stegeman, G.I., et al., *Third order nonlinear integrated optics*. Lightwave Technology, Journal of, 1988. **6**(6): p. 953-970.
40. Nakamura, S., et al., *High-speed all-optical switching experiment in Mach–Zehnder configuration using GaAs waveguide*. Applied physics letters, 1993. **62**(9): p. 925-927.
41. Bogoni, A., et al., *Regenerative and reconfigurable all-optical logic gates for ultra-fast applications*. Electronics Letters, 2005. **41**(7): p. 435-436.
42. Asobe, M., et al., *Low power all-optical switching in a nonlinear optical loop mirror using chalcogenide glass fibre*. Electronics Letters, 1996. **32**(15): p. 1396-1397.
43. Sun, S.-S. and L.R. Dalton, *Introduction to organic electronic and optoelectronic materials and devices*. 2011: CRC Press.
44. Sutherland, R.L., *Handbook of nonlinear optics*. 2003: CRC press.
45. Stegeman, G.I. and E.M. Wright, *All-optical waveguide switching*. Optical and Quantum Electronics, 1990. **22**(2): p. 95-122.
46. Stegeman, G.I. *Material figures of merit and implications to all-optical waveguide switching*. 1993.
47. Stegeman, G.I., et al., *Parameter trade-offs in nonlinear directional couplers: Two level saturable nonlinear media*. Optics Communications, 1987. **63**(5): p. 281-284.
48. Hückel, E., *Quantentheoretische Beiträge zum Benzolproblem*. Zeitschrift für Physik, 1931. **70**(3-4): p. 204-286.
49. Giesecking, R.L., et al., *25th Anniversary Article: Design of Polymethine Dyes for All-Optical Switching Applications: Guidance from Theoretical and Computational Studies*. Advanced Materials, 2014. **26**(1): p. 68-84.
50. Meyers, F., et al., *Electric field modulated nonlinear optical properties of donor-acceptor polyenes: sum-over-states investigation of the relationship between*

- molecular polarizabilities (. alpha.,. beta., and. gamma.) and bond length alternation.* Journal of the American Chemical Society, 1994. **116**(23): p. 10703-10714.
51. Hermann, J. and J. Ducuing, *Third-order polarizabilities of long-chain molecules.* Journal of Applied Physics, 1974. **45**(11): p. 5100-5102.
 52. Johr, T., et al., *Third-order nonlinear polarizabilities of a homologous series of symmetric cyanines.* Chemical physics letters, 1995. **246**(4): p. 521-526.
 53. Marder, S.R., et al., *A unified description of linear and nonlinear polarization in organic polymethine dyes.* Science, 1994. **265**(5172): p. 632-635.
 54. Hales, J.M., et al., *Design of Organic Chromophores for All-Optical Signal Processing Applications.* Chemistry of Materials, 2013. **26**(1): p. 549-560.
 55. Salem, L., *Molecular orbital theory of conjugated systems.* 1966.
 56. Orr, B. and J. Ward, *Perturbation theory of the non-linear optical polarization of an isolated system.* Molecular Physics, 1971. **20**(3): p. 513-526.
 57. Cave, R.J. and E.R. Davidson, *Theoretical investigation of several low-lying states of trans, trans-1, 3,5-hexatriene.* The Journal of Physical Chemistry, 1988. **92**(3): p. 614-620.
 58. Lappe, J. and R.J. Cave, *On the Vertical and Adiabatic Excitation Energies of the 21Ag State of trans-1,3-Butadiene.* The Journal of Physical Chemistry A, 2000. **104**(11): p. 2294-2300.
 59. Fu, J., et al., *Molecular structure two-photon absorption property relations in polymethine dyes.* Journal of the Optical Society of America B, 2007. **24**(1): p. 56-66.
 60. Mukhopadhyay, S., et al., *Polymethine dyes for all-optical switching applications: a quantum-chemical characterization of counter-ion and aggregation effects on the third-order nonlinear optical response.* Chemical Science, 2012. **3**(10): p. 3103-3112.
 61. Schreiber, M., Bu, and M.P. Fulscher, *The electronic spectra of symmetric cyanine dyes: A CASPT2 study.* Physical Chemistry Chemical Physics, 2001. **3**(18): p. 3906-3912.

62. Hales, J.M., et al., *Design of polymethine dyes with large third-order optical nonlinearities and loss figures of merit*. Science, 2010. **327**(5972): p. 1485-1488.
63. Hida, Y., H. Onose, and S. Imamura, *Polymer waveguide thermo-optic switch with low electric power consumption at 1.3 μ m*. Photonics Technology Letters, IEEE, 1993. **5**(7): p. 782-784.
64. Ma, H., A.K.-Y. Jen, and L.R. Dalton, *Polymer-based optical waveguides: materials, processing, and devices*. Advanced materials, 2002. **14**(19): p. 1339-1365.
65. Wang, M., et al., *Fabrication of optical inverted-rib waveguides using UV-imprinting*. Microelectronic Engineering, 2011. **88**(2): p. 175-178.
66. Yeniay, A., et al., *Ultra-low-loss polymer waveguides*. Journal of lightwave technology, 2004. **22**(1): p. 154.
67. Truchon, J.-F., et al., *Integrated continuum dielectric approaches to treat molecular polarizability and the condensed phase: refractive index and implicit solvation*. Journal of chemical theory and computation, 2009. **5**(7): p. 1785-1802.
68. Zhao, M.T., B.P. Singh, and P.N. Prasad, *A systematic study of polarizability and microscopic third-order optical nonlinearity in thiophene oligomers*. The Journal of chemical physics, 1988. **89**(9): p. 5535-5541.
69. Kaino, T., B. Cai, and K. Takayama, *Fabrication of DAST channel optical waveguides*. Advanced Functional Materials, 2002. **12**(9): p. 599-603.
70. Inoue, S.-i., K. Kajikawa, and Y. Aoyagi, *Dry-etching method for fabricating photonic-crystal waveguides in nonlinear-optical polymers*. Applied physics letters, 2003. **82**(18): p. 2966-2968.
71. Chon, J.C. and A.R. Mickelson, *Fabrication and characterization of a third-order nonlinear organic-polymer composite glass waveguide: a self-phase modulator*. Applied Optics, 1994. **33**(30): p. 6935-6941.
72. Chen, X., et al. *Polymer-Clad Silicon on Insulator Slot Modulator*. in *Advanced Photonics*. 2011. Toronto: Optical Society of America.
73. Hochberg, M., et al., *Terahertz all-optical modulation in a silicon-polymer hybrid system*. Nature materials, 2006. **5**(9): p. 703-709.

74. Almeida, V.R., et al., *Guiding and confining light in void nanostructure*. Optics Letters, 2004. **29**(11): p. 1209-1211.
75. Almeida, V.R., et al., *All-optical control of light on a silicon chip*. Nature, 2004. **431**(7012): p. 1081-4.
76. C, K., et al., *All-optical high-speed signal processing with silicon-organic hybrid slot waveguides*. Nat Photon, 2009. **3**(4): p. 216-219.
77. Esembeson, B., et al., *A High-Optical Quality Supramolecular Assembly for Third-Order Integrated Nonlinear Optics*. Advanced Materials, 2008. **20**(23): p. 4584-4587.
78. Tolbert, L.M. and X. Zhao, *Beyond the cyanine limit: Peierls distortion and symmetry collapse in a polymethine dye*. Journal of the American Chemical Society, 1997. **119**(14): p. 3253-3258.

CHAPTER 2

THIRD-ORDER OPTICAL RESPONSES AND THE CHARACTERIZATION TECHNIQUES

In order to propose an effective molecular design strategy for AOSP applications, a concrete understanding of the third-order optical responses of π -conjugated organic materials must be established. To this end, the theoretical underpinning behind the molecular and material parameters associated with intensity-dependent refractive index change (nonlinear refraction) and two-photon absorption will be described in this chapter. In addition, the optical characterization techniques that will allow for the extraction of these parameters, including prism coupling, Z-scan, time-resolved pump-probe transient absorption spectroscopy, and non-degenerate two-photon absorption spectroscopy will be discussed in detail.

2.1 Third-Order Polarizability

2.1.1 Macroscopic Electric Susceptibility

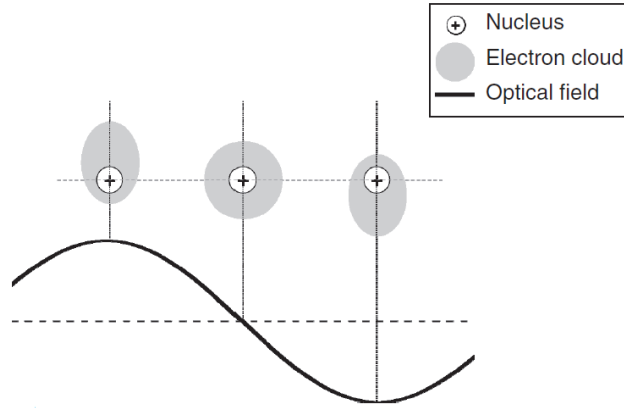


Figure 2.1. Oscillatory motion of the electron cloud in response to an applied electric field. Reprinted with permission from the authors [43] (Copyright 2011 © CRC Press).

Electromagnetic field of a light wave propagating through a medium exerts forces on the loosely bound outer or valence electrons of the medium. Ordinarily, these forces are quite small, and in a linear isotropic medium, the resulting electric polarization, \mathbf{P} , is parallel with and directly proportional to the applied field. (**Figure 2.1**) Consequently, one can write,

$$\mathbf{P}(\omega) = \varepsilon_0 \chi(\omega) \mathbf{E}(\omega) \quad (\text{Eq.2.1})$$

where $\chi(\omega)$ is a dimensionless quantity known as the electric susceptibility. In the case of very high fields such as in the case of a laser exposure, one can expect \mathbf{P} will become saturated; in other words, it simply cannot increase linearly indefinitely with \mathbf{E} . Thus we can anticipate a gradual increase of the ever-present but usually small nonlinearity as \mathbf{E}

increases. Since the direction of \mathbf{P} and \mathbf{E} coincide in an isotropic medium, we can express polarization as a Taylor series expansion:

$$\begin{aligned} \frac{\mathbf{P}_i(\omega)}{\varepsilon_0} = & \chi_{ij}^{(1)}(\omega)\mathbf{E}_j(\omega) + \frac{1}{2}\chi_{ijk}^{(2)}(-(\omega_1 + \omega_2); \omega_1, \omega_2)\mathbf{E}_j(\omega_1)\mathbf{E}_k(\omega_2) \\ & + \frac{1}{3!}\chi_{ijkl}^{(3)}(-(\omega_1 + \omega_2 + \omega_3); \omega_1, \omega_2, \omega_3)\mathbf{E}_j(\omega_1)\mathbf{E}_k(\omega_2)\mathbf{E}_l(\omega_3) + \dots \quad (\text{Eq. 2.2}) \end{aligned}$$

The electric susceptibility, $\chi^{(n)}$, is a tensor of rank $(n+1)$, e.g. $\chi^{(3)}$ is a fourth-rank tensor with 81 components.[43] The subscripts $i, j, k,$ and l represent the laboratory fixed axes. It is important to note that $\chi^{(n)}$ is a complex quantity since the polarization depends only on the electric field that was present at a previous time, and can be represented by a phase difference^{ix}; thus $\chi^{(n)}$ must satisfy Kramers–Kronig constraints.[79, 80] This complex frequency dependence of the electric susceptibilities often prevents a direct comparison between the $\chi^{(n)}$ s associated with different third-order optical phenomena. For AOSP applications, the nonlinear optical phenomena of interests are primarily limited to intensity-dependent refractive index change and degenerate two-photon absorption. Thus, any subsequent mention of $\chi^{(3)}$ for the purpose of this thesis implies the incident field frequencies of ω such that $\omega_1 = -\omega_2 = \omega_3$, and the identical incident polarizations such that $\chi_{ijkl}^{(3)}$ can be treated as one of the diagonal tensor elements, e.g. $\chi_{jjjj}^{(3)}(-\omega; \omega, -\omega, \omega)$, representing the material response to a frequency of $-\omega$, along the single axis j . [43]

2.1.2 Microscopic Molecular Polarizability

^{ix} $\text{Re}(\chi^{(3)})$ is considered an in-phase component, and $\text{Im}(\chi^{(3)})$ is the out-of-phase

At the atomic or molecular level, the polarization is equivalent to the dipole moment induced by the field and can be similarly expressed by a Taylor series.

$$\boldsymbol{\mu}^{ind} = \alpha \mathbf{E} + \beta \mathbf{E}^2 + \gamma \mathbf{E}^3 + \dots \quad (\text{Eq.2.3})$$

Since E^2 is proportional to the intensity of light, the third term, γE^3 can be regarded as an intensity dependent NLO response of the medium to a presence of a third electric field.

The perturbation theory allows for the expression of linear and nonlinear polarizabilities in terms of the relationship between ground and excited states in what is commonly referred to as a sum-over-states (SOS) expression.[56, 81, 82] When the electronic ground state g is significantly coupled to a single excited state e , which in turn is strongly coupled to a few higher lying excited states e' , the γ in the above equation can be expressed as,

$$\gamma(\omega) \propto \left\{ \begin{array}{l} \frac{M_{ge}^2 \Delta \mu_{eg}^2}{(E_{ge} - \hbar\omega - i\Gamma_{ge})^2 (E_{ge} - 2\hbar\omega - i\Gamma_{ge})} \quad (\text{D term}) \\ + \frac{M_{ge}^2 M_{ee'}^2}{(E_{ge} - \hbar\omega - i\Gamma_{ge})^2 (E_{e'e} - 2\hbar\omega - i\Gamma_{ge})} \quad (\text{T term}) \\ - \frac{M_{ge}^4}{(E_{ge} - \hbar\omega - i\Gamma_{ge})^3} \quad (\text{N term}) \end{array} \right\} \quad (\text{Eq. 2.4})$$

where M_{ge} , and $M_{ee'}$ represent the transition dipole moments, E_{ge} , $E_{ee'}$ and Γ denote the transition energies and the corresponding damping factor^x, and $\Delta \mu_{ge}$ is the difference in state dipole moments between g and e . The three terms are denoted **D** for dipolar term, **T** for two-photon term,^{xi} and **N** for negative term. As can be seen from this expression, the interplay of the three different terms can result in the real part of molecular polarizability

^x half-width of the transition band at half-maximum, for cyanines, 0.08 ~ 0.1eV for $g \rightarrow e$ transition

^{xi} the name derived from two-photon allowed $g \rightarrow e'$ transition

$\text{Re}(\gamma)$, being either positive, or negative (Eq. 2.4). Both cases can be exploited for AOSP as long as the magnitude of $\text{Re}(\gamma)$ is large,[54] although as previously discussed in **Section 1.2** and **1.3**, the largest magnitude of $\text{Re}(\gamma)$ is commonly associated with the negative peak at the “cyanine” limit. The imaginary part of the polarizability, $\text{Im}(\gamma)$, represents the probability for two-photon absorption, and therefore, can be minimized by imparting the non-negligible detuning from the two-photon resonance. ($\Delta_{\text{TP}} = E_{ge} - 2\hbar\omega$)

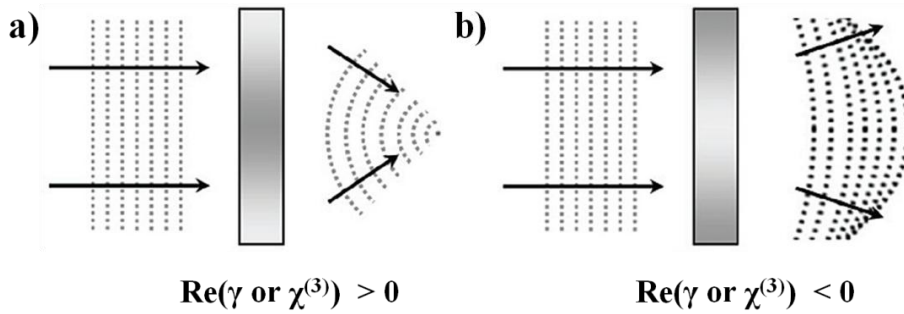


Figure 2.2. The effects of an induced phase change (illustrated in the samples) on incident phase fronts. a) Self-focusing in a medium with a positive γ or $\chi^{(3)}$. b) Self-defocusing in a medium with a negative γ or $\chi^{(3)}$. Reprinted with permission from the authors [43] (Copyright 2011 © CRC Press)

With the molecules such as polymethines which show similar ground and excited state geometries, or centrosymmetric molecules such as symmetrically-substituted polyenes which show no net static dipole, the $\Delta\mu_{ge}$ vanishes and the dipolar (**D**) term approaches zero. This implies that molecular third-order optical response will be dominated by the **T** and **N** terms. In addition, M_{ee} in these π -conjugated organics are generally smaller than M_{ge} , while Δ_{TP} takes a non-negligible value to avoid potential two-photon loss. Hence, the nonlinear optical responses of candidate molecules for AOSP are predominantly

governed by the parameters in the \mathbf{N} term: the ground to the lowest excited state transition dipole moment, M_{ge} , and the detuning ($\Delta=E-\hbar\omega$) of the incident frequency.

2.1.3 Relationship between γ and $\chi^{(3)}$

Most NLO characterization techniques measure the changes in transmittance through bulk media from which information about macroscopic nonlinearity such as nonlinear refractive index n_2 , and two-photon absorption coefficient β , are obtained. Therefore, in order to determine appropriate molecular properties from the measured bulk properties, it is necessary to establish a relationship between the microscopic and macroscopic nonlinearities. If we consider the induced macroscopic polarization as the average of microscopic dipole moment induced per unit volume, then the macroscopic polarization \mathbf{P} can be written as,

$$\mathbf{P}_i = N\langle\boldsymbol{\mu}_i^{ind}\rangle \quad (\text{Eq. 2.5})$$

where N is the number density of microscopic dipoles per unit volume, and $\langle \rangle$ is the orientational averaging of all microscopic dipoles.[43]

It is important to note that \mathbf{E} s in Equation 2.2 assumes the polarization response of an isolated atom or molecule in a vacuum. In a medium where a molecule is surrounded by other molecules with a finite polarizability, the local fields from these surrounding species contribute to the overall field in addition to the applied macroscopic fields. To

account for this, the macroscopic fields can be corrected for via Lorentz local field factors. The relationship between these fields can then be written as,

$$\mathbf{E}'_i(\omega) = L(\omega)\mathbf{E}_i(\omega) \quad (\text{Eq. 2.6})$$

where the local field is given by,

$$L(\omega) = \frac{n(\omega)^2+2}{3} \quad (\text{Eq. 2.7})$$

It is worth noting that since most materials have refractive indexes of greater than 1, the local fields amplify the applied macroscopic field. Applying this field correction, one can obtain the relationship between the microscopic polarizability, γ , and macroscopic susceptibility, $\chi^{(3)}$. [43]

$$\chi_{jjjj}^{(3)}(-\omega) = NL(\omega)^4\langle\gamma_{jjjj}(-\omega)\rangle \quad (\text{Eq. 2.8})$$

2.1.4 Units of γ and $\chi^{(3)}$

In this thesis, the units of $\chi^{(3)}$ are given in cgs units expressed as *esu* or $cm^2 \text{ statVolt}^{-2}$. The conversion to MKS units is given by, [44, 81]

$$\chi^{(3)}[m^2 \cdot V^{-2}, \text{MKS}] = \left(\frac{4\pi}{9} \cdot 10^{-8}\right) \cdot \chi^{(3)}[cm^2 \cdot \text{statVolt}^{-2} \text{ or } \text{esu}, \text{cgs}] \quad (\text{Eq. 2.9})$$

2.2 Characterization Methods

In order to identify ideal candidate polymethines for AOS application, a number of optical parameters must be determined: linear and nonlinear refractive indexes, two-photon absorption coefficient, and linear optical loss. This section describes characterization techniques that allows for measurement of these parameters.

2.2.1 Prism Coupling

A prism coupler is a device that can efficiently couple a laser beam into thin-film dielectric waveguides, and allow an accurate measurement of the spectrum of propagating modes from which the refractive index and the thickness of the film can be determined.[83]

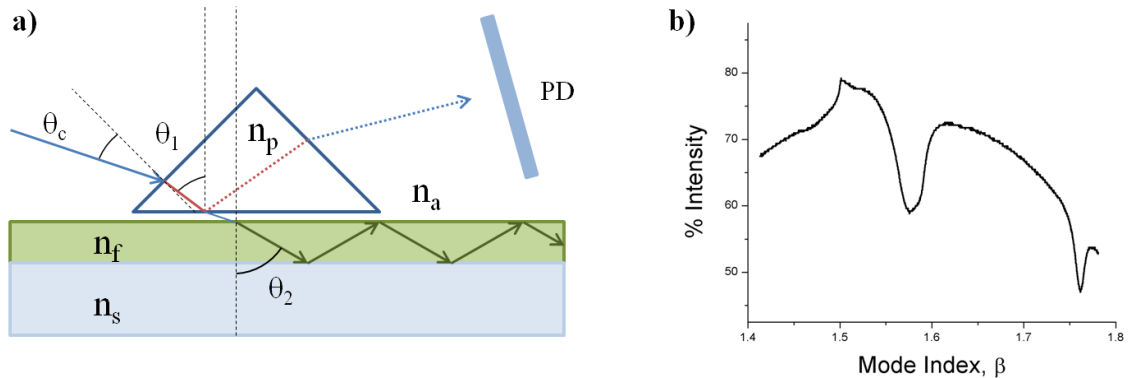


Figure 2.3. a) Simplified diagram of a prism coupler. A thin film is pressed against a face of a prism via pneumatically-operated coupling head (not shown). The incident beam either reflects off the base surface of the prism, or tunnels through the air gap or couples in the film. b) Plot of percent intensity vs. mode index, a function of the incidence angle and the refractive index of the prism.

The basic principles of operation and the components involved are shown in **Figure 2.3**

a). The angle of incidence of the laser, θ , can be swept by means of a rotary table on

which the prism, film, and the photodetector are mounted. When the horizontal component of the wave incident to the film, called effective mode index, β^{xii} , is equal to the propagation constant of one of the supported film modes, the photons violate the total internal reflection criterion and tunnel from the base of the prism across the air gap and into the film, causing a sharp drop in the intensity of light striking the photo detector.[84] This coupling condition can be expressed using Snell's law.

$$\beta(\theta_c) = n_p \sin \theta_1 = n_f \sin \theta_2 \propto \frac{\omega}{v_{p \text{ film}}} \quad (\text{Eq. 2.10})$$

where n_p^{xiii} and n_f are the indexes of the prism and the film, and $v_{p \text{ film}}$ is the phase velocity of the wave in the film. If the intensity striking the photodetector is plotted as a function of the incident angle θ , and by extension, the mode index β , a spectrum similar to **Figure 2.3 b)** is produced. It is important to note that depending on the index and thickness of the film and the wavelengths of the laser, there can be multiple incident angles θ_c where the above condition is satisfied. The reciprocity of the modes supported by the film is governed by the following eigenvalue equation, commonly referred to as the mode equation.[85]

$$\left(\frac{2\pi}{\lambda}\right) n_f \cos(\theta_2) t + \varphi_{af} + \varphi_{fs} = m\pi \quad m = 0,1,2 \dots \quad (\text{Eq. 2.11})$$

^{xii} not to be confused with β used for two-photon absorption coefficients or second-order polarizabilities

^{xiii} The prism used throughout this thesis was gadolinium gallium garnet (GGG) crystal with n_p of 1.9345 at $1.55\mu\text{m}$.

where θ_2 is the incident angle of the evanescent wave in the air gap with respect to the normal of the film^{xiv}, t is the film thickness, and φ_{af} and φ_{fs} are the Fresnel phase shifts at the air-film and film-substrate interfaces. The Fresnel phase shifts are functions of the mode index, β and given by the following,[85]

$$\varphi_{af} = \tan^{-1} \left(\left(\frac{n_f}{n_a} \right)^2 \left(\frac{\sqrt{\beta^2 - n_a^2}}{n_f \cos \theta_2} \right) \right)$$

$$\varphi_{fs} = \tan^{-1} \left(\left(\frac{n_f}{n_s} \right)^2 \left(\frac{\sqrt{\beta^2 - n_s^2}}{n_f \cos \theta_2} \right) \right) \quad (\text{Eq. 2.12})$$

where subscripts a, f, and s denote air, film, and substrate, respectively. Therefore, Equation 2.11 becomes a complex transcendental equation where, for a given substrate type, the angular locations of the modes depend only on the film index, n_f , and thickness, t . When two or more modes are coupled, and the corresponding values of β are determined, the mode equation becomes a system of equations with a common solution; hence, the refractive index and thickness of a film can be solved numerically.

^{xiv} when the coupling condition is met, $\cos \theta_2 = \sqrt{1 - \left(n_p \sin \theta_1 / n_f \right)^2}$

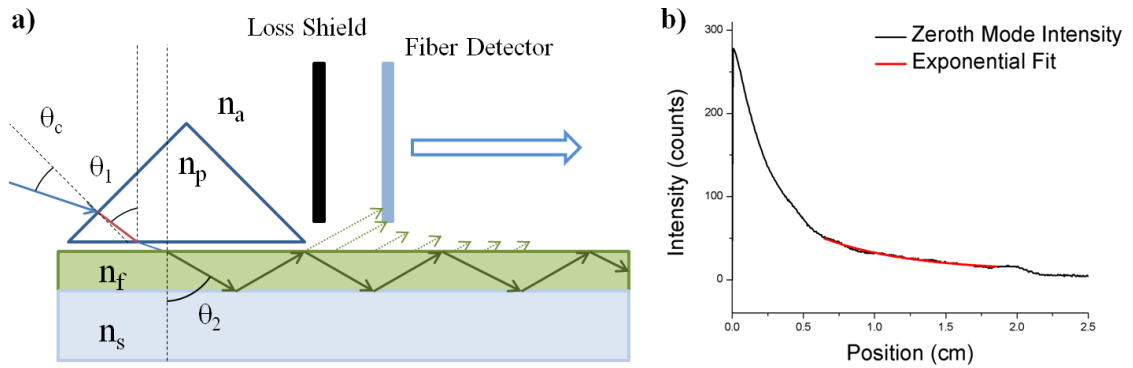


Figure 2.4. a) Prism coupler in loss measurement mode, b) intensity vs distance pattern; the large intensity drop in the first ~150 steps (0.75cm) caused by extraneous light scattering near the prism can be mitigated by installing a loss shield.

Prism couplers can also be used to measure linear propagation loss through a thin film.[86] Once the incident light is coupled maximally to a guiding mode of the film, a fiber probe scans down the lengths of the propagating streak and measures the exponential decay of light. A least squares fit is then made to the intensity vs. distance pattern, and the loss is calculated in dB/cm. If the film supports multiple guiding modes, the zeroth order mode – the coupling peak with largest mode index – is typically selected for linear loss analysis to minimize the impact of potential leaky modes into the substrate.

The refractive indexes and linear losses of the films reported in Chapter 3, 4, and 5 were determined using a Metricon 2010 prism coupler. The light source used was a Melles-Griot Diode laser 57STL051 with an output power of approximately 1.2 mW of CW light at 1.55 μ m. The usable detection range for the loss measurement is 0.5–2.0 dB/cm. The error associated with the technique depends on the length of the film and the quality of the exponential fit; for typical films of 3.5cm in length, the error is estimated to be $\pm 20\%$.

2.2.2 Z-scan

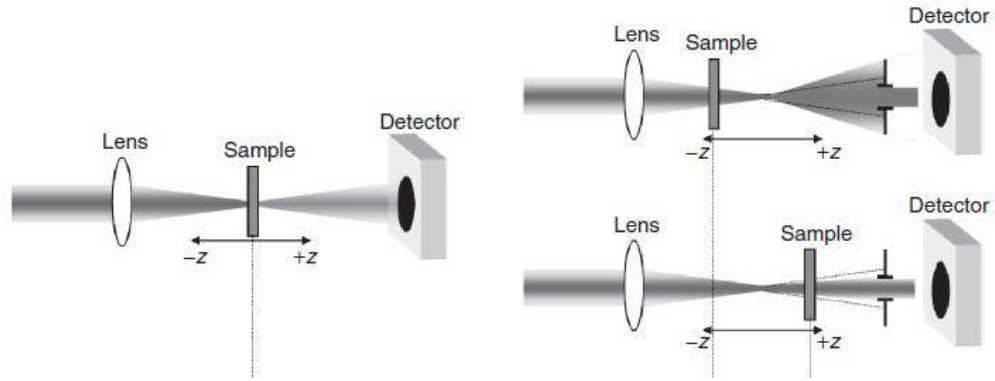


Figure 2.5. Simplified schematic of Z-scan experiment: material with a positive nonlinear refractive index, n_2 , will induce self-focusing at negative Z position, and self-defocusing at the positive Z. Shown on the left is the open aperture scan where the transmitted beam is collected in its entirety, revealing the nonlinear absorption coefficient; on the right is the close aperture scan where the collection geometry is restricted by an aperture. Reprinted with permission from the authors [43] (Copyright 2011 © CRC Press.)

The Z-scan is a single beam spectroscopic technique that can rapidly measure both two-photon absorption coefficient, and the nonlinear refractive index in solids (including thin films), and liquids.[87, 88] The transmittance of the beam through the sample in the vicinity of the focal position is monitored in the far-field as a function of the position, Z. The open aperture scan, which monitors the entire transmitted beam collected, and is only sensitive to nonlinear absorption, is used to obtain the nonlinear absorption coefficient β , from which the imaginary part of $\chi^{(3)}$ can be extracted. With β known, the closed aperture scan, sensitive to both nonlinear refraction, and nonlinear absorption, allows for the

extraction of n_2 and thus the real part of $\chi^{(3)}$. Since Z-scan is an absolute method, the spatial and temporal properties of the beam have to be carefully measured. In addition, before every measurement, the experimental setup must be calibrated using well-established nonlinearities of the samples such as fused silica, ZnS, ZnSe, and GaAs. The most commonly accepted values of the nonlinearities for these references are given in **Table 2.1**.

Table 2.1. Nonlinear optical properties of references at 1.55 μm

Samples	Thickness (μm)	n_0	n_2 (m^2/W)	β (m/W)	Ref
Fused Silica	1000	1.445	2.63×10^{-20}		[89]
ZnS	1016	2.271	5.77×10^{-19}		[90]
ZnSe	1016	2.457	1.18×10^{-18}		[90-92]
GaAs	410	3.374	2.29×10^{-17}	9.03×10^{-11}	[93, 94]

Z-scan is sensitive to all nonlinear optical mechanisms that give rise to a change of refractive index and/or absorption coefficient, not just two-photon absorption or the two-photon induced index change; thus, in order to ensure the observed nonlinear absorption and refractions are third-order in nature, the Z-scan must be performed at varying excitation energies.

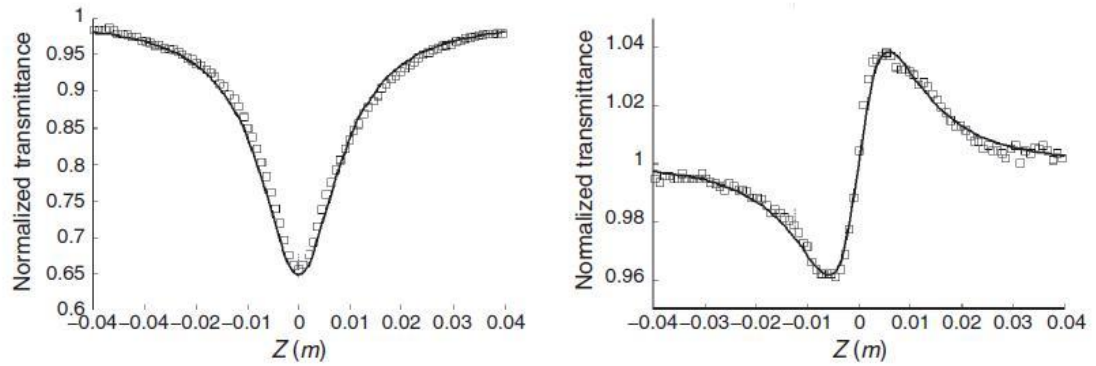


Figure 2.6. Examples of Z-scan data and the corresponding fitting functions. (left) Open aperture data of 410 μ m GaAs; (right) closed aperture data of 1mm fused SiO₂.

Sample Z-scan traces are shown in **Figure 2.6**. The principal quantity of interest here is the net transmittance of the material to the beam at a particular frequency. Assuming that the beam propagating through the sample is Gaussian, the nonlinear absorption coefficient, β , is extrapolated by fitting the trace of the open aperture transmittance using the following function.[88]

$$T = \frac{(1-R)^2 e^{-\alpha L}}{\sqrt{\pi} q_0} \int_{-\infty}^{\infty} \ln(1 + q_0 e^{(-z^2)}) dz \quad (\text{Eq. 2.13})$$

$$q_0 = \frac{\beta(1-R)I_0(1 - e^{-\alpha L})}{\alpha}$$

In this expression, the effect of nonlinear absorption on transmittance is integrated over all space. However, during an actual experiment, the transmittance of the beam is sampled at a predefined increment; thus the integrated transmittance is replaced by summation, and approximated using the trapezoidal rule.[95] All other parameters – Fresnel reflection coefficient R, peak on axis intensity I_0 , the sample length L, and the

linear absorption coefficient α , are known values already obtained from prism coupling measurements. Thus, the only unknown variable in fitting of the open aperture trace is β . In order to determine β , an arbitrary value is first assigned, and the fit of the function is iteratively evaluated until a reasonably accurate curve is generated.

The important parameter in obtaining the intensity dependent index, n_2 , from the closed aperture scan is the change in transmittance between the peak and valley, $\Delta T_{pv} = |T_p - T_v|$, where T_p and T_v are the normalized peak and valley transmittances. (**Figure 2.6**) The empirically determined relation between the induced phase distortion and the change in transmittance in the absence of nonlinear absorption is given by the following formula,[88]

$$|\Delta\varphi_0| = \frac{\Delta T_{pv}}{0.406(1-S)^{0.25}} \quad (\text{Eq. 2.14})$$

where S is the transmittance of the aperture in absence of the sample. Once the total phase change $\Delta\varphi_0$ is obtained, one can calculate the magnitude of n_2 given the length of the sample, the wavelength, and the intensity of the beam. The closed aperture scan also reveals the sign of the intensity dependent refractive index of the sample. For materials with positive n_2 , beam will focus prematurely resulting in a more divergent beam in the far-field until the sample reaches the beam waist. Past the beam waist, the material will cause the beam to collimate and the transmittance through the aperture will increase.

Thus, the plot of transmittance will show a valley at the negative Z position, and a peak at the positive Z position. Conversely, if the material possesses a negative n_2 , the focusing beam will be pushed further downfield, increasing the transmittance, until the sample passes the beam waist, past which the beam will experience a greater defocusing. In this

case, the peak will precede the valley in the plot of transmittance as a function of position Z (**Figure 2.5**).

The light source used for all Z-scan measurements was a regeneratively amplified Ti:Sapphire system (Solstice, Spectra-Physics) that produces approximately 70 fs (HW 1/e) pulses at 800 nm with a repetition rate of 1 kHz. This, in turn, pumps an optical parametric amplifier of white-light continuum (TOPAS-C, Spectra-Physics) that provides output pulses of approximately 65 fs (HW 1/e) in the appropriate spectral bands. The detectors used for the collection of all signals (reference, closed, and open-aperture) were large area Ge photoreceivers (Model#2033, NewFocus). These signals were passed through Boxcar integrator units (SR250, Stanford Research Systems) and acquired using a data acquisition card (6025E, National Instruments) and a home-built Labview® program.

2.2.3 Femto-second Transient Absorption Spectroscopy

Transient absorption spectroscopy is a pump-probe technique with which the photophysical response of an excited molecule such as excited state absorption and the rise and decay dynamic of various photo-induced transient species can be investigated. The basic principle of transient absorption spectroscopy is to excite a desired one-photon absorption band of the target molecule with a strong pump pulse, and then to examine the photo-induced transient species with a weak, broadband probe pulse. By varying the temporal delay of the probe pulse, the absorption of the transient species can be monitored at different delays, and therefore, the temporal dynamics of the transient species can be determined.

While the resolution of a wide range of excited state dynamics can be made possible with the use of pump beams of different pulse widths, and varying delay geometries, for the purpose of this thesis, this technique was used to determine the excited state absorption cross-sections for the calculation of M_{ee} of various cyanine-like molecules. Hence, our focus was limited to the ultrafast absorption response within the initial 20~150 femtoseconds upon the temporal overlap of the pump and the probe beam. A simplified layout of the transient absorption setup is shown below.

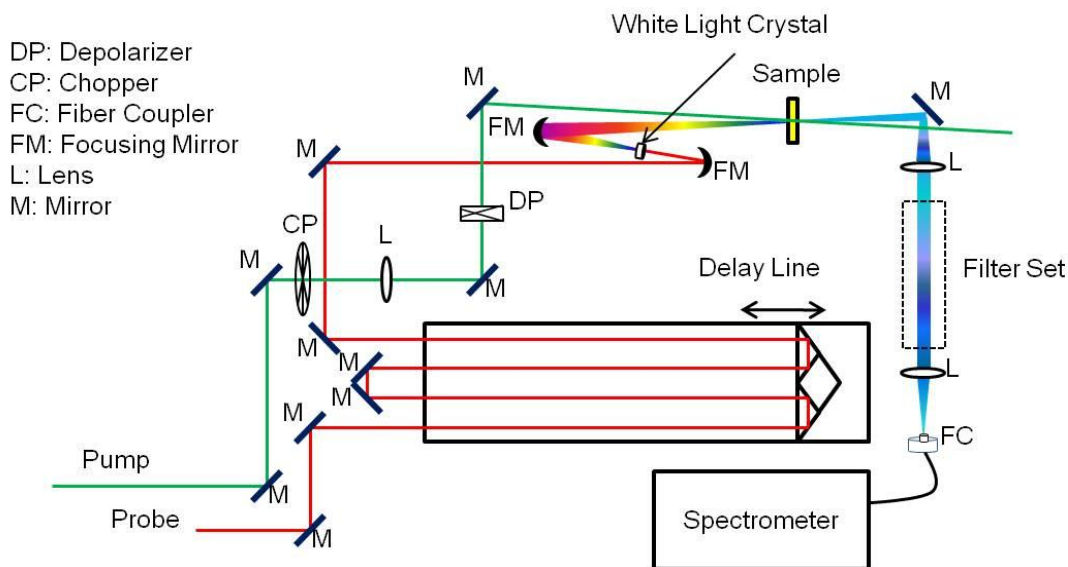


Figure 2.7. The layout of the pump-probe transient absorption, and ND-2PA spectroscopy. Adapted with permission from Chi, S-H., *Third-order Nonlinear Optical Properties of Conjugated Polymers and Blends*, Ph.D. Thesis, The Georgia Institute of Technology, December 2009. Copyright 2009 © Georgia Institute of Technology

Femtosecond transient absorption spectra were acquired using a commercial pump-probe spectroscopy system (Ultrafast Systems, Helios). The pump wavelengths were generated

in the same way as that for femtosecond Z- scan mentioned previously. The probe beam was a white-light continuum (WLC) (spectral range, 400-1600 nm) generated by splitting a portion (~5%) of the regenerative amplifier (Spitfire, Spectra-Physics) and focusing into either CaF₂ or CSi crystal depending on the desired spectral range. The probed signals were collected by a fiber optic cable coupled to a multichannel spectrometer with a Silicon (spectral range 400-900 nm) or InGaAs (spectral range 800-1600 nm) sensor. The measurable delay time window extended up to 3.2 ns. The pump beam was chopped at 500 Hz to obtain, sequentially, the reference WLC spectra (without pump) and the signal spectra (with pump) which allowed for the generation of the transient (ΔOD) spectra. The instrument response function (~200 fs) and the chirp correction function for WLC (applied to all data sets) were determined by measuring the neat solvent response. For solution measurements, the optical path length of the quartz cuvette used was 2 mm and the solution was stirred continuously throughout the acquisition.

2.2.4 Non-degenerate Two-Photon Absorption Spectroscopy

Nondegenerate two-photon absorption (ND-2PA) spectroscopy is a pump-probe technique where a broad continuum pulse is used to probe a sample that is subjected to an intense pump pulse. It is a single-shot technique where the large spectral extent of the probe beam could allow for full characterization of the sample.[96, 97] The principle behind operation is same as the transient absorption spectroscopy described above (**Figure 2.7**). For the purpose of this thesis, the technique is used to obtain the non-degenerate two-photon absorption cross section of the metal-terminated nonamethines,

TCF-terminated heptamethines – tricyanofuran-substituted cyanines with 7 carbons on the π -bridge, and alkyne-bridged cyanine samples to determine their applicability for nonlinear refraction based all optical switching.

The pump beam is typically higher in irradiance than the probe, thus the frequency of the pump is chosen such that it is less than that required for a degenerate two-photon transition (approximately half the transition energy), in hopes of avoiding possible linear absorption into the lowest lying excited state. The non-degenerate nonlinear absorption (ND-2PA) spectra are then plotted with respect to the total transition energy instead of the probe wavelengths, since the spectral position of probe absorption depends on the pump frequency involved in the non-degenerate two-photon absorption process. The transition energy is given by,

$$E_{transition} \propto \frac{1}{\lambda_{transition}} = \frac{1}{\lambda_{pump}} + \frac{1}{\lambda_{probe}} \quad (\text{Eq. 2.15})$$

Since the wavelengths of interest for telecommunications are between 1300 nm and 1550 nm, the probe used in the ND-2PA experiment is a NIR continuum covering 350 ~ 1600 nm. Once the absorption spectrum is plotted with respect to the transition energy, we can determine the states involved with the non-degenerate two-photon transition. With the transition energy identified, the ΔOD of the probe beam is then converted to the exponential loss factor Γ_0 . This loss factor is linearly proportional to the non-degenerate two-photon absorption coefficient, β_{ND} , which can then be converted to the ND-2PA cross-section, δ_{ND} , from which the imaginary part of macroscopic susceptibility can be extracted.

The critical parameters that will have an impact on ND-2PA can be obtained from the differential equations that describe the attenuation of the beams through the medium.[44]

$$\frac{dI_e}{dz} = -\alpha_e I_e - 2 \left(\frac{\omega_e}{\omega_p} \right)^{1/2} \beta_{ep} I_e I_p - \beta_{ee} I_e^2$$

$$\frac{dI_p}{dz} = -\alpha_p I_p - 2 \left(\frac{\omega_e}{\omega_p} \right)^{1/2} \beta_{ep} I_e I_p - \beta_{pp} I_p^2 \quad (\text{Eq. 2.16})$$

Where α and β represent linear and nonlinear absorption coefficient, and the subscripts e , and p denote the excitation (control) and probe (signal) beams respectively. In the above expression, the first and the last terms represent linear absorption and self-induced degenerate two-photon absorption, respectively. For our application, the wavelengths of the signal and the control beams are chosen such that the both linear absorption and the degenerate two-photon absorption are negligible. Thus, with these two terms ignored, the attenuations of the beams are described by two equations and two unknowns. Solving this system of equations, the probe energy transmittance – the ratio of transmitted and incident energies – can be explicitly expressed assuming negligible pump self TPA.[44]

$$T_p = \frac{\iint_{-\infty}^{\infty} I_p dA dt}{\iint_{-\infty}^{\infty} I_{p0} dA dt} = (1 - R_p)^2 \exp(-\Gamma_0) \quad (\text{Eq. 2.17})$$

$$\Gamma_0 \cong 2 \sqrt{\frac{\lambda_e}{\lambda_p}} \beta_{ep} (1 - R_e) I_{e0} L$$

The parameter R is the Fresnel reflection at the interface between the material and the air. The sample length is given by L . The nonlinear absorption coefficient β_{ep} can be obtained via the analysis of the total energy exchanged per unit time and volume between the light beams and the molecular ensemble and is given by the following.

$$\beta_{ND} = \frac{3\omega_p}{2\varepsilon_0 n_e n_p c^2} \text{Im} \left(\chi_{ep}^{(3)}(-\omega_p; \omega_p, -\omega_e, \omega_e) \right) \quad (\text{Eq. 2.18})$$

To convert the ΔOD obtained from the ND-2PA experiment into a cross-section, an arbitrary β_{ND} value is chosen, and iterated until the calculated probe transmittance, T_p agrees with the ΔOD observed. With the β_{ND} value established, one can simply convert this to cross-section using the following relationship,

$$\delta_{ND} = \frac{2\hbar\omega_p\beta_{ND}}{N} \quad (\text{Eq. 2.19})$$

where, N is the number density of absorbing molecules. The reason above expression holds true is because of the following definition, derived from the analysis of the energy exchanged per unit time and volume between the probe beam and the molecular ensemble. (The full derivation is beyond the scope of this thesis.)

$$\delta_{ND} = \frac{3\hbar\omega_p\omega_e}{N\varepsilon_0 n_e n_p c} \text{Im} \left(\chi_{ep}^{(3)}(-\omega_p; \omega_p, -\omega_e, \omega_e) \right) \quad (\text{Eq. 2.17})$$

As can be seen from these equations, non-degenerate two-photon absorption coefficient β_{ND} and the non-degenerate two-photon absorption cross-section δ_{ND} are directly proportional to the imaginary part of the third-order macroscopic susceptibility, $\text{Im}(\chi^{(3)})$, and thus, $\text{Im}(\gamma)$.

2.3 References

43. Sun, S.-S. and L.R. Dalton, *Introduction to organic electronic and optoelectronic materials and devices*. 2011: CRC Press.
44. Sutherland, R.L., *Handbook of nonlinear optics*. 2003: CRC press.
54. Hales, J.M., et al., *Design of Organic Chromophores for All-Optical Signal Processing Applications*. Chemistry of Materials, 2013. **26**(1): p. 549-560.
56. Orr, B. and J. Ward, *Perturbation theory of the non-linear optical polarization of an isolated system*. Molecular Physics, 1971. **20**(3): p. 513-526.
79. Lucarini, V., *Kramers-Kronig relations in optical materials research*. Vol. 110. 2005: Springer Science & Business Media.
80. Brée, C., A. Demircan, and G. Steinmeyer, *Kramers-Kronig relations and high-order nonlinear susceptibilities*. Physical Review A, 2012. **85**(3): p. 033806.
81. Boyd, R.W., *Nonlinear optics*. 2003: Academic press.
82. Mukamel, S., *Principles of nonlinear optical spectroscopy*. Vol. 29. 1995: Oxford University Press New York.
83. Onodera, H., I. Awai, and J.-i. Ikenoue, *Refractive-index measurement of bulk materials: prism coupling method*. Applied Optics, 1983. **22**(8): p. 1194-1197.
84. Ulrich, R. and R. Torge, *Measurement of Thin Film Parameters with a Prism Coupler*. Applied Optics, 1973. **12**(12): p. 2901-2908.
85. Tien, P.K. and R. Ulrich, *Theory of Prism-Film Coupler and Thin-Film Light Guides*. Journal of the Optical Society of America, 1970. **60**(10): p. 1325-1337.
86. Okamura, Y., S. Yoshinaka, and S. Yamamoto, *Measuring mode propagation losses of integrated optical waveguides: a simple method*. Applied Optics, 1983. **22**(23): p. 3892-3894.
87. Sheik-Bahae, M., A.A. Said, and E.W. Van Stryland, *High-sensitivity, single-beam n^2 measurements*. Optics letters, 1989. **14**(17): p. 955-957.

88. Sheik-Bahae, M., et al., *Sensitive measurement of optical nonlinearities using a single beam*. Quantum Electronics, IEEE Journal of, 1990. **26**(4): p. 760-769.
89. Milam, D., *Review and assessment of measured values of the nonlinear refractive-index coefficient of fused silica*. Applied optics, 1998. **37**(3): p. 546-550.
90. Krauss, T.D. and F.W. Wise, *Femtosecond measurement of nonlinear absorption and refraction in CdS, ZnSe, and ZnS*. Applied physics letters, 1994. **65**(14): p. 1739-1741.
91. Major, A., et al., *Ultrafast nonresonant third-order optical nonlinearities in ZnSe for photonic switching at telecom wavelengths*. Applied physics letters, 2004. **85**(20): p. 4606-4608.
92. Hutchings, D. and B. Wherrett, *Theory of anisotropy of two-photon absorption in zinc-blende semiconductors*. Physical Review B, 1994. **49**(4): p. 2418.
93. Hurlbut, W.C., et al., *Multiphoton absorption and nonlinear refraction of GaAs in the mid-infrared*. Optics letters, 2007. **32**(6): p. 668-670.
94. Villeneuve, A., et al., *Nonlinear absorption in a GaAs waveguide just above half the band gap*. Quantum Electronics, IEEE Journal of, 1994. **30**(5): p. 1172-1175.
95. Kuzyk, M.G. and C.W. Dirk, *Characterization techniques and tabulations for organic nonlinear optical materials*. 1998.
96. Negres, R.A., et al., *Two-photon spectroscopy and analysis with a white-light continuum probe*. Optics letters, 2002. **27**(4): p. 270-272.
97. Negres, R.A., et al., *Experiment and analysis of two-photon absorption spectroscopy using a white-light continuum probe*. Quantum Electronics, IEEE Journal of, 2002. **38**(9): p. 1205-1216.

CHAPTER 3

POLYETHINES WITH LARGE NONLINEAR REFRACTIVE INDEX, LOW LINEAR AND NONLINEAR OPTICAL LOSS IN NEAR INFRARED

3.1 Introduction

Organic materials with extensive π -systems such as donor-acceptor (D-A) substituted polyenes, polydiacetylenes, and polymethines were identified potential candidates for phase^{xv}-based AOSP early in the history of third-order NLO materials.[53, 98, 99] Their utilities, however, were limited by one or more of these factors: insufficient intensity-dependent refractive response ($n_2 \propto \text{Re}(\chi^{(3)})$), large linear absorption loss ($\alpha \propto \text{Im}(\chi^{(1)})$), and large two-photon absorption loss ($\beta \propto \text{Im}(\chi^{(3)})$). While some of these limitations imposed by the inherent electronic structures of the molecules, such as the competition between **N** term and **D** term in D-A polyenes, the primary phenomena responsible for these issues in polymethines are spontaneous symmetry breaking, and intermolecular electronic coupling via aggregation.

^{xv} a.k.a nonlinear refraction-, or nonlinear index-based

3.1.1 Spontaneous Symmetry-breaking

As discussed in Section 1.3, polymethines achieve maximal magnitude of molecular polarizability, γ , among the molecules of comparable lengths. Computational and experimental studies have shown that γ is predicted to scale as L^7 , where L denotes the length.[28, 52, 100] This pronounced length-dependence of γ in polymethines suggests that extension of the bridge conjugation length could be a facile strategy for enhancing nonlinear response. However, theoretical predictions, backed up by a significant body of experimental evidence suggest that polymethines beyond a certain critical length undergo a Peierls-type symmetry breaking wherein the charge localizes on one end of the molecule leading to significant BLA (**Figure 3.1**).[78]

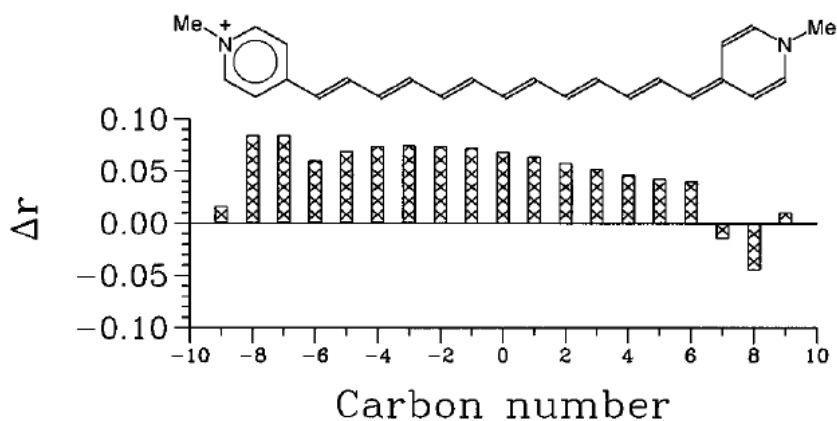


Figure 3.1. Example of spontaneous symmetry breaking in pyridinium tridecamethine. Δr denote the differences in the lengths of adjacent bonds at each carbon position. Reprinted with permission from the authors [78] (Copyright 1997 © American Chemical Society, *J. Chem. Am. Soc.*).

This charge localization causes a decrease in M_{ge} and a concomitant increase in E_{ge} leading to an overall reduction in $|\text{Re}(\gamma)|$, all while the molecule can also develop strong

two-photon absorption (2PA) bands. For example, pyridinium-terminated[78] and benzothiazolium-terminated[101] polymethines with 9 and 11 carbons in the central chain, respectively, both possess small E_{01} values of 1.26 and 1.14 eV, comparable to a recently reported selenopyrylium-terminated polymethines which showed a promising $\text{Re}(\gamma)$ of -4.4×10^{-32} esu and molecular figure-of-merit of 72,[62] far exceeding the requirement of 4π . However, both systems exhibited spectroscopic signatures indicating significant charge localization at these conjugation lengths. Hence, one of the major challenges in exploiting polymethines for AOSP is engineering molecules with sufficiently long delocalization lengths to generate strong NLO responses without succumbing to symmetry breaking.

3.1.2 Aggregation

The highly delocalized electronic nature of cyanine-like polymethines, while responsible for their large $|\text{Re}(\gamma)|$, also leads to extremely large linear polarizabilities, and, in turn, strong dipole – induced dipole, and induced dipole – induced dipole interactions which drive interchromophore aggregation, especially in concentrated or high-dielectric screening environments. With the exception of a few known cases involving growth-controlled pseudoisocyanine J-aggregate crystals,[102-104] aggregation deleteriously affects linear loss in material as the electronic coupling between dyes introduces new states, and the absorption band edges broaden in response to either or both directions. **Figure 3.2** depicts controlled formation of H- and J-type aggregate of benzimidazole-

terminated cyanine[105] and the corresponding linear absorption spectra showing the aggregate spectra no longer resembling that of the monomeric species.

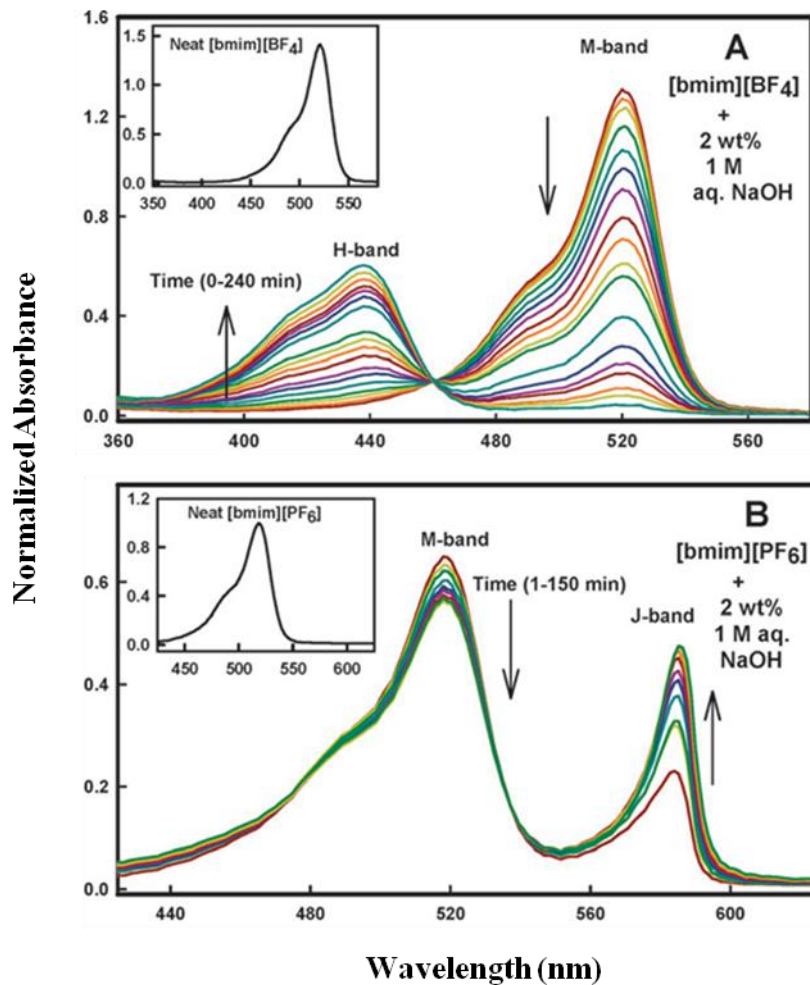


Figure 3.2. a) H- and b) J- aggregation bands in benzimidazolecarbocyanines induced using two different ionic liquids. The different colors in the spectra represent the emergence of aggregate bands in 12-minute interval. Reprinted with permission from the authors [105] (Copyright 2011 © RSC Publishing, *Chem. Commun.*)

Aggregation also has severe consequences on the nonlinear response of the material. $\text{Re}(\gamma)$ typically experiences a significant reduction as the overall M_{ge} decreases while the oscillator strength shifts away from the band responsible for resonant enhancement.

Moreover, the newly formed states are often two-photon active, either narrowing or closing of the two-photon transparency window, thereby decreasing the two-photon FOM (2PA-FOM). Hence, translating the molecular optical properties of promising polymethines into material properties in an aggregate-prone high-number density environment is another major challenge in the development of functional organic NLO materials for AOSP.

3.2 Effects of Metallation on the Optical Properties of *bis*(dioxaborine) (DOB)

Polymethines

One potential strategy to overcoming symmetry breaking is to modify the charge-stabilizing terminal groups such that they participate more efficiently in the overall conjugation length of the polymethine molecule. Terminal groups that possess good energy matching to the frontier orbitals of the conjugated bridge and provide large orbital overlaps for mixing of terminal group wave functions with the π -electron wave functions of the bridge should help delocalize charge throughout the molecule and minimize the impact of charge localization. This approach can enable the use of a shorter π -bridge to achieve the same degree of delocalization as a longer cyanine, circumventing the issue of symmetry breaking. Past investigations have revealed that dioxaborine^{xvi} is one such terminal group; Matichak et al. and Hales et al. concluded that dioxaborine(DOB)-terminated cyanines are less affected by symmetry breaking than other cyanines of

^{xvi} IUPAC name: 2,2-difluoro-4-phenyl-6-methyl-1,3,2(2H)-dioxaborine

comparable length while exhibiting very large, predominantly real values of γ . [106, 107]
 In particular, indane-substituted DOB nonamethine, and stilbene-substituted DOB
 heptamethine exhibited very large $|\gamma|$ of 5.4×10^{-32} and 7.0×10^{-32} esu at 1300 nm. [106,
 107]

On the basis of this previous finding, the next logical aim would be to further increase γ
 by stabilizing the LUMO of these cyanines using the electron withdrawing influence of
 positively charged metal fragments. While several polymethines substituted with charge-
 stabilizing organometallic terminal groups such as $[\text{RuCl}(\text{dppe})(\text{PPh}_3)(\text{CO})]$ or
 $[\text{Cp}_2\text{Fe}_2(\text{CO})_3\text{C}]$ have been reported, [108, 109] the role of these metal complexes on
 linear and nonlinear optical properties has not been investigated to our knowledge. To
 understand the impact of metal complexation on the linear and nonlinear molecular
 optical properties, a pair of group IX metals, rhodium and iridium, have been coordinated
 to the bipyridine post-terminal group of DOB heptamethines. (**Figure 3.3**)

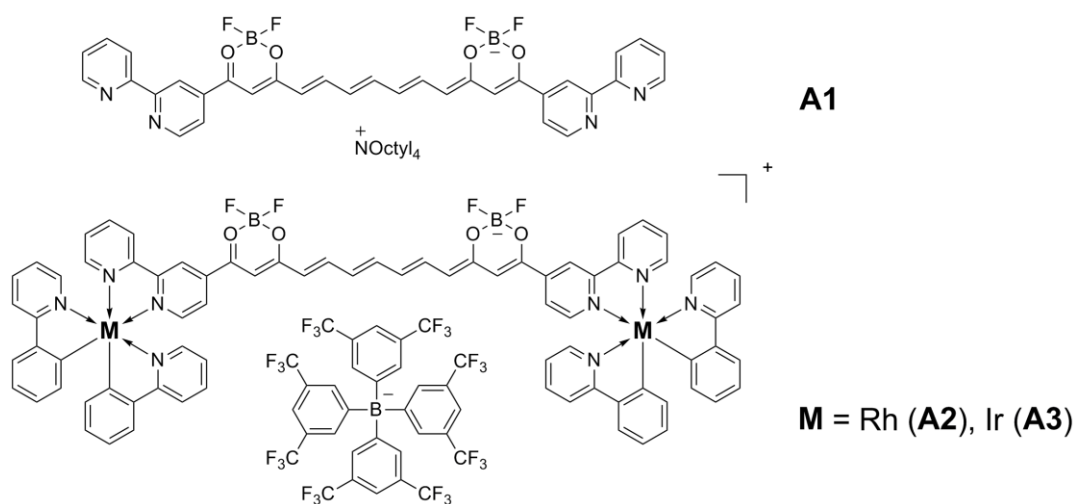


Figure 3.3. The chemical structures of bis(2,2'-bipyridyl dioxaborine)heptamethines. A1: model compound, A2: rhodium-terminated, and A3: iridium-terminated

3.2.1 Linear Optical Properties

The linear absorption spectra of **A1-3** in dichloromethane and in the solid state are shown in **Figure 3.4**; some of their optical parameters are compared in **Table 3.1**. The visible-near-IR spectra of **A1-3** in solution all show sharp electronic absorption edges and well-resolved vibronic structures, similar to what has been observed for the $S_0 \rightarrow S_1$ transitions of other symmetrical dioxaborine (DOB)-terminated polymethines;[106, 110-112] however, the vibronic structures of these compounds are less strongly peaked than those of typical cyanines. Incorporation of metal terminal groups beyond the DOB in **A2** and **A3** leads to bathochromic shifts in the absorption maxima with respect to the model compound **A1**, with concomitant decreases in the corresponding absorptivities and transition dipole moments. Presumably, the bathochromic shifts are due in part to the electron-withdrawing influence of the positively charged Rh and Ir fragments leading to stabilization of the LUMO,[106] and in part to planarization of the bipyridyl unit upon complexation.

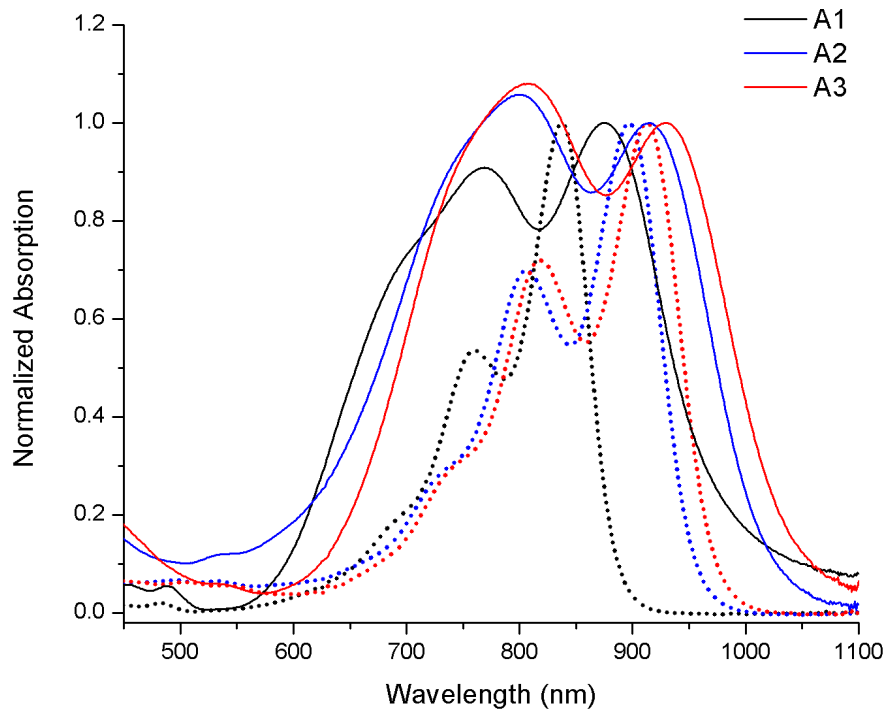


Figure 3.4. Normalized linear absorption spectra of a) A1, b) A2, and c) A3 in CH_2Cl_2 (dashed) and in neat films (solid).

The absorption spectra of neat films of **A1-3** (**Figure 3.4**) resemble that of a proton sponge salt of an anionic *bis*(dioxaborine)-terminated nonamethine[107] in that the main absorption bands are broadened and split relative to their corresponding solution spectra. However, the solid state spectra of **A2** and **A3**, although still broad compared to the solution spectra, are characterized by low-energy (0,0) band that are closer in wavelength to the corresponding solution peaks with less than 20 nm red-shift than in the case of the model compound **A1** which shows 40nm red-shift or other previously reported nonamethine which similarly showed large red-shift. Moreover, the solid-state absorption onset is sharper and the long-wavelength tailing is reduced in **A2** and **A3** compared to

A1, likely due to the bulkier end groups serving both to modify the intermolecular interactions that limit the distribution of available aggregate geometries and to reduce crystallinity which can lead to scattering loss. These results demonstrate that incorporation of bulky metal complexes into *bis*(dioxaborine) polymethines can lead to bathochromic shifts of the solution absorption maxima without compromising the near-IR transparency of the corresponding films.

Table 3.1. Linear and nonlinear optical properties of **A1-3**

	λ_{\max}^a (nm)	$\epsilon_{\max} (\times 10^5$ $M^{-1} \text{ cm}^{-1})$	M_{ge}^b (D)	$\text{Re}(\gamma)^c$ ($\times 10^{-32}$ esu)	$\text{Im}(\gamma)$ ($\times 10^{-32}$ esu)	$\lambda_{\max, \text{film}}$ (nm)
A1	830 (760) ^d	2.6 (1.4)	19	-1.0	1.6	875 (768)
A2	897 (806)	1.6 (1.1)	16	-1.3	1.3	916 (800)
A3	912 (819)	1.6 (1.1)	16	-1.6	1.7	930 (809)

^a Measured in CH₂Cl₂. ^b Obtained from main absorption band using $\mu_{ge}=0.09854[\int(\epsilon/\nu)d\nu]^{0.5}$ where ϵ is in $M^{-1} \text{ cm}^{-1}$, ν in cm^{-1} , and the transition moments are expressed in debye (D). ^c Measured at 1.55 μm ; errors $\pm 10\%$. ^d The values in brackets denote the contribution from the vibronic shoulder ^e Due to the presence of impurities in the sample of A2, the values in the table are lower limits on the magnitudes of the quantities.

3.2.2 Nonlinear Optical Properties

The nonlinear optical parameters measured using fs- pulsed Z-scan are also shown in

Table 3.1. The magnitudes of $\text{Re}(\gamma)$ of all three heptamethines were found to increase linearly with the excitation irradiance, suggesting the presence of contribution from

excited-state refraction. Therefore, the values of $\text{Re}(\gamma)$ reported in **Table 3.1** were determined from linear extrapolation to zero excitation irradiance. On the other hand, the values of $\text{Im}(\gamma)$ did not show the same degree of irradiance dependence, suggesting minimal contributions from excited-state absorption. These results are consistent with the transient absorption spectra that show a detuning of nearly 100nm between the excitation wavelength and the peak of the excited state absorption band, $E_{ee'}$. (**Figure 3.5**) The magnitudes of the $\text{Re}(\gamma)$ for heptamethines all three DOB cyanines are quite large, and can be compared with the value of -5.3×10^{-32} esu that have been reported for an anionic DOB nonamethine at the same wavelengths. [107]

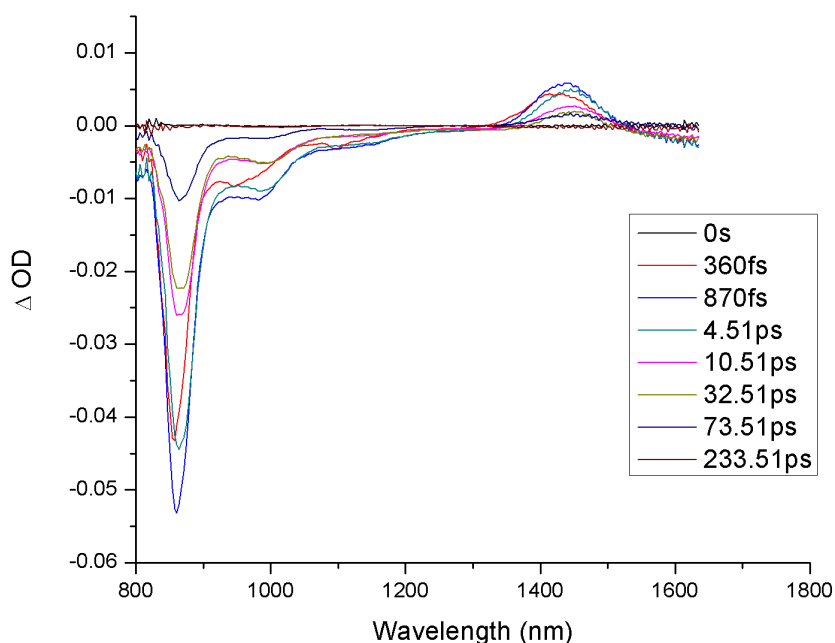


Figure 3.5. Transient absorption spectrum of **A1** in CH_2Cl_2 ; the sample concentration, 9.3 μM ; the pump wavelength, 830 nm; pump energy, 4.1 μJ . The negative signal at ca. 1000 nm is assumed to be due to stimulated emission.

The magnitudes for $\text{Re}(\gamma)$ at $1.55\mu\text{m}$ for the metal terminated polymethines **A2**, and **A3** are 30 and 60% larger than that of the metal-free **A1**. This result is in contrast with the estimates from the zero-frequency values of γ obtained from the two-state model^{xvii} using M_{ge} of **A2** and **A3**, which predicted that the γ for **A2** and **A3** should be around 70% of that of **A1**. This implies that significant two-photon dispersion enhancement, likely from the $|\text{vb}\rangle$ state, (Section 1.3, **Figure 1.5**) is responsible for the increase in the magnitude of $\text{Re}(\gamma)$ upon metal-complexation. Indeed, the values of $\text{Im}(\gamma)$ at $1.55\mu\text{m}$ indicate significant two-photon absorption at this wavelength for all three chromophores, with the corresponding two-photon cross-sections varying from 860-1140 GM. ($\text{cm}^4\text{ s photon}^{-1}\text{ mol}^{-1}$)

3.3 Effects of Out-of-Plane Steric Bulk Substitution on the Optical Properties of Chalcogenopyrylium-terminated Heptamethines

A selection process that would allow for identification of terminal groups with the largest effective number of π -electrons could facilitate the discovery of optimal molecular candidate for nonlinear index-based AOS. This can be accomplished by applying a free electron model for the absorption behavior of vinylogous sets of polymethine molecules with different terminal groups.[113] By fitting the evolution of M_{ge} and E_{ge} versus the effective conjugation length, L , and its inverse, $1/L$, for a variety of vinylogous polymethines, it has been found that among all the terminal groups, the selenopyrylium

^{xvii} $\gamma(0) \propto -M_{ge}^4 / E_{ge}^3$

exhibits the optimal values of E_{ge} and M_{ge} for a given effective conjugation length, L .

(Figure 3.6)

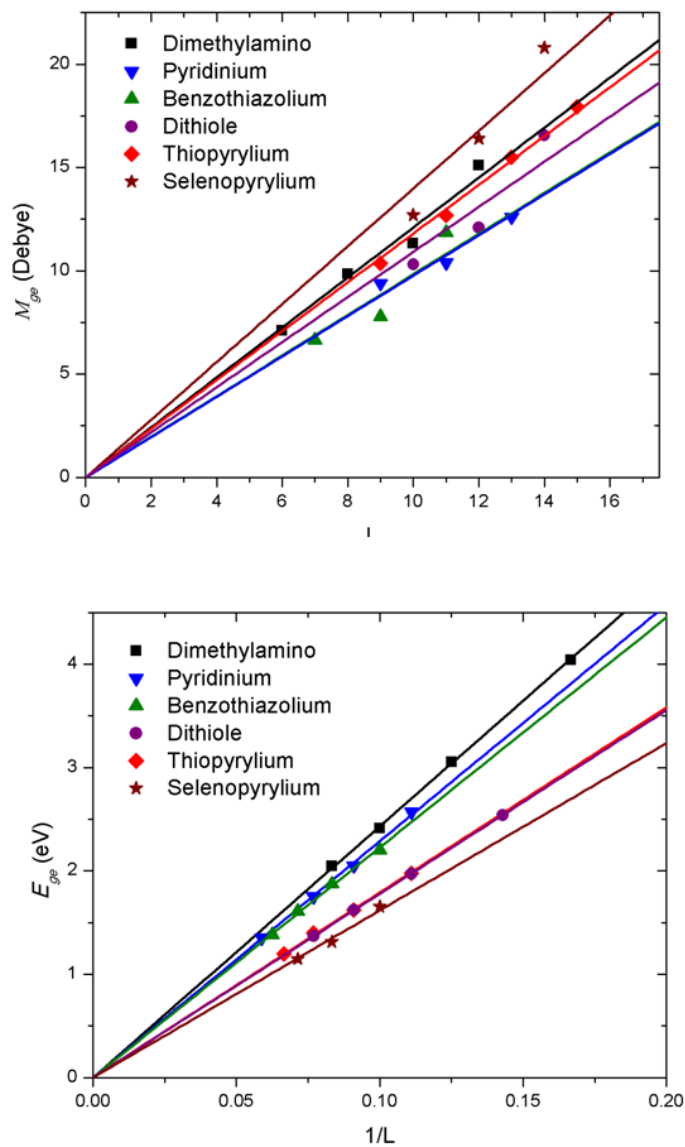


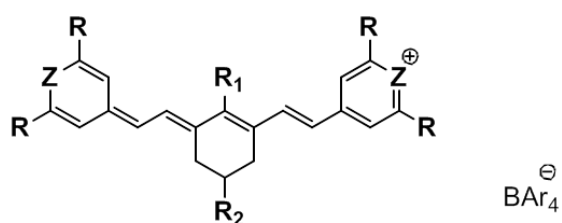
Figure 3.6. M_{ge} vs L (top) and E_{ge} vs $1/L$ (bottom) for symmetrically substituted polymethines with various terminal groups. Plot of dimethylamino-, pyridinium-, benzothiazolium-, dithiole-terminal groups adapted with permission from the authors.

[62] (Copyright 2010 © AAAS, *Science*)

These results indicate that the selenopyrylium-, and chalcogenopyrylium- groups by extension, should be effective at delocalizing charge throughout the molecule. Given that this group contains the heaviest and most polarizable atom of all the heterocyclic terminals, one would expect sizable mixing of the terminal π -orbital with the π -conjugated bridge coupled with an increase in the transition density towards the periphery of the molecule. SAC/SAC-CI quantum chemical calculations confirm this observation, revealing an appreciable electron density in the frontier orbitals of the terminal groups.[62] Consequently, the dominance of the N term (Section 2.2.1) in the NLO response and its steep dependence on E_{ge} and M_{ge} gives rise to unprecedentedly large values of $|\text{Re}(\gamma)|$ for chalcogeno-polymethines throughout the near-IR, exceeding those of other promising organic molecules including a dioxaborine (DOB)-terminated nonamethine, polarized carotenoids,[114] and other D-A polyenes.[115] Furthermore, the highly delocalized nature of the chalcogenopyrylium polymethines suggests that these molecules should possess the large two-photon transparency region alluded to in section 1.3.

With an ideal molecular platform identified, the focus of recent investigations has been on developing methods to impart polymethines strong resistance to aggregation. This section describes one such approach; the “end”, “front”, and/or “back” positions of the chalcogenopyrylium heptamethines are substituted with groups that are i) moderately-sized, ii) fairly rigid and attached to the chromophore without intervening the flexible groups, and iii) project above and below the plane of the π -system. (**Figure 3.7**) While similar approaches have been investigated with thiopyrylium-terminated polymethines using Fréchet-type dendron substitution of flexible benzyl aryl ether at the “front” site to

limit the aggregation effect, the films cast with these dyes still showed moderate band broadening associated both H- and J-type aggregation, and exhibited unacceptably large linear losses in the telecommunication region.[116] The “end”, “front”, and “back” groups chosen for this investigation are comparatively more rigid, and more pronounced in protrusion out of the plane of the π -bridge. The substitution scheme for this investigation is shown in **Figure 3.7**.



Compound	Chalcogen Z	“End” R	“Front” R ₁	“Back” R ₂
B1	S	Ph	Cl	H
B2	S	tBu	Cl	H
B3	S	Ph	cbz	H
B4	S	tBu	cbz	H
B5	S	tBu	cbz	fl
B6	S	tBu	cbz	tBu
B7	S	Ad	cbz	tBu
B8	Se	Ad	cbz	tBu

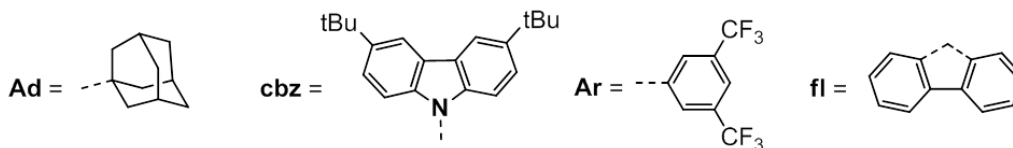


Figure 3.7. Rigid steric group substitution scheme for chalcogenopyrylium-terminated polymethines.

3.3.1 Linear optical properties

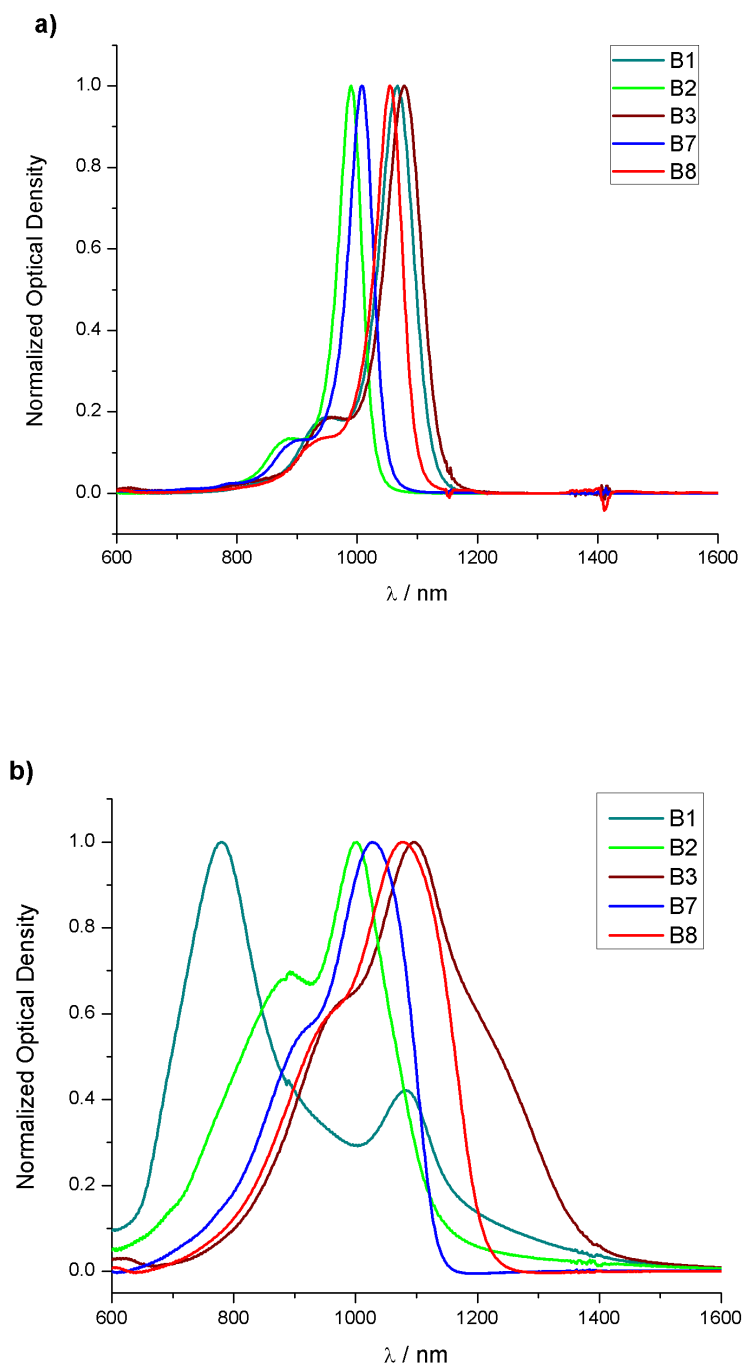


Figure 3.8. Normalized absorption spectra of chalcogenopyrylium heptamethines in a) dilute chloroform solution and b) in 50 wt% blends with amorphous polycarbonate (APC)

Figure 3.8 shows the 1PA spectra for a few of the dyes in dilute solutions and in films at 50 wt% in an amorphous polycarbonate (APC) host. The thin-film spectra of **B1**/APC exhibits broad features significantly displaced to both the low- and high-energy sides of the solution absorption band; batho- and hypso-chromic shifts are generally attributed to J- and H- aggregations, respectively,[117, 118] while the large bandwidths seen here likely reflect a distribution of aggregate geometries. Replacement of the phenyl “end” groups of **B1** with out of plane, non-conjugated *tert*-butyl (tBu) groups results in a low-energy absorption maximum for **B2**/APC similar to that observed in solution spectrum, while substantially suppressing the low energy tail.

Use of the large out-of-plane 3,6-di(*tert*-butyl)carbazol-9-yl (cbz) group in the “front” (R') position tends to suppress broadening on the high-energy side of the film spectra (**B3** vs. **B1**; **B6** vs. **B2** **Figure 3.9**), indicating that H-type aggregation can be prevented using this approach. In the case of **B3**/APC (R = Ph) there is a pronounced low-energy shoulder with a rather narrow linewidth compared to the broad tail of **B1**; we attribute this to a more well-defined J-aggregate geometry. Bulky groups in the “back” position(s), R₂, (**Figure 3.7**) primarily affect the film spectra on the high-energy side of the main peak (**B6-8**). In summary, bulky “end” groups drastically reduce the J-aggregate-like absorption and the “front” groups (and to a lesser extent “back” groups) reduce the H-aggregate-like absorption. Importantly, when bulky R, R₁, and R₂ groups are all present, the spectra of the APC blend films are narrowest and most solution-like. Similar trends are observed in the spectra of neat chromophore films (**Figures 3.9**).

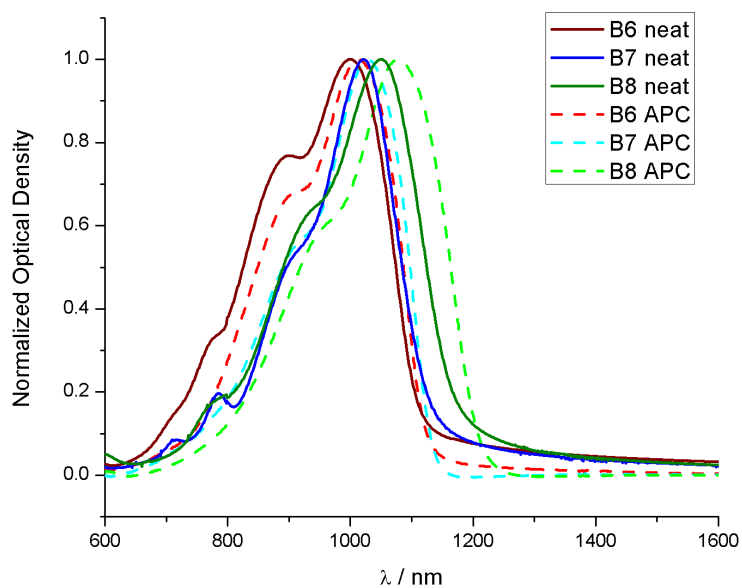
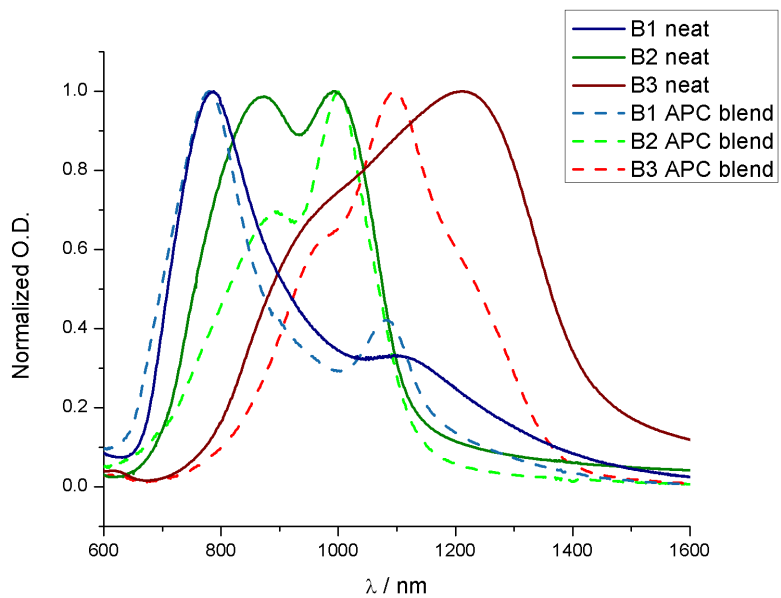


Figure 3.9. Linear absorption spectra of neat films (solid) and 50 wt% dye-APC blends (dashed)

The spectra of neat films are broader than those of the APC blends in all cases. This broadening is particularly apparent in the less heavily substituted compounds **B1**, **B2**, and **B3**. Compared to the solution spectrum, the film spectra of the unsubstituted compound **B1** shows significant broadening and shifting of the bands in both directions. Dilution of **B1** in APC host polymer had only minor impact on the absorptive behavior. The neat film of **B2**, lacking the “front” group, shows strong H-type aggregation, as show by the significant shift in the oscillator strength to the higher energy band. Dilution of **B2** in APC results in a less pronounced blue-shifted feature, suggesting a reduction in H-aggregate formation. Compound **B3**, lacking the rigid “end” group, shows a significant broadening of the spectrum in the lower energy region, ($\lambda > 1300\text{nm}$) attributable to J-type aggregation. The broadening of the band in the near IR region is significantly more pronounced in the neat film than in the APC blend, in which a peak is retained at a similar wavelength to that see in solution and the red-shifted band (at $\sim 1270\text{ nm}$) is relatively narrow, suggesting a more well-defined J-aggregate geometry. For **B4-8**, the spectra in neat films and in APC blends are very similar, further corroborating that, with less heavily substituted cyanines, the dilution in APC is an impactful approach.

Table 3.2. Linear and nonlinear^a optical properties of chalcogenopyrylium-terminated heptamethines at 1550 nm in chloroform and in films (50 wt% in APC unless otherwise stated)

Cpd	Solution		Film				Linear loss ^c (dB cm ⁻¹)
	λ_{\max} (nm)	Re(γ) ($\times 10^{-32}$ esu)	Re(γ)/Im(γ)	Re($\chi^{(3)}$) _{ex} ^b ($\times 10^{-11}$ esu)	Re($\chi^{(3)}$) ($\times 10^{-11}$ esu)	Re($\chi^{(3)}$)/Im($\chi^{(3)}$)	
B1	1067	-3.2	35	-4.2	-1.5	^d	>20 ^e
B2	990	-1.8	11	-2.9	-2.4	4.6	5.6
B3	1078	-2.4	30	-3.2	-8.6	11	8.5
B4	997	-1.8	13	-2.5	-2.6	8.6	10
B5	988	-1.6	9	-2.1	-2.5	6.0	4.1
B6	997	-1.7	13	-2.3	-2.7	12	3.5
B7	1008	-2.0	14	-2.1	-2.4	13	3.4
B8	1055	-2.2	36	-2.6	-3.3	12	4.4
B8 (neat)				-5.2	-5.1	21	8.2

^a Determined using the fs Z-scan technique. Experimental uncertainties are $\pm 8\%$ for Re(γ), $\pm 11\%$ for |Re(γ)/Im(γ)|, $\pm 13\%$ for Re($\chi^{(3)}$) and $\pm 18\%$ for |Re($\chi^{(3)}$)/Im($\chi^{(3)}$)|, for details refer to Appendix. ^b Estimated by using the solution value of Re(γ), the local field factor, and the concentration of the film. ^c Determined using prism coupling. The loss measured for a pure APC film is 1.9 dB cm⁻¹. ^d Im($\chi^{(3)}$) not determined due to significant linear absorption. ^e Loss exceeding the instrumental detection limit.

3.3.2 Nonlinear optical properties

Table 3.2 compares the solution molecular NLO parameters for **B1-B8** at 1550nm. The molecular polarizability of compound **B1** has been reported previously,[62] and serve as a reference for comparison with its large $|\text{Re}(\gamma)|$ and $|\text{Re}(\gamma)/\text{Im}(\gamma)|$. At the concentrations employed (<5 mM), aggregation is not expected to be significant and so variations in $\text{Re}(\gamma)$ and $\text{Im}(\gamma)$ can largely be ascribed to substituent effects on the $S_0 \rightarrow S_1$ (1PA) band position. $\text{Re}(\gamma)$ is primarily influenced through near-resonant enhancement, increasing with reduced detuning between the excitation photon energy and the energy of S_1 state. The effective conjugation length is somewhat reduced upon replacing the aryl “end” groups with alkyl “end” groups; accordingly λ_{max} and $|\text{Re}(\gamma)|$ are largest for **B1** and **B3** and smallest for **B4** through **B6**. $|\text{Re}(\gamma)/\text{Im}(\gamma)|$ is also sensitive to the $S_0 \rightarrow S_1$ transition energy. Although 2PA into the S_1 state of cyanine-like dyes is electronically forbidden, significant vibronically assisted 2PA into S_1 is generally observed, with the peak transition energy approximately 0.2eV higher than the 1PA peak energy: [59, 62] the hypsochromic shift of λ_{max} seen for **B2** and **B4 –B7** relative to **B1** brings this 2PA peak closer to twice the energy corresponding to the 1550 nm laser wavelength, resulting in a reduction in $|\text{Re}(\gamma)/\text{Im}(\gamma)|$. Thus, although changing “end” groups from phenyl to tert-butyl significantly improves the linear spectra of films by reducing the overall absorption tail at 1550 nm, it leads to poorer *molecular* 2PA-FOMs for **B2** and **B4-7** than **B1** and **B3**. However, the $S_0 \rightarrow S_1$ absorptions of selenopyrylium dyes are bathochromically shifted relative to those of their thiopyrylium analogue **B7**. [119] This leads to greater near-resonance enhancement of the $\text{Re}(\gamma)$, and consequently the molecular 2PA-FOM of

the selenopyrylium dye **B8** is larger than that of its thiopyrylium analogue **B7** and is similar to those for **B1** and **B3**, while the film spectra of **B8** (**Figure 3.8**) demonstrate considerably reduced aggregation relative to **B1** and **B3** due to the bulkier substitution pattern.

Table 3.2 also includes linear optical loss and NLO data for films composed of 50 wt% chromophore/APC blends at 1550nm. The low-energy tail in the spectrum of **B1/APC**, attributed to J-like aggregation, results in exceedingly large linear losses; these are reduced considerably through “end” group substitutions, as seen in the films spectra of **B2/APC**, while “front” and “back” substitutions further reduce the optical losses. (**B5-8/APC**). H-type aggregation in the **B1/APC** film results in $\text{Re}(\chi^{(3)})$ value significantly smaller than that extrapolated from its dilute solution, $\text{Re}(\chi^{(3)})_{\text{ex}}$. Conversely, for many of the films where “front” substitution effectively inhibits formation of H-type aggregates, the $\text{Re}(\chi^{(3)})$ values are fairly similar to the values of $\text{Re}(\chi^{(3)})_{\text{ex}}$. Blend films with thiopyrylium chromophores having out-of-plane R, R', and R'' substituents also exhibit macroscopic 2PA-FOMs very similar to those observed in dilute solutions. Film 2PA-FOMs are generally slightly lower than found in solutions. The vibronic shoulders of the thin-film spectra are stronger than those seen in solution; this may be due to increased vibronically assisted 2PA in the films. Remarkably, films of **B3/APC** exhibits nonlinearity far exceeding those extrapolated from solution. We attribute this to the strong J-aggregate-like low-energy absorption band centered around 1270 nm. (**Figure 3.8**) Moreover, the width of this band is sufficiently narrow such that it does not impact the linear optical loss as severely as the broad and less well-defined low energy absorption seen for **B1/APC**. Films of **B8/APC** exhibit the expected increase in $|\text{Re}(\chi^{(3)})|$

compared to its thiopyrylium analogue **B7**/APC, while simultaneously exhibiting a two-photon FOM suitable for AOSP and low optical losses. Interestingly a neat film of **B8** give two-photon FOM even larger than **B8**/APC, suggesting either 1) presence of crystalline domains with well-defined orientations of the dyes in the neat film that pushes the two-photon absorption band away from the pump wavelength of $1.55\ \mu\text{m}$, or 2) the APC is the not most optimal host in preventing broadening of vibronic shoulder and the associated two-photon loss.

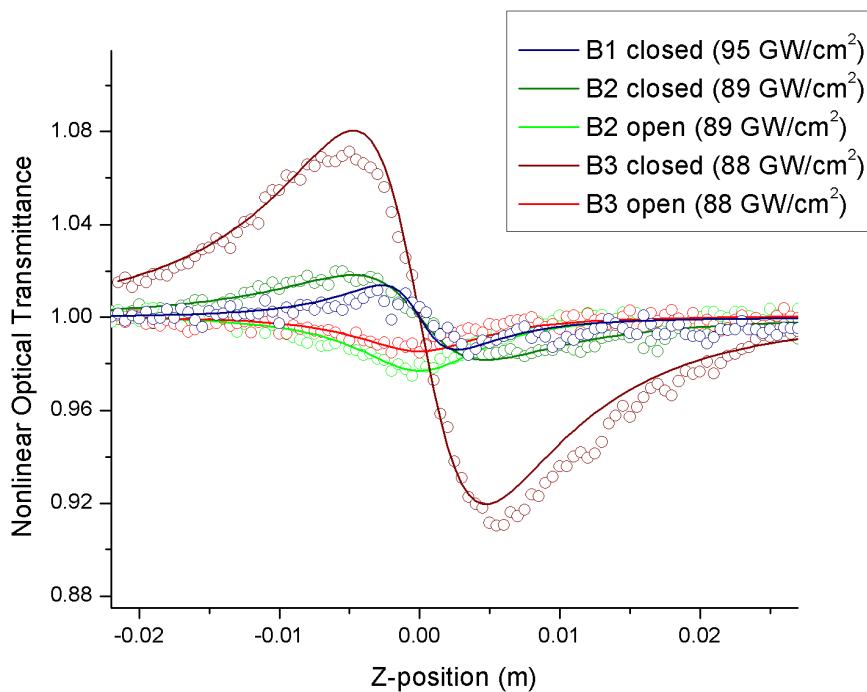


Figure 3.10. Closed (following the division by open aperture scan) and open aperture Z-scans of selected 50 wt% dye/APC blends at 1550nm

As seen from the **Table 3.2**, the values of the $\text{Re}(\gamma)$ scale with the λ_{max} of the solution spectrum as expected from the detuning between the excitation photon energy and the energy of the S1 state. (Section 1.3) The macroscopic susceptibility, $\chi^{(3)}$, also shows the corresponding increase with increasing λ_{max} , with the exception of **B1** and **B3**. The film of **B1** shows significant reduction of the expected value of $\text{Re}(\chi^{(3)})$ while that of **B3** shows significant amplification of this value. The reduction of optical nonlinearity seen in the film of **B1** and the increase in **B2** can be explained by their respective linear absorption spectra. **Figure 3.10** shows representative Z-scan plots which reveal the differences in the magnitude of the signals under identical experimental conditions, showing nearly a five-fold increase in the closed aperture signal from the film of **B3** with respect to that of **B1** and **B2**.

3.4 Effects of Square-planar “Front” Substituents on the Optical Properties of Chalcogenopyrylium-terminated Heptamethines

The films containing the modified chalcogenopyrylium dye molecules from the previous section exhibited reduced aggregation in high number density films along with a concomitant improvement in the linear and NLO properties compared to films containing heptamethines without substitution of the bulky groups. Furthermore, a number of the investigated dyes, namely **B6**, **B7**, and **B8** showed macroscopic solid-phase NLO values, as well as the two-photon absorption figure-of-merit (2PA-FOM), required for an effective NLO material for silicon-organic hybrid optical switching devices. For these dyes, the linear losses were in the range of 3.5 to 4.5 dB/cm.[120] While these levels of

linear losses are considered acceptable, with a lower linear loss, it may be possible to increase the loading density of the chromophores in the host polymer to achieve even greater macroscopic third-order susceptibility, $\chi^{(3)}$. Hence, a novel synthetic approach using a bulky steric substituent with a well-defined atomic connectivity to the cyanine bridge was undertaken to mitigate aggregation, thereby improving the transparency of the film at telecommunication wavelengths.

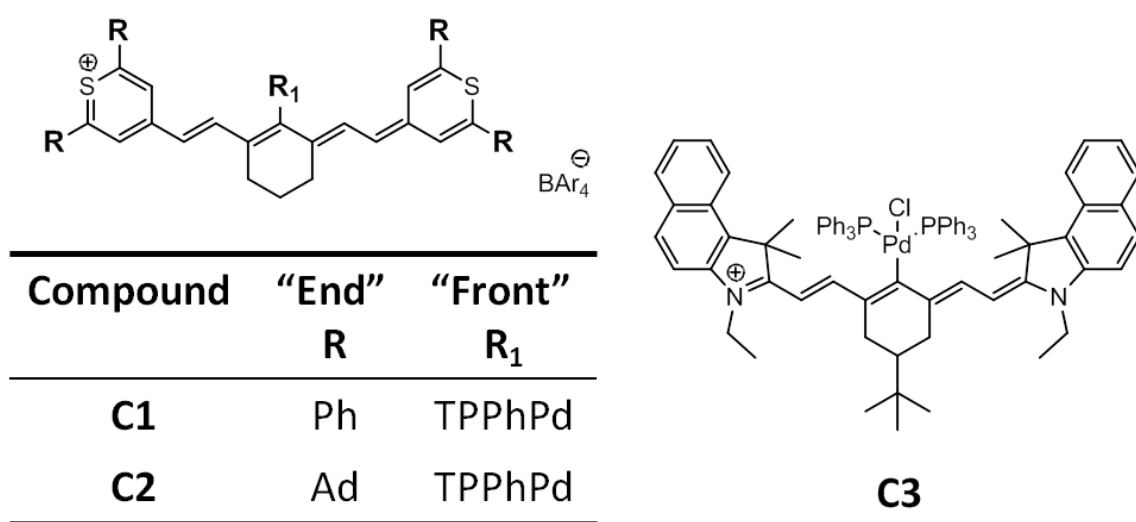


Figure 3.11. Structures of *bis*(triphenylphosphine)palladium-modified (left) thiopyrylium and (right) *bis*(benzoindole)thiopyrylium polymethines.

Table 3.3 summarizes both micro- and macroscopic NLO properties of various chromophores modified with *bis*(triphenylphosphine)palladium (TPPhPd). The novelty of these particular group 10 transition metal containing substituents is that it forms a square-planar complex with the central cyanine chain unit. It is hypothesized that bulky triphenylphosphine group will assume a completely orthogonal orientation with respect to the cyanine bridge, imparting a necessary intermolecular distance to inhibit aggregation.

As seen from the **Figure 3.11**, compound **B1**, **B3**, and **C1** are structural analogues sharing the identical terminal groups, *bis*(diphenylthiopyrylium) with only variations being the “front” substituent. Compared to the unsubstituted **B1** and carbazole substituted **B2**, the TPPhPd substituted cyanine **C1** exhibits an appreciable hypsochromic shift of λ_{\max} . This shift increases the detuning of the 1PA resonance from the 1550 nm beam, and reduces the near-resonance enhancement of the magnitude of $\text{Re}(\gamma)$. Interestingly, the impact of such blue-shift on $\text{Re}(\chi^{(3)})$ is not as drastic as expected as can be seen from the discrepancy between solution extrapolated and experimentally determined $\text{Re}(\chi^{(3)})$ s.

Table 3.3. Linear and nonlinear^a optical properties of *Bis*(triphenylphosphine) – palladium substituted heptamethines at 1550nm in chloroform and in 50 wt% films

	Solution			Film			Linear loss (dB cm ⁻¹)
	λ_{max} (nm)	Re(γ) ($\times 10^{-32}$ esu)	Re(γ)/Im(γ)	Re($\chi^{(3)}$) _{ex} ($\times 10^{-11}$ esu)	Re($\chi^{(3)}$) ($\times 10^{-11}$ esu)	Re($\chi^{(3)}$)/Im($\chi^{(3)}$)	
APC	-	-	-	-	0.0066	-	1.9
B1	1067	-3.2	35	-4.2	-1.5	^b	>20 ^c
B3	1078	-2.4	30	-3.2	-8.6	11	8.5
C1	998	-0.94	11	-1.1	-2.1	4.1	7.1
C2	993	-1.5	13	-1.6	-2.9	18	4.1
C3	807	-1.3	^d	-1.3	-2.4	12	2.0

^a Determined using the fs Z-scan technique. Experimental uncertainties are $\pm 8\%$ for Re(γ), $\pm 11\%$ for |Re(γ)/Im(γ)|, $\pm 13\%$ for Re($\chi^{(3)}$) and $\pm 18\%$ for |Re($\chi^{(3)}$)/Im($\chi^{(3)}$)|, for details refer to Appendix. ^b Im($\chi^{(3)}$) not determined due to significant linear absorption. ^c Loss exceeding the instrumental detection limit. ^d The two-photon absorption coefficient, β , hence, Im(γ), below the detection limit of the fs Z-scan

The most importance consequence of the TPPhPd substitution is the reduction of the linear losses in the films. With just the “front” group modification alone, the linear loss of the film containing bis-diphenylthiopyrylium dye (**B1**, **B3**) improves from > 20 dB/cm to 7.1 dB/cm. When other promising cyanines dyes with different terminal groups such as *bis*(adamantyl)thiopyrylium (**C2**), and *bis*(benzoindole)thiopyrylium (**C3**) were modified using TPPhPd group, the linear loss values approach that of the neat host polymer (APC) film, while simultaneously satisfying the requisite two-photon absorption FOM. The remarkably low linear loss is most likely due to a combination of the greater detuning from the one-photon absorption resonance, and their solution like linear absorption spectra in films as seen in **Figure 3.12**.

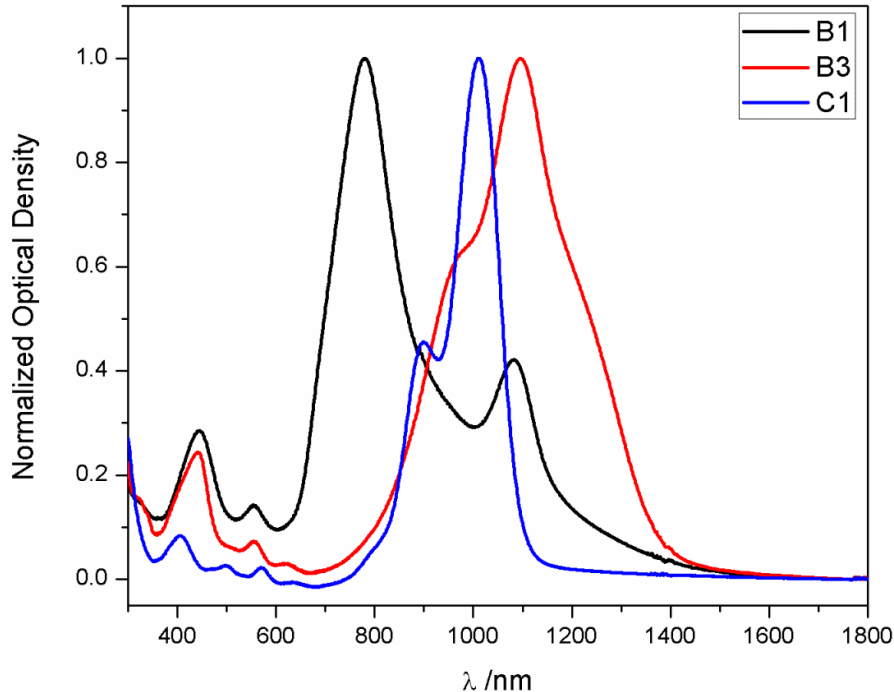


Figure 3.12. Normalized linear absorption spectra of 50 wt% dye/APC blend films; 80nm in thickness

3.5 Summary

In Section 3.2 we have demonstrated that a new type of transition metal functionalized polymethines is able to extend the effective delocalization without incurring spontaneous symmetry breaking as predicted and, at least for the particular counterion used here, potentially narrow the distribution of aggregate geometry, as evidenced by increased linear transparency in the near IR. Although the post-terminal metal coordination results in noticeable increases in the $\text{Re}(\gamma)$ at $1.55\mu\text{m}$, in all three chromophores, $\text{Im}(\gamma)$ exhibited comparable increase magnitude, indicating that even if these microscopic values were to be translated to the solid state, these particular compounds would exhibit unacceptably high nonlinear optical losses for AOSP applications.

While comparable or even higher values of $|\text{Re}(\chi^{(3)})|$ have been demonstrated in other organic materials at telecommunications wavelengths, including polyacetylene derivatives[121] and polymethines with dioxaborine[107] and tricyanofuran[122] termini, these have been accompanied by larger linear and/or nonlinear losses. Conversely, an arylethynyl aryl tetracyanobutadiene exhibits excellent loss parameters, but $|\text{Re}(\chi^{(3)})|$ smaller than for the present compounds.[123] Films of the chalcogenopyrylium heptamethines **B6–8**/APC blends and of neat **B8** show a unique *combination* of large $|\text{Re}(\chi^{(3)})|$, 2PA-FOM that meets or exceeds the required value for AOSP, low linear optical loss, and, importantly for device applications, solution processability. In conclusion, through a design strategy aimed at reducing interchromophore aggregation, cyanine-like dyes can be engineered to afford the requisite optical properties for phase-based AOSP: large $|\text{Re}(\chi^{(3)})|$, acceptable 2PA-FOMs, reasonably low linear losses, and

good photostability arising from low photoreactivity combined with minimal 1PA and 2PA absorption at 1550 nm. In the case of **B3**/APC, control of the nature of the aggregation led to a larger $|\text{Re}(\chi^{(3)})|$ value than anticipated from solution data without incurring unacceptable loss. Thus this work represents a critical step in the development of third-order NLO materials; the approach may also be used to inhibit deleterious intermolecular interactions in other organic photonic and electronic applications.

The substitution of square-planar *meso-bis*(triphenylphosphine) palladium onto the bridge positions of heptamethine molecules has resulted in dramatically reduced linear loss in high number density films. The palladium complex substituent is highly effective to the extent that when attached to a benzoindole terminated cyanine, the linear loss of the cyanine blend film is indistinguishable from that of the host polymer, APC. As the benzoindole polymethine dyes substituted with TPPhPd show a rare combination of exceptionally low linear loss and good two-photon FOM, the investigation of the effect of increasing the loading density is underway. Additionally, it was also found that these dyes are less stable in ambient conditions than the carbazole(cbz)-substituted predecessors and thus methods for improving their stability are also being investigated.

3.6 Experimental details

3.6.1 Synthesis of Polymethines

The polymethines investigated in this chapter were synthesized by the collaborators from the Marder group at Georgia Institute of Technology. Metal coordinated DOB dyes were

synthesized by Dr. Hsien Chieh Lin; chalcogenopyrylium polymethines were result of the synthetic efforts by Dr. Yulia Getmaneko, and Dr. Yadong Zhang; TPPhPd substitutions were performed by Dr. Iryna Davidenko. The corresponding synthetic details are provided in the ESI of references [124] and [120].

3.6.2 Film Preparation

All films were cast using a Laurell Technologies WS-650-23 spin coater operated at 750 rpm for four minutes, followed by an overnight vacuum drying. The thin films for use in linear absorption measurements were cast from dye solutions, 0.4 wt% in DBM and 1.5 wt% in 1,1,2-trichloroethane onto microscope coverslips. Thicker films used for linear loss and nonlinear optical measurements were spun using more viscous solutions prepared by mixing an equal volume of 6 wt% dye solution and 6 wt% APC solution in 1,1,2-trichloroethane. All solutions were filtered through 0.2 μm PTFE syringe filters prior to spinning to remove dust and any undissolved particulates. The substrates for the thicker films were 0.5 mm thick fused silica, cut to ca. 1×4 cm in size to allow a sufficient length of light propagation for accurate loss measurements. The thicknesses of the films were determined using Dektak 6M profilometer; the thicknesses of the thinner films were ca. 80 nm and ca. 1.1-1.2 μm , respectively.

3.6.3 Characterization of linear absorption, refractive index and linear optical loss

Absorption spectra were recorded using a dual-beam Shimadzu UV-3101PC UV-VIS-NIR scanning spectrometer. For all spectroscopic measurements (both linear and

nonlinear) on solutions, spectrometric grade chloroform (Sigma-Aldrich) was used. Linear absorption measurements were performed on 6 μ M solution in 1cm pathlength cuvettes using 1 nm slit width. The absorption spectra of the thin films were taken with a microscope slide as the reference using 2 nm-wide slit.

The refractive indexes, thickness and optical loss of guest-host films were measured using a prism coupler (Metricon®, Model 2010) which was equipped with a 200-P-1 prism (code 995.4) and a scanning-fiber probe for optical loss measurement. The principle behind operation is summarized in Section 2.2.1. The light source used was a 1550nm CW diode laser operating at 4.2mW (Melles Griot, Diode Laser Driver 06DID203). The film thickness extracted from the prism coupling measurements agreed well with the values obtained using contact profilometry.

3.6.4 Nonlinear Optical Characterization Technique

Z-scan were performed at various excitation irradiances ranging from 30-270 GW/cm² in order to ensure that the extracted real and imaginary components of the third-order susceptibilities, $\chi^{(3)}$ s, are indeed purely from third-order contribution. The principle and standard layout is given in Section 2.2.2. The HW1/e² radius of the beam used for the experiment was ca. 60 μ m, its Rayleigh range was 4–5 mm, and the beam shape was found to be Gaussian with an M value of 1~1.08. The experimental setup was validated using well-established nonlinearities for samples of fused silica, ZnS, ZnSe, and GaAs. **(Table 2.1)** It should be noted that for the samples in solution, the 1 kHz pulse repetition rate has been found to obscure the closed aperture results due to thermal nonlinearities in some cases. In order to eliminate these effects, the repetition rate of the system was

reduced to 50 Hz. This lower repetition rate minimized the thermal contributions to the resulting closed-aperture signals. The resulting open- and closed-aperture scans were then corrected by subtracting their respective background contributions: the solvent, CHCl_3 , in the case of solution measurements; and the substrate, 500 μm thick fused silica, in the case of film measurements. For the remainder of this thesis, all Z-scans should be assumed to have been performed using these parameters unless otherwise noted.

3.7 References

28. Bredas, J.L., et al., *Third-Order Nonlinear Optical Response in Organic Materials: Theoretical and Experimental Aspects*. Chemical Reviews, 1994. **94**(1): p. 243-278.
52. Johr, T., et al., *Third-order nonlinear polarizabilities of a homologous series of symmetric cyanines*. Chemical physics letters, 1995. **246**(4): p. 521-526.
53. Marder, S.R., et al., *A unified description of linear and nonlinear polarization in organic polymethine dyes*. Science, 1994. **265**(5172): p. 632-635.
59. Fu, J., et al., *Molecular structure two-photon absorption property relations in polymethine dyes*. Journal of the Optical Society of America B, 2007. **24**(1): p. 56-66.
62. Hales, J.M., et al., *Design of polymethine dyes with large third-order optical nonlinearities and loss figures of merit*. Science, 2010. **327**(5972): p. 1485-1488.
78. Tolbert, L.M. and X. Zhao, *Beyond the cyanine limit: Peierls distortion and symmetry collapse in a polymethine dye*. Journal of the American Chemical Society, 1997. **119**(14): p. 3253-3258.
98. Halvorson, C., et al., *Third harmonic generation spectra of degenerate ground state derivatives of poly (1, 6-heptadiyne)*. Chemical physics letters, 1993. **212**(1): p. 85-89.
99. Krausz, F., E. Wintner, and G. Leising, *Optical third-harmonic generation in polyacetylene*. Physical Review B, 1989. **39**(6): p. 3701.
100. Hermann, J.-P., *Non-linear susceptibilities of cyanine dyes. Application to frequency tripling*. Optics Communications, 1974. **12**(1): p. 102-104.
101. Lepkowicz, R.S., et al., *Nature of the electronic transitions in thiocarbocyanines with a long polymethine chain*. Chemical physics, 2004. **305**(1): p. 259-270.
102. Stiel, H., S. Dähne, and K. Teuchner, *J-aggregates of pseudoisocyanine in solution: New data from nonlinear spectroscopy*. Journal of luminescence, 1988. **39**(6): p. 351-357.
103. Kobayashi, S., *Large optical nonlinearity in pseudoisocyanine J-aggregates*. Molecular Crystals and Liquid Crystals, 1992. **217**(1): p. 77-81.

104. Sasaki, F., S. Haraichi, and S. Kobayashi, *Linear and nonlinear optical properties of pseudoisocyanine J aggregates in distributed feedback microcavities*. Quantum Electronics, IEEE Journal of, 2002. **38**(7): p. 943-948.
105. Kumar, V., G.A. Baker, and S. Pandey, *Ionic liquid-controlled J- versus H-aggregation of cyanine dyes*. Chemical Communications, 2011. **47**(16): p. 4730-4732.
106. Matichak, J.D., et al., *Using End Groups to Tune the Linear and Nonlinear Optical Properties of Bis (dioxaborine)-Terminated Polymethine Dyes*. ChemPhysChem, 2010. **11**(1): p. 130-138.
107. Hales, J.M., et al., *Bisdioxaborine polymethines with large third-order nonlinearities for all-optical signal processing*. Journal of the American Chemical Society, 2006. **128**(35): p. 11362-11363.
108. Xia, H.P., R.C. Yeung, and G. Jia, *Synthesis of Symmetrical C5H5-Bridged Dimeric Ruthenium Complexes*. Organometallics, 1997. **16**(15): p. 3557-3560.
109. Spotts, J.M., W.P. Scafer, and S.R. Marder, *The synthesis and spectroscopic properties of organometallic cyanine analogues*. Advanced Materials, 1992. **4**(2): p. 100-102.
110. Halik, M. and H. Hartmann, *Synthesis and characterization of new long-wavelength-absorbing oxonol dyes from the 2, 2-difluoro-1, 3, 2-dioxaborine type*. CHEMISTRY-WEINHEIM-EUROPEAN JOURNAL-, 1999. **5**: p. 2511-2517.
111. Zyabrev, K., et al., *Design, Synthesis, and Spectral Luminescent Properties of a Novel Polycarbocyanine Series Based on the 2, 2-Difluoro-1, 3, 2-dioxaborine Nucleus*. European Journal of Organic Chemistry, 2008. **2008**(9): p. 1550-1558.
112. Gerasov, A., et al., *The nature of electron transitions in anionic dioxaborines, derivatives of aminocoumarin*. Journal of Physical Organic Chemistry, 2008. **21**(5): p. 419-425.
113. Kuhn, H., *A Quantum-Mechanical Theory of Light Absorption of Organic Dyes and Similar Compounds*. The Journal of Chemical Physics, 1949. **17**(12): p. 1198-1212.
114. Marder, S.R., et al., *Large molecular third-order optical nonlinearities in polarized carotenoids*. Science, 1997. **276**(5316): p. 1233-1236.

115. May, J.C., et al., *Highly efficient third-order optical nonlinearities in donor-substituted cyanoethynylethene molecules*. Optics letters, 2005. **30**(22): p. 3057-3059.
116. Scarpaci, A., et al., *Effects of dendronization on the linear and third-order nonlinear optical properties of bis (thiopyrylium) polymethine dyes in solution and the solid state*. Chemistry of Materials, 2012. **24**(9): p. 1606-1618.
117. Würthner, F., T.E. Kaiser, and C.R. Saha-Möller, *J-Aggregates: From Serendipitous Discovery to Supramolecular Engineering of Functional Dye Materials*. Angewandte Chemie International Edition, 2011. **50**(15): p. 3376-3410.
118. West, W. and S. Pearce, *The dimeric state of cyanine dyes*. The Journal of Physical Chemistry, 1965. **69**(6): p. 1894-1903.
119. Tolmachev, A., M. Kudinova, and N. Derevyanko, *Pyrylocyanines*. Chemistry of Heterocyclic Compounds, 1974. **10**(1): p. 45-49.
120. Barlow, S., et al., *Polymethine materials with solid-state third-order optical susceptibilities suitable for all-optical signal-processing applications*. Materials Horizons, 2014. **1**(6): p. 577-581.
121. Chi, S.H., et al., *Thick Optical-Quality Films of Substituted Polyacetylenes with Large, Ultrafast Third-Order Nonlinearities and Application to Image Correlation*. Advanced Materials, 2008. **20**(17): p. 3199-3203.
122. Li, Z.a., et al., *High-Optical-Quality Blends of Anionic Polymethine Salts and Polycarbonate with Enhanced Third-Order Non-linearities for Silicon-Organic Hybrid Devices*. Advanced Materials, 2012. **24**(44): p. OP326-OP330.
123. Esembeson, B., et al., *A High-Optical Quality Supramolecular Assembly for Third-Order Integrated Nonlinear Optics*. Advanced Materials, 2008. **20**(23): p. 4584-4587.
124. Lin, H.-C., et al., *Synthesis and linear and nonlinear optical properties of metal-terminated bis(dioxaborine) polymethines*. Chemical Communications, 2011. **47**(2): p. 782-784.

CHAPTER 4

ANIONIC POLYMETHINES WITH VARYING COUNTERIONS FOR ENHANCED COMPATIBILITY WITH HOST POLYMER

4.1 Introduction

For practical AOSP applications, it is imperative for the polymethine molecules to be processed into good optical quality thin films with high chromophore loading densities. Polymethines are highly polarizable ions, thus prone to both strong inter- and/or intra-molecular interactions in the solid-state via aggregation, and ion pairing,[125] respectively. These interactions can lead to undesirable distortion of the molecular symmetry and charge localization, leading to dramatically reduced $\chi^{(3)}$ values. In addition, the concomitant shifts and broadening of both linear and two-photon absorption bands can ruin the advantageous optical transparency window mentioned in the previous chapters. Therefore, understanding the effects of counterion on the optical properties of cyanines at a high number density environment is critical in overcoming challenges associated with translating the favorable molecular figures-of-merit of cyanines into material FOMs.

Recently, anionic polymethines based on the substitution of strongly electron withdrawing tricyanofuran^{xviii} (TCF) groups at terminal positions with strongly red-shifted photophysical properties have been reported. These TCF-terminated cyanines are unique in that, unlike common cationic cyanines whose conformation is predominantly limited to *syn*- type, they are readily observable in three different conformers (**Figure 4.1**) with near-identical delocalization lengths at room temperature. This enables these chromophores to exhibit increased solubility compared to the cationic counterparts, and a distinct ability to form linear chains when bridged by small cationic counterions. [126]

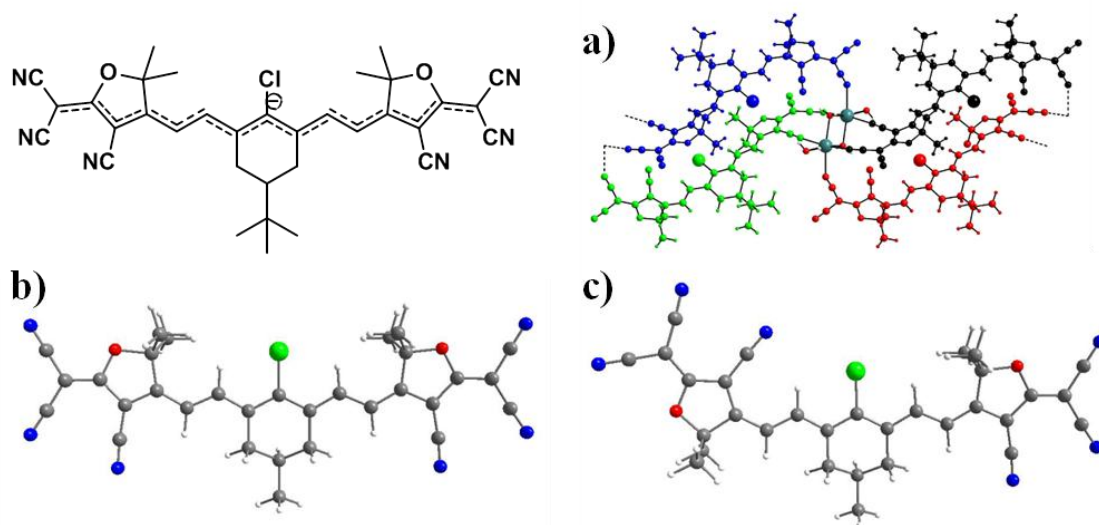


Figure 4.1. Chemical and DFT optimized structure of tricyanofuran-terminated heptamethines: a) crystal packing in presence of a small dimeric cation (Na^+ shown) b) *syn*- conformer c) *anti*- conformer. DFT structures reprinted with permission from the authors [126] (Copyright © 2008 American Chemical Society *Org. Lett.*)

^{xviii} IUPAC name: 4,5,5-trimethyl-3-cyano-2(5H)-furanilydenepropane-dinitrile

In this chapter, we report on the systematic modification of the counterions of TCF-polymethines and the impact that these different counterion have on their linear and NLO properties of TCF-polymethines in both the solution and films. For solid-state material characterization, we have employed a polymer guest-host approach using amorphous polycarbonate (APC), a highly processable polymer which a sizable refractive index ($n_0 \approx 1.559$) and negligible nonlinearity at $1.55 \mu\text{m}$, in order to mitigate the potential absorptive loss at high number density.

4.2 Effects of Various Counterions on the Optical properties of TCF-terminated heptamethine – Amorphous Polycarbonate (APC) blend films

One approach to improve the miscibility of TCF polymethine salt and the host polymer is to modify the structure of the counterions so as to increase the attractive intermolecular interaction with the polymer. Specifically, we reasoned that aryl-based cationic counterions with a large delocalized positive charge would reduce the strength of the electrostatic TCF polymethine-counterion interaction, and reduce the ion-pairing energy.[125] Additionally, a moderately polar counterion might improve the solvation of the cations via attractive dipole-dipole interactions with the carbonate groups of the polymer. To test the validity of this hypothesis, a series of aromatic counterions such as benzyl-triethyl ammonium chloride, benzyl-triphenyl phosphonium bromide, pentafluorobenzyl-triphenyl phosphonium bromide and (4-diethylaminobenzyl)-triphenyl phosphonium iodine, were paired with TCF polymethines in the preparation of salts whose structures are given below (**Figure 4.2**). These polymethine-cation pairs have been

prepared through ion exchange reactions by Zhong'an Li from the Jen group at the University of Washington.

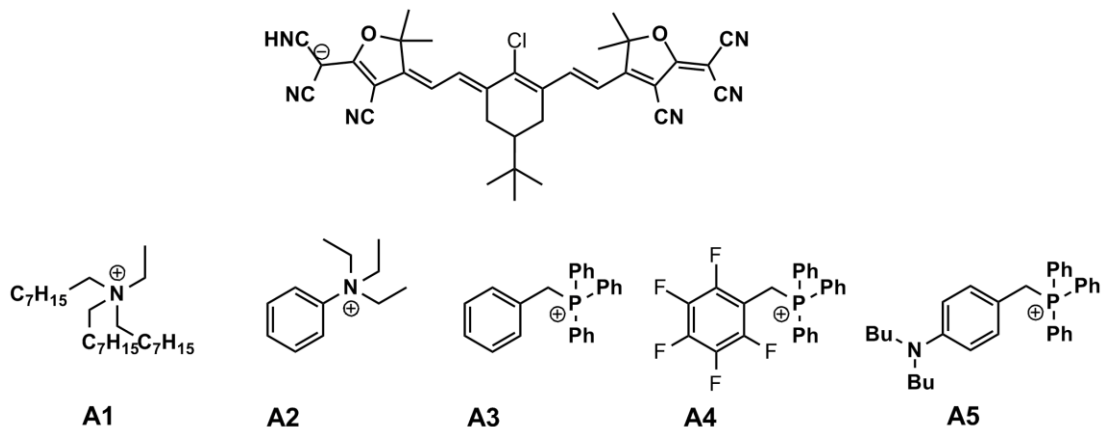


Figure 4.2. Structures of various counterions paired with TCF-terminated heptamethines

4.2.1 Linear Optical Properties

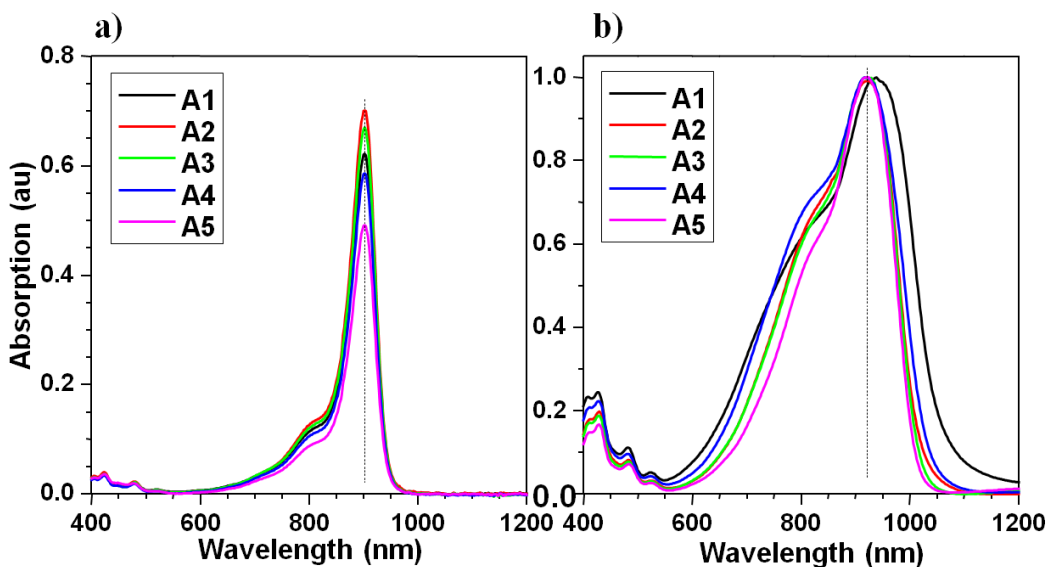


Figure 4.3. The absorption spectra of polymethines in (a) dilute DCM solutions (concentration of $\sim 2 \times 10^{-6}$ M) and (b) thin guest-host APC films doped with 50 wt% of chromophores

Figure 4.3 a) shows the 1PA spectra for some of the dyes in dilute solutions and in films at 50 wt% in an amorphous polycarbonate (APC) host. The spectra show characteristic features of long-chain polymethines: sharp bands in the near-IR with very large extinction coefficients. The different counterions seem to have minimal influence on the $\pi \rightarrow \pi^*$ electronic transitions in DCM. The film absorption spectra in **Figure 4.3 b)** exhibit qualitatively similar features to their solution spectra, albeit with increased band broadening, which suggest inhomogeneous broadening, aggregation or charge localization in the ground-state geometry. In particular, the polymethine salt with the aliphatic cation, **A1** suffer greater bandwidth broadening compared to the other four with aromatic cations. The film absorption spectrum of **A5** exhibits the narrowest linewidth, a result consistent with the hypothesis of enhanced solubility of polymethines with bulky, polarizable aromatic counterions bearing a moderately polar group in APC.

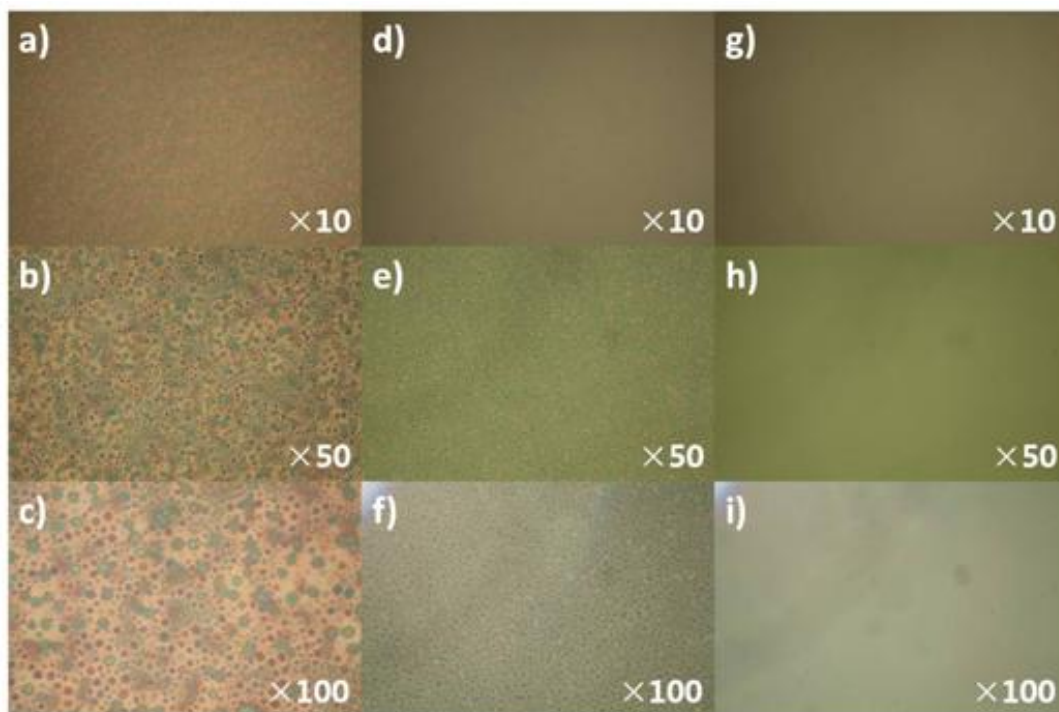


Figure 4.4. Optical transmission micrographs of thick guest-host APC films doped with 50 wt% of polymethine salt under different magnifications. a), b), c) APC film containing **A1** under $\times 10$, $\times 50$, and $\times 100$ magnification, respectively. d), e), f): **A2**, and g), h), i): **A5**

Thicker films ($\approx 2\mu\text{m}$) of the guest-host polymers were prepared for morphological studies and characterization of bulk linear and NLO properties. The transmission optical microscopy images of these thick films under the different magnifications are shown in **Figure 4.4**. Under the $10\times$ magnification, the A2 and A5 films are noticeably more homogenous than that of A1, which exhibits clear evidence of phase separation. At $50\times$ magnification, evidence of phase separation can also be observed for the A2 film, while A5 film remains optically homogeneous even at a magnification of $100\times$. These results seem to support well the hypothesis that moderately polar, aromatic counterions with diffuse charge localization can be used to enhance the compatibility between polymethine salt guests and the APC host polymer.

Table 4.1. The linear and nonlinear optical properties at 1.55 μm of thick guest-host APC films doped with 50 wt.% polymethine salt

Dye	Index ^a	Loss ^b (dB/cm)	$ \chi^{(3)} ^c$ ($\times 10^{11}$ esu)	$ \text{Re } \chi^{(3)} / \text{Im } \chi^{(3)} ^d$
A2 (50%)	1.79	NA	4.5	3.4
A3 (50%)	1.79	9.0	3.8	2.7
A4 (50%)	1.76	NA	4.5	3.1
A5 (50%)	1.76	7.5	4.0	2.7
A3(25%)	1.72	5.8	2.7	3.9
A5(25%)	1.69	5.0	2.1	2.7

^a Refractive indexes measured by prism coupling; ^b the linear optical loss measurements. NA: not available due to loss exceeding the detection limit; ^c $|\chi^{(3)}| = [(\text{Re } \chi^{(3)})^2 + (\text{Im } \chi^{(3)})^2]^{1/2}$; ^d the errors were estimated to be $\pm 14\%$

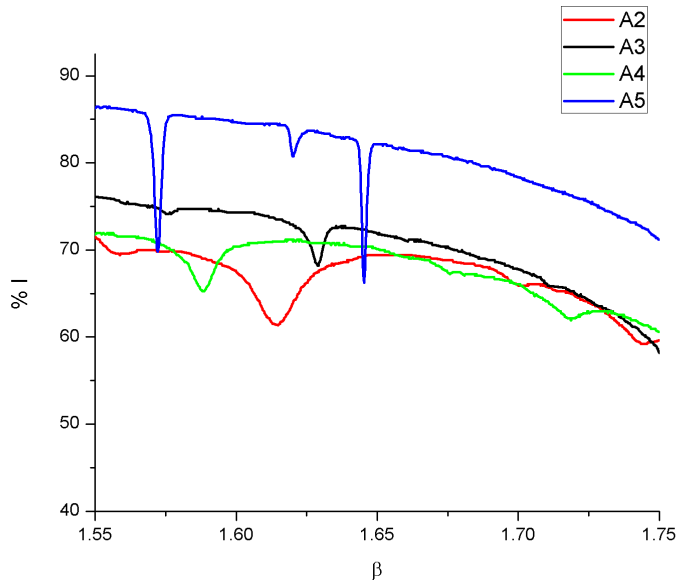


Figure 4.5. Prism coupling intensity plots for thick ($\sim 1.5 \mu\text{m}$) guest-host APC films doped with 50 wt.% polymethine salts

The refractive indexes and the linear optical losses of the films at 1550nm were measured by the prism coupling method and the results are summarized in **Table 4.1**. The linear losses of the **A2** and **A4** films exceeded the detection limit of 20 dB/cm, while the mode-coupling profiles were found to be excessively broad. (**Figure 4.5**) The large linear losses may be due to the weak polarity and polarizability of the counterion in **A2**, and to the steric bulk of the fluorine substituents of the counter ion in **A4**, each adversely affecting solvation in polycarbonate host. In addition, the inductive effect of the fluorine substituent at the 4' position of the pentafluorobenzyl phosphonium most likely results in a weaker the ground-state polarity and polarizability compared to **A3** and **A5**, further reducing its solubility in APC. On the other hand, the films containing **A3** and **A5** showed significantly lower losses of 9 dB/cm and 7.5 dB/cm, respectively, with reasonably narrow mode-coupling profiles. (**Figure 4.5**) The reduced loss for **A3** and **A5** correlates with the optical quality observed for these films under optical microscopy.

4.2.2 Nonlinear Optical Properties

Table 4.2. Molecular nonlinearities of 6.0~6.5 mM **A2-A5** in DCM at 1550 nm

Dye	Re(γ)	Im(γ)	$ \gamma $	$ \text{Re}(\gamma)/\text{Im}(\gamma) $	Calc. $ \chi^{(3)} ^a$
	(10^{-32} esu)	(10^{-32} esu)	(10^{-32} esu)		(10^{-11} esu)
A2	-2.8	1.2	3.0	2.3	9.1
A3	-2.8	1.3	3.1	2.2	8.2
A4	-2.3	1.3	2.6	1.8	7.4
A5	-3.3	1.4	3.6	2.4	7.5

$a |\chi^{(3)}| = NL^4 |\gamma|$. The local field factor was assumed to be dominated by the solvent, DCM, thus the static refractive index, n_0 , used in calculation was DCM 1.42.

Third-order macroscopic non-linearities of the solution and film composites containing **A2-A5** were measured at 1550nm using fs- pulsed Z-scan, and the results are summarized in Table 4.1 and Table 4.2. By employing a linear number density extrapolation to predict material nonlinearity, $\chi^{(3)}$, from molecular polarizability, γ , it was found that the calculated $|\chi^{(3)}|$ are in reasonable agreement with the values determined from the blended films, suggesting that the chromophores can retain their polymethine-like characteristics after being processed into high number density films. This is encouraging particularly given the deleterious impacts that aggregation can have on the NLO response of polymethines in solid state. As a result, these polymethine/APC blend films exhibit large third-order susceptibilities that exceed those of organic materials previously used in SOH devices, and are approximately three times larger than the value of crystalline silicon.[13-15] It should be noted that the film containing **A2** showed spot-to-spot variations in the

measured $|\chi^{(3)}|$ values indicating spatial inhomogeneity, likely a result of the aforementioned phase-separation of the film.

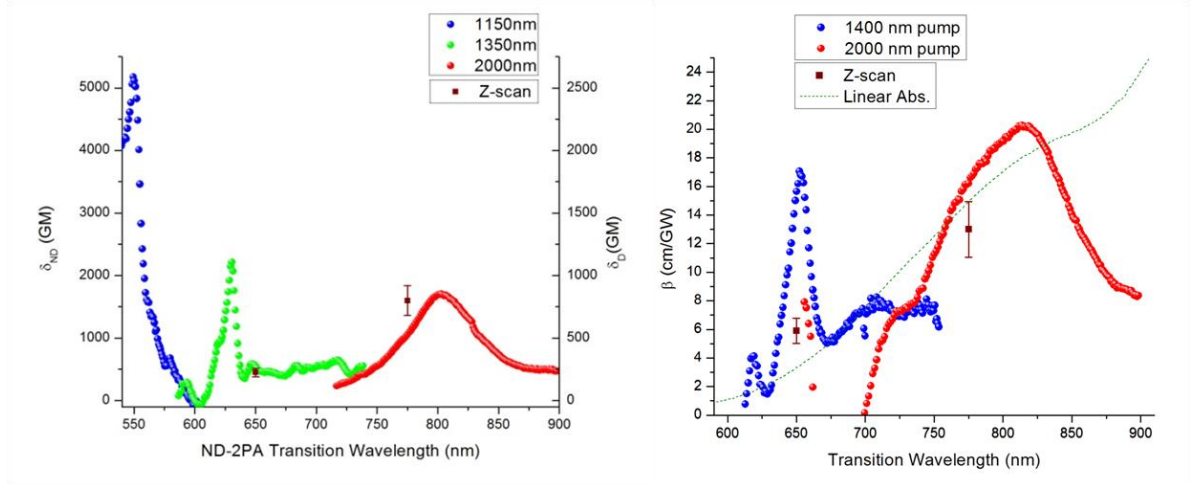


Figure 4.6. Left: non-degenerate two-photon absorption (ND-2PA) spectra[96] of 5.4mM **A3** in chloroform overlaid with the degenerate TPA cross-sections, δ_D , ($1 \text{ GM} = 10^{-50} \text{ cm}^4 \text{ s photon}^{-1}$) obtained from Z-scan. Right: 50 wt. % **A3**: APC film overlaid with TPA coefficients, β . The dashed line represents linear absorption.

The macroscopic two-photon FOMs for these polymethine blend films are not sufficiently large for phased-based all-optical switching applications. In order to understand the origins of the reduced FOMs, non-degenerate two-photon absorption spectroscopy was performed. As seen from **Figure 4.6**, the the lowest-lying TPA bands centered at 810nm which correspond to vibronically allowed resonances[59] are in close proximity to the double the energy of the excitation frequency of $1.55\mu\text{m}$. This would lead to the large $\text{Im}(\chi^{(3)})$ seen and subsequently the large $|\text{Re}(\chi^{(3)}) / \text{Im}(\chi^{(3)})|$ ratios. In fact, these $\text{Im}(\chi^{(3)})$ values correspond to two-photon absorption coefficient β of $1.3 \times 10^{-10} \text{ m/W}$, which exceed that of gallium arsenide, a semiconductor known to have a large two-photon absorption across the telecommunication region. The ND-2PA spectrum of the

solution shows that the optical transparency window lies between 600 nm and 750nm. The sharp band at 650nm is associated with stimulated Raman response arising from the difference in the pump and probe wavelengths corresponding to stoke shift.

4.2.3 SOH application

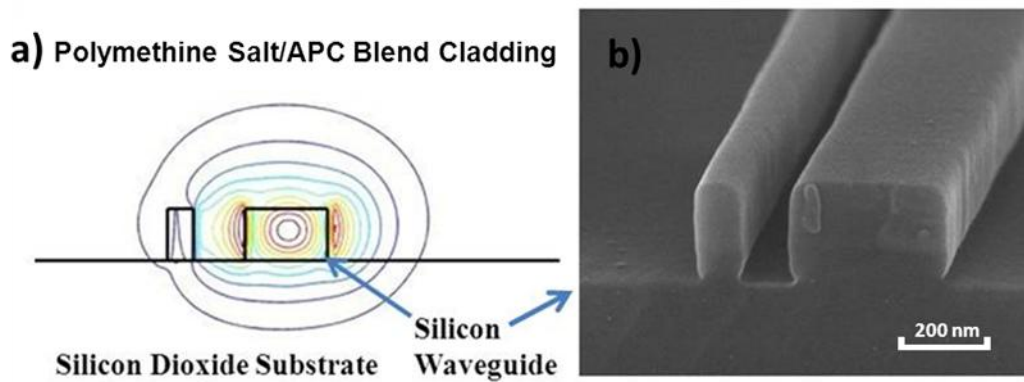


Figure 4.7 a) Calculated optical mode pattern for TE₀ mode of the asymmetric slot waveguide. b) SEM micrograph of the cross-section showing 100 and 310 nm width silicon rails with 180 nm slot

Despite sub-optimal FOMs for nonlinear index-based switching, the large values of $|\chi^{(3)}|$ and β , and also the processability imparted through the use of polymer guest-host blends allowed for the claddings to be applied via facile spin-casting method, enabling for other AOSP applications such as four-wave mixing (FWM) [127-129] and loss-based all-optical switching.[130, 131] As shown on **Figure 4.7**, the TCF-polymethines/APC blend films were applied as claddings on top of asymmetric slot Si waveguides to create SOH device.[132] Using this device, the collaborators at the Hochberg group successfully demonstrated wavelength conversion under near-degenerate FWM

conditions with the pump pulse centered at 1548 nm, probe at 1550 nm, and the sideband generated at 1546 nm. (**Figure 4.8**) They also confirmed that the $|\chi^{(3)}|$ s of the 25 wt. % guest-host blends (**Table 4.2**) are in a good agreement with the values predicted from free-space Z-scan, with the $|\chi^{(3)}|$ of 2.0×10^{-11} esu and TPA coefficient β of 6.5×10^{-11} m/W.

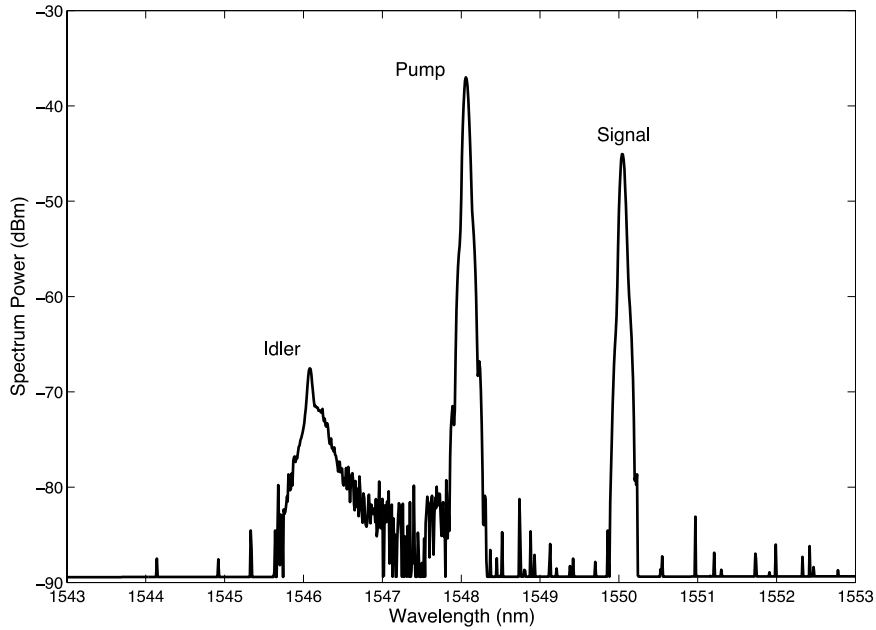


Figure 4.8. Optical spectrum showing idler wavelength generated by near-degenerate four wave mixing in silicon organic hybrid slotted waveguide device coated with 25 wt.% **A3** in amorphous polycarbonate. Down-converted light was filtered out by the measurement system.

4.3 Effects of Multiply-charged Counterions on Optical Properties of TCF-terminated Polymethines

Compared to the TCF-polymethine systems with singly-charged counterions investigated in the previous section,[122] multiply-charged counterions can potentially form a

supramolecular salt complex with the chromophores potentially constraining them in close proximity to one another in a particular geometry. Such constraint could impact both intra- and inter-molecular interactions. By controlling the nature of the counterions, a particular interaction can be favored, such as induced dipole – induced dipole interactions predicted between the cyanines, or the electrostatic interactions between cyanine and its counterion. We predict that, with judicious choices of counterions, these constructs could create a high dielectric screening media that inhibit intermolecular interactions between the molecular pairs, and result in materials with optical properties that are only dependent on local environment, and independent of the overall molecular concentrations.

The relative spatial locations and the nature of counterions of polymethines have been shown to affect significantly the geometric and electronic structures of polymethines, as well as their linear and NLO properties.[125, 133] Dahne et al. have reported that distortions of polymethines electronic structures in crystals are predominantly driven by coulombic interactions between cationic polymethines and anionic counterions.[134] Quantum chemical characterization of such polymethines–counterion complexes has revealed significant alterations in the mean BLA, and subsequent NLO properties due to the electrostatic interactions between the ions.[60, 135] Thus, in this section, the impacts of these multi-chromophore – counterion pairs will be determined by probing both their linear and NLO properties over a range of concentrations.

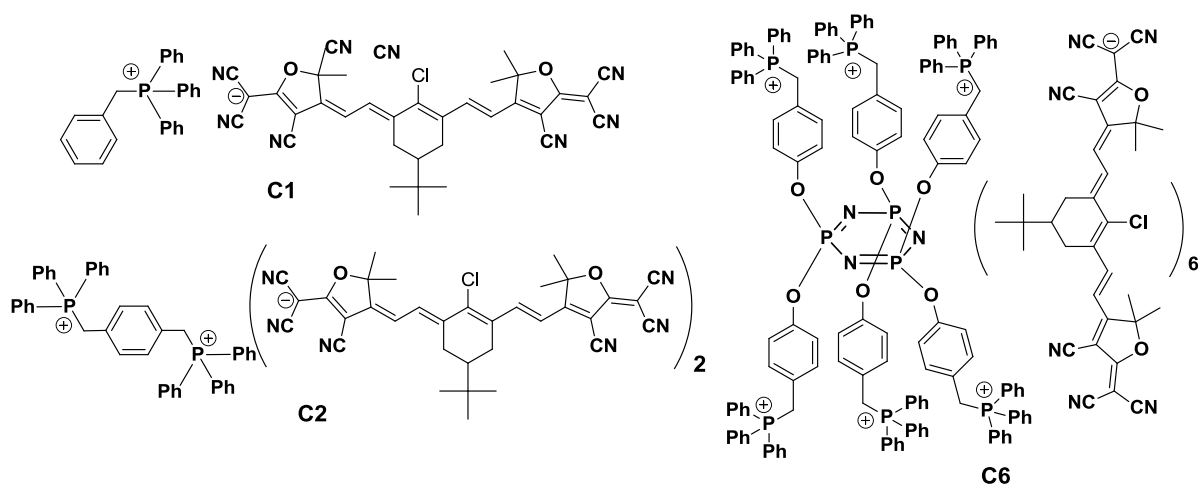


Figure 4.9. Structures of TCF-polymethines and the counterions

The molecular structures of the polymethines salts studied in this section are summarized in **Figure 4.9**. In this scheme, di-cationic 1,4-*Bis*[(triphenylphosphonium)methyl]benzene and hexa-cationic hexakis[(4-oxybenzyl)triphenylphosphonium]cyclotriphosphazene were designed first to pairs with multiple anionic TCF-polymethines to produce two new supramolecular polymethines salt complexes **C2** and **C6** respectively, while **C1** with a mono-cationic counterion was prepared according to the previously reported method.[122] The planarity of the benzene ring coupled with the *para*- substitution of the phosphoniums in **C2** may help minimize aggregation between the chromophores, however, the potential head-to-tail chromophore-counterion alignment may give rise to electrostatic interactions. Similarly, since the ring of cyclotriphosphazene in the hexa-cation is almost planar, the phosphonium salt substituents are likely spatially dispersed symmetrically around the ring due to repulsive interaction between the cations. This may facilitate an interdigitation of the chromophores around the counterions.

4.3.1 Linear optical properties of TCF-heptamethine /Multication Counterion Pairs

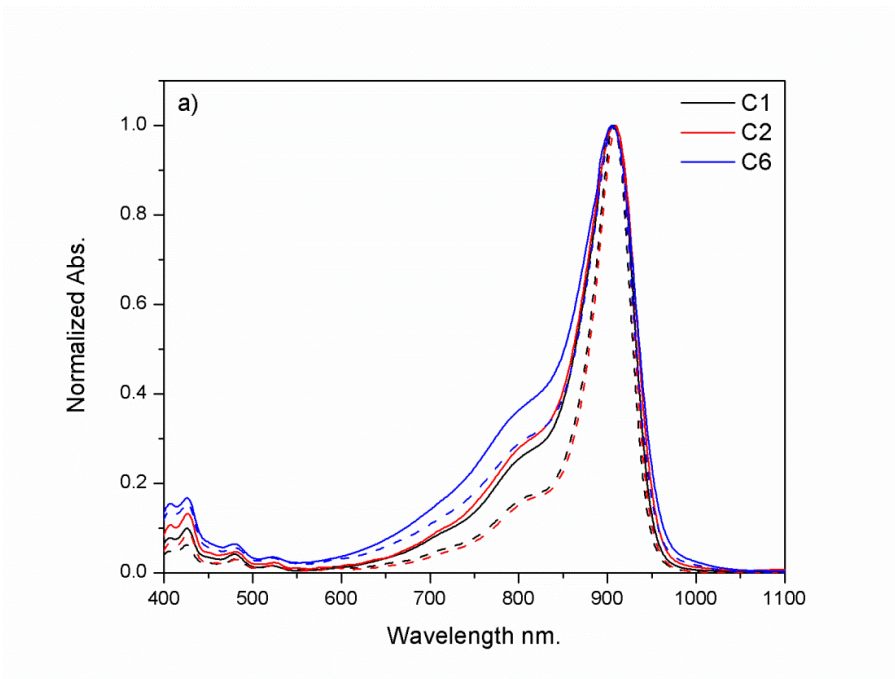


Figure 4.10. Normalized Vis-NIR spectra of dyes in CHCl_3 (dash: $12\mu\text{M}$, solid: 5mM)

The linear optical properties of these polymethines salts in both solutions and solid-state were investigated in order to elucidate the effects of the counterions various concentrations on the electronic transitions. The normalized UV-Vis-NIR absorption spectra of the molecules in chloroform solutions are shown in **Figure 4.10**, and a summary of their optical properties on a per-chromophore basis is given in **Table 4.3**. All three molecules show the characteristic features of highly polarizable and symmetric polymethines with sharp transitions (centered at $\lambda_{\text{max}} = 906\text{nm}$) possessing very large extinction coefficients and containing weak vibronic shoulders. The different counterions seem to have minimal influence on the $\pi \rightarrow \pi^*$ electronic transitions as evidenced by the similarity in the location and bandwidth of their (0,0)- absorption bands.

At dilute concentrations, **C6** shows a higher relative intensity of the vibronic shoulder (ca. 780 nm) than **C1** or **C2**, indicating a more significant change in geometry upon excitation. At higher concentration, **C1** and **C2** show a significant increase in the relative contribution of their vibronic shoulders, while such increase in the magnitude is much less pronounced for **C6**. Hence, **C1** and **C2** seem to be more sensitive to the changes to overall molecular concentrations.

Table 4.3 Comparison of relative oscillator strengths (f) and extinction coefficients per chromophore of **C1**, **C2**, and **C6** at dilute and concentrated solutions

	Dilute			Concentrated		
	$f/f_{\text{dil. C1}}$	$\epsilon_{\text{max}}^a (\times 10^5 \text{ M}^{-1} \text{ cm}^{-1})$	μ_{ge}^b (D)	$f/f_{\text{dil. C1}}$	$\epsilon_{\text{max}} (\times 10^5 \text{ M}^{-1} \text{ cm}^{-1})$	M_{ge} (D)
C1	1	3.25	17.0	0.88	1.97	16.0
C2	0.84	2.80	15.6	0.72	1.62	14.4
C3	0.54	1.28	12.8	0.52	0.97	12.3

^a Measured in CH_2Cl_2 ^b Obtained from main absorption band using $\mu_{\text{ge}} = 0.09854 [\int (\epsilon/\nu) d\nu]^{0.5}$ where ϵ is in $\text{M}^{-1} \text{ cm}^{-1}$, ν in cm^{-1} , and the transition moments are expressed in Debye (D)

A closer analysis of the linear optical properties at dilute concentrations shows that the individual chromophores in the **C2** and **C6** multi-cationic constructs exhibit reduced extinction coefficients ϵ , oscillator strengths $f/f_{\text{dil. C1}}$, and ground to lowest-lying excited state transition dipole moments M_{ge} , compared to those of **C1**. (**Table 4.3**) This points to stronger intra-molecular interactions in the multi-cationic construct resulting in charge

localization; however, the question remains whether the perturbation arises from counterion–chromophore or chromophore–chromophore interactions.

Table 4.3 also reveals that the relative oscillator strengths and transition dipole moments of **C1** and **C2** at high concentrations are noticeably dampened than those at dilute concentrations, suggesting that electronic configurations of **C1** and **C2** are also strongly affected by overall concentrations. **C6** on the other hand, shows minimal change in this regard, remaining somewhat impervious to the increase in the molecular concentration. Strong intra-molecular ion- pairing interactions in **C6** may be constraining the orientation of the chromophores within the construct which in turn, may help shield these chromophores from interacting with the chromophores or counterions of neighboring salt complexes.

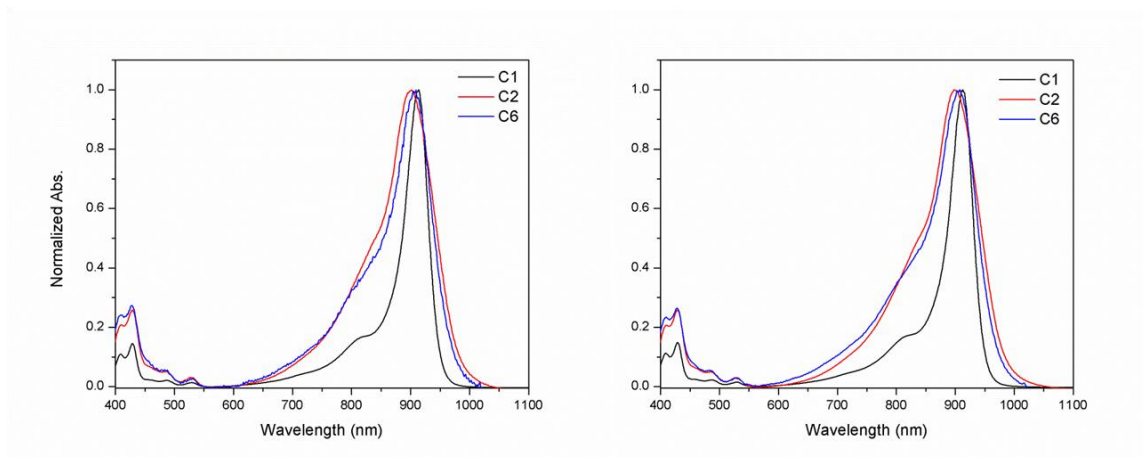


Figure 4.11. Normalized Vis-NIR spectra of **C1**, **C2**, and **C6** in toluene. Left: 5 μM , right: 20 μM

The insensitivity of the spectral properties over a range of lower concentrations suggests that aggregation (i.e. chromophore-chromophore interactions) plays a negligible role. On

the other hand, the absorption spectra of **C2** and **C6** in toluene – a solvent more likely to induce a stronger ion pair association due to reduced polarity and polarizability[125] – exhibit features that deviate significantly from those of ideal polymethines marked by a noticeable broadening and loss of vibronic shoulder. This combination of results indicates that the main sources of perturbation that causes charge localization is most likely chromophore–counterion interactions. Interestingly, the spectrum of **C1** in toluene remains relatively unchanged compared to chloroform which is consistent with the mitigating effects of a bulky polarizable counterion discussed in Section 4.2.

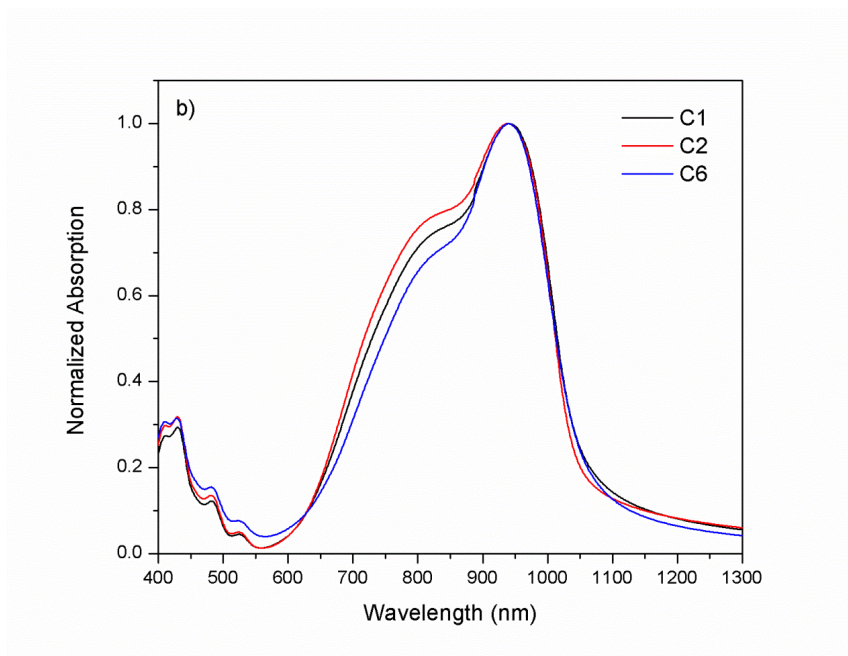


Figure 4.12. Normalized UV-Vis-NIR spectra of **C1**, **C2**, and **C6** in neat films (80 nm thick)

To investigate the effect of multi-cationic counterions on the optical properties of solid-state materials, neat films of these complexes were prepared by spin-coating the salt solutions onto pretreated glass substrates. The absorptions spectra of these films are

shown in **Figure 4.12**. Most of the film spectra exhibit significantly broadened absorption bands, along with a 30nm red-shift in their absorption maxima, more intense vibronic transitions, typically associated with larger geometry changes upon excitation. This suggests the presence of charge localization in the salt complexes in solid-state, which is not surprising given the nearly three-orders of magnitude increase in molecular concentration beyond the concentrated solutions described above. Compared to the films of **C1** and **C2**, **C6** shows a reduced vibronic shoulder, more closely resembling its solution spectrum. Consistent with the results seen in the solution studies, these results indicate that use of multiply-charged counterions could provide a pathway for suppressing inter-chromophore interaction, and a method to create a highly dielectric shielding environment for the chromophores.

4.3.2 Monlecular Nonlinearities of TCF-heptamethine /Multication Counterion Pairs

Table 4.4. The molecular third-order polarizabilities of dyes measured in diluted and concentrated CHCl₃ solutions using the femtosecond pulsed Z-scan method at 1.3 μm.

Dye/Concentration ^a		Re(γ)	Im(γ)	Re(γ)/Im(γ) ^a	Calc.Re(γ)
		(10 ⁻³² esu ^a)	(10 ⁻³³ esu ^a)		(10 ⁻³² esu)
C1	0.5mM	-3.4	1.6	21	-3.4
	5.0 mM	-1.3	1.5	7.8	-2.8
C2	0.5mM	-3.1	1.6	18	-2.6
	5.0mM	-1.2	1.5	7.1	-1.5
C6	0.5mM	-2.6	2.1	13	-0.95
	5.0 mM	-0.88	1.7	5.1	-0.81

^a The concentrations and the values are represented in per chromophore in the salt complexes. Errors were estimated to be ±8% for Re(γ) and 11% for |Re(γ)/Im(γ)|.

Table 4.5 The molecular third-order polarizabilities of dyes measured in diluted and concentrated CHCl₃ solutions using the femtosecond pulsed Z-scan method at 1.55 μm.

Dye/ concentration ^a		Re(γ)	Im(γ)	Re(γ)/Im(γ)	Calc.Re(γ)
		(10 ⁻³² esu)	(10 ⁻³³ esu)		(10 ⁻³² esu)
C1	0.5mM	-3.4	9.0	3.8	-1.4
	5.0 mM	-1.6	9.7	1.6	-1.0
C2	0.5mM	-2.8	6.6	4.2	-1.0
	5.0mM	-1.2	7.5	1.6	-0.67
C6	0.5mM	-2.4	5.7	4.2	-0.42
	5.0 mM	-1.0	6.0	1.7	-0.32

^a The concentrations and the values are represented in per chromophore in the salt complexes. Errors were estimated to be ±8% for Re(γ) and 11% for |Re(γ)/Im(γ)|.

The real and imaginary components of γ , $\text{Re}(\gamma)$ and $\text{Im}(\gamma)$, of the salt complexes were determined from the dye solutions in chloroform using the Z-scan at 1.3 and 1.55 μm . The results are summarized in **Table 4.4** and **Table 4.5** along with $\text{Re}(\gamma)$ calculated from a simplified Sum-Over-States (SOS) expression for the nonlinear polarizability using experimentally determined values of M_{ge} from **Table 4.3**.^{xix} All of the salts in relatively dilute solutions (0.5mM chromophore) exhibit NLO properties typical for long-chain polymethines. Near the two-photon transparency window of 1.3 μm , [54]we observe large negative magnitudes of $\text{Re}(\gamma)$ with relatively small values of $\text{Im}(\gamma)$, resulting in high $|\text{Re}(\gamma)/\text{Im}(\gamma)|$ ratios of >12 .

Compared to **C1** and **C2**, 0.5mM **C6** shows a reduced $\text{Re}(\gamma)$ and increased $\text{Im}(\gamma)$, consistent with the results from the linear absorption studies that suggest ion-pairing interactions even at a relatively dilute concentrations. The trends in the calculated $\text{Re}(\gamma)$ values are nearly quantitative at 1.3 μm when compared to the experimental data, with the exception of **C6**. The larger experimental value for **C6** could be a byproduct of the increased two-photon activity – as evidenced by the larger $\text{Im}(\gamma)$ values – which would lead to a dispersion enhancement in $\text{Re}(\gamma)$ that is not accounted for in the simplified SOS expression. (**Figure 4.13**)

When the concentration of the solution is increased ten-fold to 5 mM, the enhanced intermolecular interactions lead to a significant decrease in $\text{Re}(\gamma)$ values for all three salts while the $\text{Im}(\gamma)$ shows little change. The experimental values of $\text{Re}(\gamma)$ for the concentrated solutions of **C1** and **C2** are smaller than predicted by the simplified two-state model. This supports the argument that, at higher concentrations, significant charge

^{xix} See Appendix

localizations and the concomitant increase in BLA occur in **C1** and **C2**. **C6** on the other hand, shows a much better agreement between the experimental and calculated $\text{Re}(\gamma)$, suggesting that ion-pairing has already occurred at a lower concentration and the value of M_{ge} has properly accounted for this effect.

The experimental values of $\text{Re}(\gamma)$ at 1.55 μm show the same trend of decreasing $\text{Re}(\gamma)$ across **C1**, **C2**, and **C6** with increasing concentrations. While the same trends are reproduced in the calculated $\text{Re}(\gamma)$ values, there is a significant deviation compared to the experimental values, as simplified theory underestimates the γ in all cases. This is most likely due to the same dispersion enhancement seen in dilute **C6** solution, owing to the proximity of the excitation wavelength to the vibronically allowed TPA band. At 1.55 μm all three dyes show significant TPA, as evidenced by the two-photon spectra provided below.

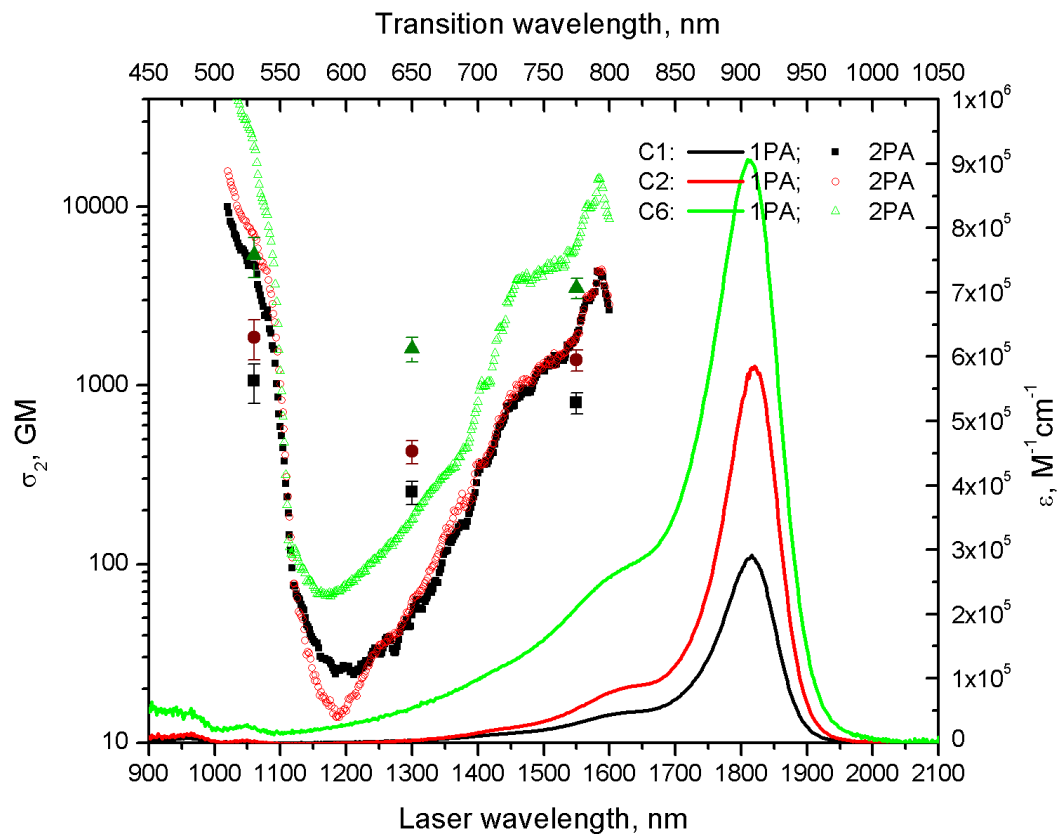


Figure 4.13. Overlay of linear absorption and two-photon absorption spectra **C1**, **C2**, and **C6**, obtained using two-photon induced fluorescence and Z-scan on 5mM (per molecule basis) solutions in chloroform.

4.3.3 Macroscopic Nonlinearities of TCF-heptamethine /Multication Counterion Pairs

Table 4.6 The molecular third-order polarizabilities of dyes measured in diluted and concentrated CHCl₃ solutions using the femtosecond pulsed Z-scan method at 1.3 μm.

Dyes	Re $\chi^{(3)a}$ ($\times 10^{-11}$ esu)	Im $\chi^{(3)a}$ ($\times 10^{-11}$ esu)	Re $\chi^{(3)}$ / Im $\chi^{(3)}$	Calc. Re $\chi^{(3)b}$ ($\times 10^{-11}$ esu)	Calc. Re $\chi^{(3)b}$ ($\times 10^{-11}$ esu)
C1	-3.3	0.43	7.8	-4.6	0.59
C2	-3.6	0.53	6.9	-4.7	0.67
C6	-3.8	0.74	5.2	-4.5	0.89

^a Errors from the measured values were estimated to be $\pm 13\%$ for Re(γ) and 18% for |Re(γ)/Im(γ)|. $|\chi^{(3)}|=NL^4|\gamma|$. The local field factor was calculated using the film refractive indexes of 1.61, 1.64, and 1.72 for C1, C2, and C6, respectively.

Table 4.7 The molecular third-order polarizabilities of dyes measured in diluted and concentrated CHCl₃ solutions using the femtosecond pulsed Z-scan method at 1.55 μm.

Dyes	Re $\chi^{(3)a}$ ($\times 10^{-11}$ esu)	Im $\chi^{(3)a}$ ($\times 10^{-11}$ esu)	Re $\chi^{(3)}$ / Im $\chi^{(3)}$	Calc. Re $\chi^{(3)b}$ ($\times 10^{-11}$ esu)	Calc. Re $\chi^{(3)b}$ ($\times 10^{-11}$ esu)
C1	-2.3	1.5	1.4	-6.2	3.7
C2	-3.4	1.9	1.8	-5.2	3.3
C6	-3.6	1.9	1.8	-5.1	3.1

^a Errors from the measured values were estimated to be $\pm 13\%$ for Re(γ) and 18% for |Re(γ)/Im(γ)|. $|\chi^{(3)}|=NL^4|\gamma|$. The local field factor was calculated using the film refractive indexes of 1.61, 1.64, and 1.72 for C1, C2, and C6, respectively.

The macroscopic third-order nonlinearities of neat films (thickness 1.2-1.6μm) at two different wavelengths, 1.3 and 1.55 μm, are summarized in **Table 4.6** and **4.7**,

respectively. The extrapolated $\chi^{(3)}$ values were calculated from γ values of the concentrated solutions and were found to be in reasonable agreement with the values determined from the films, suggesting that these chromophores can retain their polymethines-like characteristics even after being processed into high number density films. The observed magnitude of $\text{Re}(\chi^{(3)})$ for all three salts are comparable to the best values reported using other polymethines-based films. The largest value was found to be 3.8×10^{-11} esu, which is more than two times larger than that of silicon ($\sim 1.4 \times 10^{-11}$ esu). It is worth noting that of all the complexes C6 exhibits the highest $\text{Re}(\chi^{(3)})$ value at 1.3 and 1.55 μm . This can be attributed to the presence of the multiply-charged counterion, which limits the intermolecular interaction in solid state, i.e. aggregation. A comparison against the $\chi^{(3)}$ value predicted from γ also supports this argument as C6 shows the closest correlation.

4.4 Summary

It is abundantly clear that the nature of counterions has a profound effect on the cyanines' compatibility with its medium. In Section 4.1, we established that the modification the structure of the cationic counterion of polymethine salts such that they exhibit high polarizability and moderate dipole moment improves the TCF-cyanines solid-state miscibility with APC. The retention of high optical quality of the guest-host films at a greater loading density afforded by these counterions along with the large $|\chi^{(3)}|$ that exceeded that of crystalline Si by three times enabled the integration of these TCF cyanines in SOH waveguides which demonstrated wavelength conversion via near-

degenerate FWM and optical power modulation of sideband. The $|\chi^{(3)}|$ and β measured in device configuration were also in a good agreement with those measured from a bulk films on glass substrates.

In Section 4.2, polymethines with di-cationic and hexa-cationic counterions were determined. The hexacation, in particular, exerts a moderately large coulombic force, resulting in pre-organization of the chromophores in their vicinity. The optical properties of the mono- and di-cationic complexes indicate that the charge localization and corresponding change in geometry upon excitation occur at a lower concentration likely due to intermolecular interactions, while the properties of hexa-cation are dominated by intramolecular ion-pairing interactions across all concentration. More detailed vibrational spectroscopic studies should be conducted to supplement this conclusion.

All variants of anionic TCF-terminated polymethines show large macroscopic third-order nonlinearities in high number density neat films with the one paired with hexacation yielding the highest $\text{Re}(\chi^{(3)})$ value of -3.6×10^{-11} esu at $1.55 \mu\text{m}$, more than twice larger than the value of silicon. However, TCF-polymethine complexes also show significant two-photon absorption at this wavelengths, resulting in a suboptimal $|\text{Re} \chi^{(3)}/\text{Im} \chi^{(3)}|$. Nevertheless, our results provide a better understanding of the impact of the counterions on the optical properties of polymethines, and provide an alternate method to tailor their electronic properties both at the molecular and bulk material level for device applications.

4.5 Experimental Details

4.5.1 Preparation of guest-host films

All dyes investigated in this chapter were synthesized by Zhong'an Li from the Jen group at the University of Washington. Glass substrates were sonicated in distilled water, acetone, and isopropanol sequentially before use. Equal parts of identical 6% by weight mixture of the polymethine dyes and APC dissolved in dibromomethane were added to produce the 50 wt. % dye-polymer blend solution for film casting. The 25% by wt. mixture was made by adding 3:1 ratio. The neat films were cast using 13% by wt. solution to account for the lower viscosity in absence of APC polymer in the mixture. The thin films for linear absorption measurement were cast using 1.5 wt. % solution. All films were cast using a Laurell Technologies WS-650-23 spin coater operated at 800 rpm for four minutes, followed by an overnight vacuum drying.

4.5.2 Refractive index and linear optical loss

The refractive indexes, thickness and optical loss of guest-host films were measured using a prism coupler (Meticon®, Model 2010) which was equipped with a 200-P-1 prism (code 995.4) and a scanning-fiber probe for optical loss measurement. The principles behind operation is summarized in Section 2.2.1. The light source used was a 1550nm CW diode laser operating at 4.2mW (Melles Griot, Diode Laser Driver 06DID203). The film thickness extracted from the prism coupling measurements agreed well with the values obtained using contact profilometry. (Dektak, 6M) The linewidth of

the coupled modes for A2 film were particularly broad with excessive loss of this film exceeding the instrumental limit of the scanning fiber measurement. (20 dB/cm)

4.5.3 Two-photon Induced Fluorescence (TPIF)

Principle: Two-photon induced fluorescence is a single-beam spectroscopic technique where the sample is degenerately two-photon excited using an intense monochromatic light. Upon a two-photon induced excitation, the sample decays from the excited state via fluorescence, and the emitted light is collected and quantified using either photomultiplier tubes or CCD camera. For an accurate measurement of the two-photon cross-section δ_{2PA} , the laser must be sufficiently detuned from one-photon resonance, and yet retain a spectral proximity to the two-photon band. This technique is a referential method, meaning that the two-photon spectrum of the reference compound must be known in order to scale accurately the two-photon cross-section of the sample. The reference used in generating **Figure 4.13** was dilue (2 μ M) fluorescein. The sample in question must exhibit a sufficient quantum yield, so that the number of photons emitted is within the detection limit of the setup. Once the two-photon absorption cross-section is obtained, one can determine the imaginary part of the third-order polarizability.

Setup: A laser source is coupled with an optical parametric amplifier that generates a tunable monochromatic pulse. The beam is routed to both the sample and the reference arms using a beam splitter. The photomultipliers are set up such that the fluorescence light from the sample and the reference are collected perpendicular to the incident excitation beam. A set of neutral density filters of known transmittance is placed between the sample and the detector, and is used to control the intensity of the signal reaching the

detector. As the laser frequency approaches the two-photon resonance, the intensity of the fluorescence is expected to increase; the filters are adjusted to attenuate the fluorescence reaching the detector, ensuring the reading of accurate photon counts while avoiding detection saturation. To prevent ambient light from reaching the PMT, the sample, filters and detectors are completely encased in the dark.

To ensure that the fluorescence is strictly due to the degenerate two-photon absorption, the intensity of the fluorescence signal should be measured at varying excitation energies, and its quadratic dependence on the incident pulse intensity must be verified. Once the integrated fluorescence is measured, the cross-section is obtained simply from the following formula.[44]

$$\delta_s = \delta_r \frac{F_s C_r \eta_r \Phi_r}{F_r C_s \eta_s \Phi_s} \quad (\text{Eq. 4.1})$$

where Φ is the fluorescence quantum yield. The collection efficiency factor η is given by the following ratio,[136]

$$\eta = \frac{1}{n^2} \left(\frac{\int f_{em}(\lambda) \cdot IRF(\lambda) \cdot \prod_i^n T_n \cdot d\lambda}{\int f_{em}(\lambda) d\lambda} \right) \quad (\text{Eq.4.2})$$

where n is the refractive index of the solvent used, f is the fluorescence count at a particular wavelength λ , IRF is the frequency dependent instrument response, and T is the transmittance of the filters used to attenuate any fluorescence reaching the detector. With the cross-section known, the nonlinear absorption coefficient, β can be obtained by multiplying δ_{2PA} by $N/\hbar\omega_e$.

4.6 References

13. Lin, Q., et al., *Dispersion of silicon nonlinearities in the near infrared region*. Applied physics letters, 2007. **91**(2): p. 21111-21111.
14. Bristow, A.D., N. Rotenberg, and H.M. van Driel, *Two-photon absorption and Kerr coefficients of silicon for 850–2200nm*. Applied Physics Letters, 2007. **90**(19): p. 191104.
15. Dinu, M., F. Quochi, and H. Garcia, *Third-order nonlinearities in silicon at telecom wavelengths*. Applied Physics Letters, 2003. **82**(18): p. 2954.
44. Sutherland, R.L., *Handbook of nonlinear optics*. 2003: CRC press.
54. Hales, J.M., et al., *Design of Organic Chromophores for All-Optical Signal Processing Applications*. Chemistry of Materials, 2013. **26**(1): p. 549-560.
59. Fu, J., et al., *Molecular structure two-photon absorption property relations in polymethine dyes*. Journal of the Optical Society of America B, 2007. **24**(1): p. 56-66.
60. Mukhopadhyay, S., et al., *Polymethine dyes for all-optical switching applications: a quantum-chemical characterization of counter-ion and aggregation effects on the third-order nonlinear optical response*. Chemical Science, 2012. **3**(10): p. 3103-3112.
96. Negres, R.A., et al., *Two-photon spectroscopy and analysis with a white-light continuum probe*. Optics letters, 2002. **27**(4): p. 270-272.
125. Bouit, P.-A., et al., *Continuous Symmetry Breaking Induced by Ion Pairing Effect in Heptamethine Cyanine Dyes: Beyond the Cyanine Limit*. Journal of the American Chemical Society, 2010. **132**(12): p. 4328-4335.
126. Bouit, P.-A., et al., *Stable Near-Infrared Anionic Polymethine Dyes: Structure, Photophysical, and Redox Properties*. Organic Letters, 2008. **10**(19): p. 4159-4162.
127. Vallaitis, T., et al., *Optical properties of highly nonlinear silicon-organic hybrid (SOH) waveguide geometries*. Optics Express, 2009. **17**(20): p. 17357-17368.

128. Lin, Q., O.J. Painter, and G.P. Agrawal, *Nonlinear optical phenomena in silicon waveguides: modeling and applications*. Optics Express, 2007. **15**(25): p. 16604-16644.
129. Koos, C., et al., *Nonlinear silicon-on-insulator waveguides for all-optical signal processing*. Optics Express, 2007. **15**(10): p. 5976-5990.
130. Jacobs, B.C. and J.D. Franson, *All-optical switching using the quantum Zeno effect and two-photon absorption*. Physical Review A, 2009. **79**(6): p. 063830.
131. Wen, Y.H., et al., *All-optical switching of a single resonance in silicon ring resonators*. Optics Letters, 2011. **36**(8): p. 1413-1415.
132. Spott, A., et al., *Photolithographically fabricated low-loss asymmetric silicon slot waveguides*. Optics Express, 2011. **19**(11): p. 10950-10958.
133. Bianco, A., M. Del Zoppo, and G. Zerbi, *Molecules with enhanced negative third order vibrational polarizabilities: polymethine dyes and their vibrational spectra*. Synthetic metals, 2001. **125**(1): p. 81-91.
134. Dähne, L. and G. Reck, *Deformation of Polymethine Structures by Intermolecular Interactions*. Angewandte Chemie International Edition in English, 1995. **34**(6): p. 690-692.
135. Giesecking, R.L., et al., *Impact of Bulk Aggregation on the Electronic Structure of Streptocyanines: Implications for the Solid-State Nonlinear Optical Properties and All-Optical Switching Applications*. The Journal of Physical Chemistry C, 2014. **118**(41): p. 23575-23585.
136. Makarov, N.S., M. Drobizhev, and A. Rebane, *Two-photon absorption standards in the 550-1600 nm excitation wavelength range*. Optics Express, 2008. **16**(6): p. 4029-4047.

CHAPTER 5

IMPLEMENTATION OF POLYMETHINE-HOST POLYMER BLENDS IN SILICON-ORGANIC HYBRID (SOH) CONSTRUCTS

5.1 Introduction

The promising optical properties of polymethines-polymer blend films discussed thus far were characterized and optimized on a bulk, featureless slab waveguides that are on the orders of a few millimeters to a few centimeters in size. For a functional SOH device operation, the same linear and nonlinear optical properties must also be seen when these materials are integrated onto miniaturized micro- and nano- scale waveguides. To ensure such, two conditions must be met: 1) the cross-sectional waveguide dimensions must be within a proper range to support single mode propagation, and 2) the NLO materials must cover and infiltrate the structures that produce the modal confinement without forming voids or scattering sites.

5.1.1 Numerical Aperture of Waveguides and Single-mode Propagation

Single-mode propagation is particularly important in ensuring the speed of operation and the signal fidelity because it can circumvent the problems of intermodal dispersion seen in multi-mode waveguides – the spread of signal in time associated with the different group velocities between the modes.[137] The single mode guiding conditions for

varying types of waveguides are well-understood, and the equations that govern these conditions have been solved for various geometries of the waveguides including rectangular strip and slot waveguides.[138-141] The analytical solutions to these equations, which dictate the permissible cross-sectional dimensions for single mode propagation, contain the following waveguide numerical aperture term.

$$NA = \sqrt{n_{core}^2 - n_{cladding}^2} \quad (\text{Eq. 5.1})$$

Thus, the knowledge of precise refractive index of the cladding at the operating wavelength is critical. Moreover, the problem of chromatic dispersion commonly seen in optical fibers can also be present in waveguides depending on the propagation lengths. Hence, elucidation of the dispersive behavior of cladding material is particularly important in the fabrication of a functional waveguide containing device.

5.1.2 Solution-Processing of Organic Cladding

Up to this point, successful infiltration of organic materials in SOH devices has been accomplished on a limited scope through vapor-phase deposition of discrete chromophores[129] or solution casting of chromophore guest-polymer host blends.[73, 127] While the former route is capable of producing good optical quality films, it is limited to molecules that can be sublimed without thermal decomposition. Thus, solution processing approaches provide a greater utility to a much wider range of molecular systems. For instance, casting of guest-host blends allows one to use molecular engineering approaches to optimize the optical and physical properties of discrete molecules, while taking advantage of the processability of well-established host

polymers. Furthermore, solution processing opens up the possibility of achieving materials with a high degree of molecular order^{xx} through thin-film crystal growth methods.[142-144]

The difficulty in solution processing of the organic NLO materials onto Si and other substrates arises from the fact that processable organic solutions are typically hydrophobic, whereas the surfaces of these substrates are hydrophilic due to the presence of a native oxide surface layer. This issue is compounded in the micro- to nano- scale device applications as the substrates exhibit very large surface-to-volume ratios. Therefore, reduction of the surface energy mismatch is crucial for homogenous coverage and conformal infiltration of the organic NLO cladding.

5.2 Linear Dispersion Behaviors and Optical Nonlinearities of Host Polymers and Dye-APC Guest-Host Film

To interpret dispersion curves such as the ones in **Figure 5.2**, it is helpful to understand the models from which the dispersion curves can be generated. The oldest description of dispersion is given by Cauchy's equation,[145]

$$n(\lambda) = A + \frac{B}{\lambda^2} + \frac{C}{\lambda^4} \quad (\text{Eq. 5.2})$$

where A, B, and C are constants unique to a medium. Cauchy's equation, while only an empirical equation that models materials with normal dispersion,^{xxi} and whose constants

^{xx} Using anisotropic polarization dependence, the enhancements by a factor of ~5 can be achieved for third-order NLO responses relative to isotropic systems.

A, B, and C holds no meaningful physical quantity of equivalence, is still widely considered valuable in modeling dispersive behavior in a transparent region away from any resonances. To account for the dispersion behavior near resonances, Sellmeier's equation is employed instead.

$$n^2(\lambda) = 1 + \frac{A_0\lambda^2}{\lambda^2 - \lambda_0} + \frac{A_1\lambda^2}{\lambda^2 - \lambda_1} + \frac{A_2\lambda^2}{\lambda^2 - \lambda_2} \dots \quad (\text{Eq. 5.3})$$

Unlike Cauchy's equation, the constants in each term of the sum in Sellmeier's equation holds physical meanings; A_i represents the oscillator strength at a resonant wavelength of λ_i . [145] The number of terms required to generate a reasonable dispersion curve depends on the number of resonances (oscillators) and the empirical values of refractive indexes available at near those corresponding resonances.

5.2.1 Dispersive behaviors of neat APC, PMMA polymer films and a dye-doped polymer blend

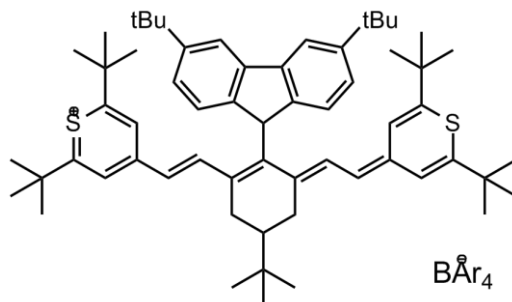


Figure 5.1. Structure of **B6**, a modified thiopyrylium-terminated heptamethine

^{xxi} In the regions of anomalous dispersion, Cauchy model would show a very gradual, asymptotic curve, instead of a rapid drop and rise seen typically associated with dispersion near resonance.

For the characterization dye-polymer blend film, the chromophore used was compound **B6** from our recent publication[120] based on its low linear loss in amorphous polycarbonate (APC) film blend, and its extensively characterized nonlinear optical properties. For prism coupling experiments, a **B6**/APC film blend thick enough (ca. 1.2 μ m) to couple at least two modes of 1550 nm light for an accurate index determination^{xxii} was spin-cast on fused SiO₂ substrate. The same film, however, could not be used for spectral ellipsometry due to the lack of reflectivity required. Instead, a relatively thick (ca. 3 μ m) a *neat* **B6** film with sufficient reflectivity was blade-cast on an opaque surface, allowing spectral ellipsometric measurements. The dispersion data from this neat film can be used to model semi-empirically the dispersion of the dye-APC film using effective medium approximation (EMA),[146-148] provided that the dispersion of the neat APC host is also available. Therefore, the dispersive behaviors of the neat host polymer films were also characterized simultaneously.

Table 5.1. Refractive indexes of neat APC, poly(methyl methacrylate) (PMMA), and 50 wt% **B6**/APC film determined using prism coupling

	n_{633nm}	n_{830nm}	n_{1060nm}	n_{1300nm}	n_{1550nm}
APC	1.5803	1.5726	1.5653	1.5610	1.5591
PMMA	1.4924	1.4852	1.4829	1.4818	1.4812
B6/APC	<i>N/A</i>	<i>N/A</i>	<i>N/A</i>	1.7472	1.6767

N/A: Not available due to excessive absorption loss

^{xxii} Refer to Section 2.2.1

The refractive indexes of pure APC and PMMA thin films were measured using the prism coupling technique at rather large wavelength increments of 633, 830, 1060, 1300, and 1550 nm due to the limitation on the available laser diode sources. For neat polymer films, these results are summarized in **Table 5.1**. The refractive indexes of the dye-host polymer film blend were limited to 1300 nm and 1550 nm due to severe absorption losses at lower wavelengths, and the associated mode broadening beyond the detection range.

It is immediately apparent that APC possesses larger refractive index than PMMA across all visible and near-infrared (NIR) wavelengths. Hence, we can deduce that cladding consisting of dye-APC blends would yield a tighter confinement in waveguides than that consisting of dye-PMMA blends. This result, coupled with the fact that the most promising class of NLO molecules indentified in this thesis thus far (Chapter 3) – chalcogenopyrylium heptamethines – form high optical quality film in APC, makes APC an ideal host polymer platform.

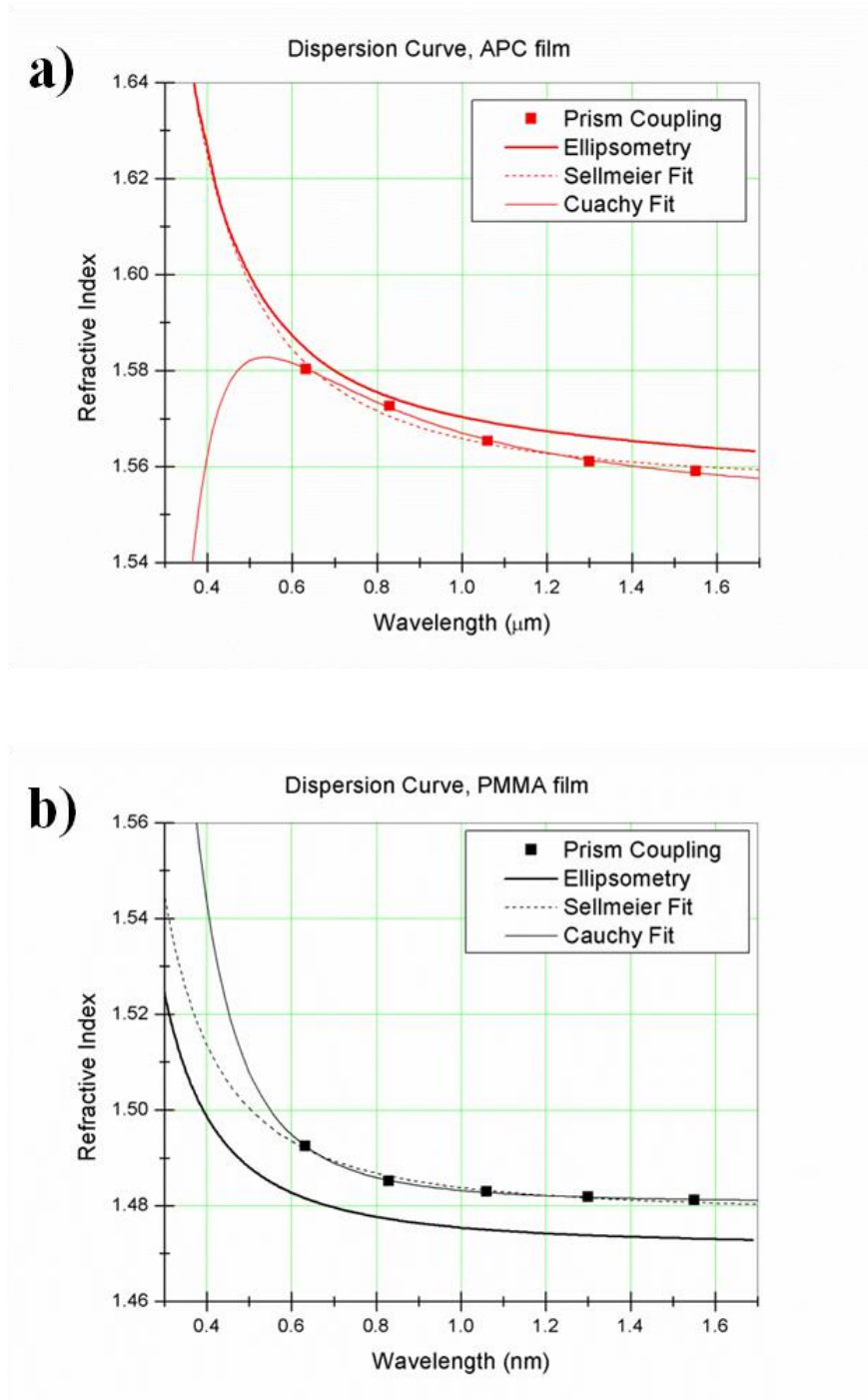


Figure 5.2. Dispersion curves of neat host polymer ca. $2\mu\text{m}$ thick a) APC, and b), generated using a least square fit of the measured indexes to Cauchy's and Sellmeier's equations, and spectral ellipsometry.

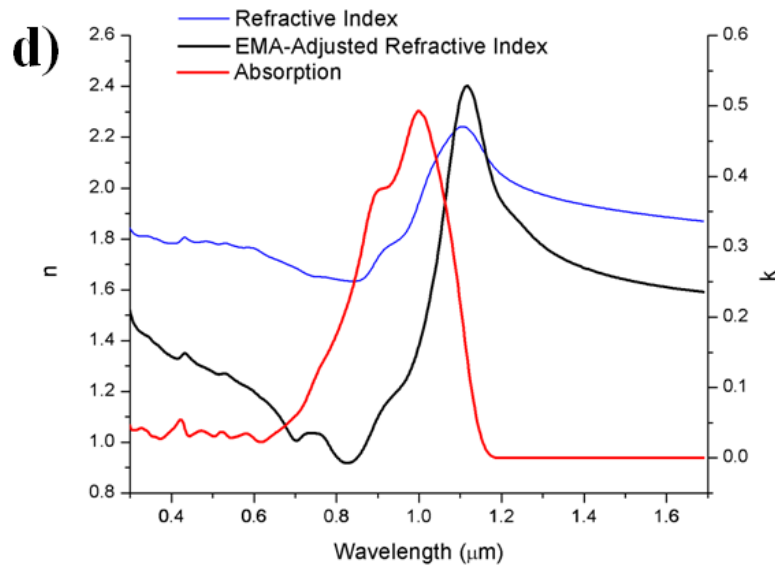
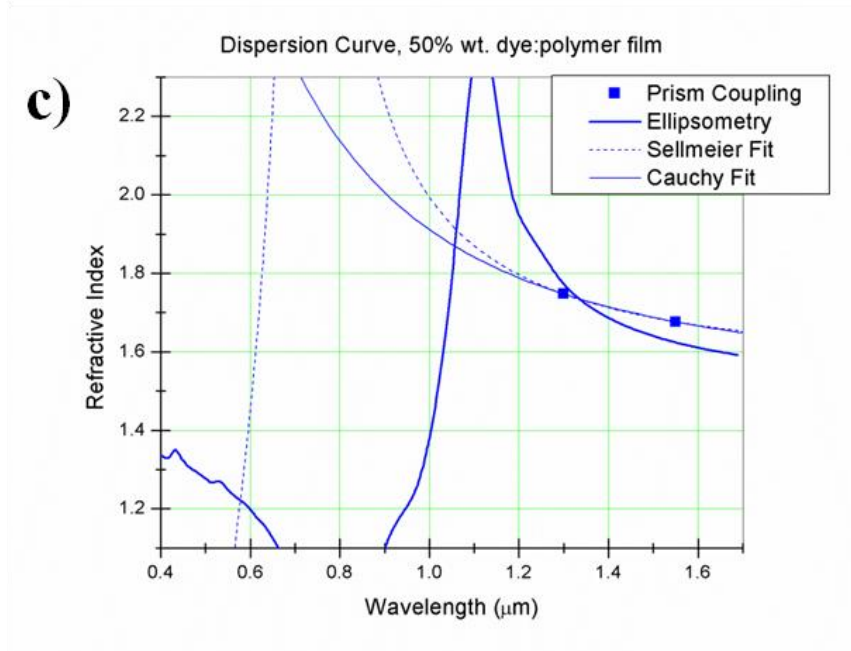


Figure 5.3. Dispersion curves of c) 50 wt% **B6**/APC film ca. 1.2 μm thick, generated using a least square fit of the measured indexes to Cauchy's and Sellmeier's equations, and spectral ellipsometry. d) Plot of the real and imaginary part of complex refractive index, n (blue) and k , (red) respectively, generated using effective medium approximation.

(EMA) in modeling the ellipsometric data of 2 μm thick neat APC, and 1.6 μm thick neat **B6** films separately.

Figure 5.2. and **5.3** show the dispersion curves obtained prism coupling and spectrometric ellipsometry, which were then fit to dispersion curves generated using Sellmeier and Cauchy dispersion functions. Due to the lack of index values near the resonance in the cases of APC and PMMA neat films, the Cauchy model produces a more precise fit in the near-IR region. With only two empirically determined index values available, we are unable to distinguish the quality of the fit for the **B6**/APC blend film. The dispersion of the *neat* **B6** films measured using spectral ellipsometry, and the corresponding EMA-adjusted dispersion of the **B6**/APC, with an assumed volume fraction $f = 0.4$,^{xxiii} shows a good agreement with the dispersion curve generated from the prism coupling.

The slight offset seen between the dispersion generated from prism coupling and ellipsometry can be attributed mainly to two sources; 1) there are contrasting reports on the dispersion data on gadolinium gallium garnet crystal of which the prism in our prism coupling experiment is consisted,[149-151] and 2) the surface of the neat polymer has non-negligible surface roughness which increases the mean square error against the model used to fit ellipsometric data. Nonetheless, since the dimensional analysis of most waveguides for single mode propagation involves indexes with two-decimal-digit accuracy, the offset of less than 0.6% still yields useful dispersion curves that can serve as a guideline for waveguide design.

^{xxiii} assuming identical densities, $f=0.4$ correspond to 40 wt%

The least squares fits generated using Cauchy and Sellmeier's equations yield a set of coefficients that can be used to quickly replicate these dispersion curves. The values of these coefficients are given in **Table 5.2** and **5.3**.

Table 5.2. Cauchy and Sellmeier coefficients using single-term expressions

		APC	PMMA	B6/APC
Cauchy	A	1.556	1.478	1.510
	B	0.0103	0.0054	0.4018
Sellmeier	A₀	0.3946	0.3392	1.416
	λ₀	0.7717	0.7647	0.5239

Table 5.3. Cauchy and Sellmeier coefficients using the conventional forms (two-terms for Cauchy and three oscillators for Sellmeier)

		APC	PMMA	B6/APC
Cauchy	A	1.552	1.481	1.347
	B	0.0180	0.0013	1.067
	C	0.0026	0.0014	0.660
Sellmeier	A₀ = A₁ = A₂	0.4736	0.3953	0.4721
	λ₀ = λ₁ = λ₂	0.0214	0.0130	0.5240

As can be seen from the larger value of the coefficient **B**, **B6/APC** films shows greater wavelength dependence of its refractive index compared to the neat polymer films. This is consistent with the added resonance effect from the presence of NIR absorbing dye.

The resonant wavelengths represented by Sellmeier coefficient, λ_0 , however, are highly misleading as the lack of near resonance index values leads to incorrect assignments. The resonant wavelengths calculated from the dispersion curves generated using single oscillator Sellmeier's equation overestimate the resonant wavelengths of the neat polymer films and underestimate that of the dye-polymer blend. The conventional form of the equation (Eq. 5.2) yields Sellmeier coefficients, λ_0 , that are significantly shorter than the measured resonant wavelengths in all three samples.

5.3 Improving Cladding Infiltration via Substrate Surface Modification

The coverage and infiltration of the waveguide structures are particularly important from the linear loss perspective. Our past collaboration with the Eich group at TUHH^{xxiv} have revealed that linear loss of the guest-host polymer measured in sub-micron devices are often much higher than that measured in large slab waveguides. (i.e. 5 dB/cm vs. 17 dB/cm in 50 wt% TCF-terminated polymethine:PMMA blends) The post mortem scanning electron microscopy (SEM) images of spin-cast film blends on unmodified surfaces revealed the likely sources of this undesirable additional loss: voids and scattering sites along the organic-inorganic interface from partial delamination near the micro- features. This problem was more evident in the dye-APC blend than the dye-PMMA film as the propagation loss in the former could not be measured due to near-complete extinction. (**Figure 5.4**)

^{xxiv} Technische Universität Hamburg-Harburg

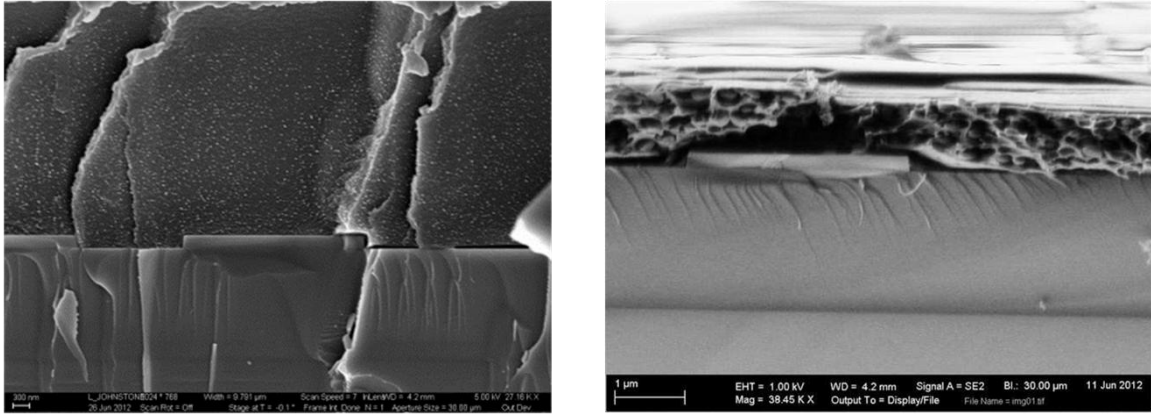


Figure 5.4. Cross-sectional SEM images of polymer clad waveguides: (left) freeze-fractured TCF-polymethine/PMMA, (right) room-temperature fractured **B6/APC** on on fused SiO₂ waveguides. Images taken with the aid of Dr. Joel M. Hales, Lucas Johnstone.

Thus, for efficient propagation of confined light through the NLO active film material, it is critical for the coverage of the substrate and the infiltration of the features to be complete and homogenous. In this section, we report a method in which the surface energy mismatch can be reduced.

5.3.1 Surface Modification

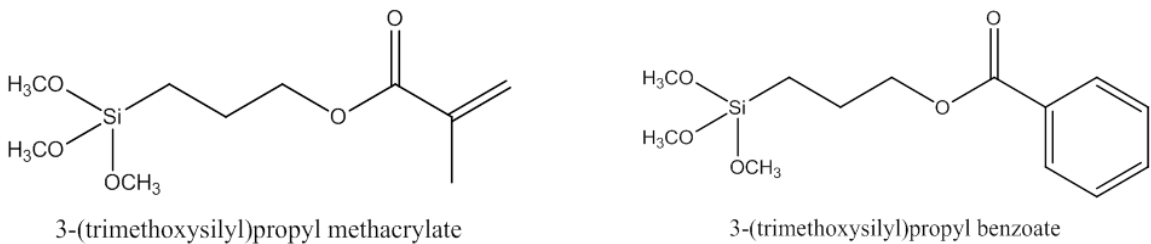


Figure 5.5. Structures of the alkoxy silane coupling agents. (Left) (3-methacrylpropyl) trimethoxysilane, and (right) (3-benzoylpropyl) trimethoxysilane (referred as, PM and PB, respectively), for substrate surface modification^{xxv}

^{xxv} Other names: methacrylpropyl trimethoxysilane, benzoyloxypropyl trimethoxysilane

To reduce the surface energy mismatch, and thus, promote better wetting and adhesion, we functionalized the surface of the substrate with a monolayer of (3-benzoylpropyl)-trimethoxysilane (PB) and (3-methacrylpropyl)trimethoxysilane (PM) and using well-known silane coupling chemistry.[152-154] These “tail” groups are chosen based on the anticipated “compatibilizing” attractive interaction between the modified surface and the host polymer, based on their structural similarity and the projected similarity in the static dipole moment and linear polarizability. This is shown schematically in **Figure 5.6**.

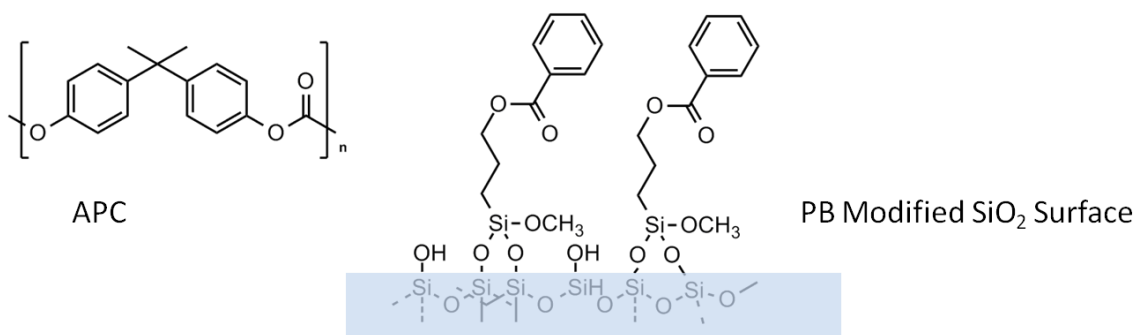


Figure 5.6. Structure of amorphous polycarbonate (APC) and the binding of the PB on silica substrate.

Owing to the possibility of polycondensation to form Si–O–Si linkages between the coupling agents themselves rather than with the substrate, [155] careful control of reaction conditions and moisture content is required to obtain well-defined monolayers. Thus, the procedures in Reference [154] were strictly followed in the preparation of the substrate and reaction solution. Two sets of different reaction conditions were investigated for possible differences in the thicknesses of the assembled layers, and in the smoothness of the surfaces. (Details are given in Section 5.5.3) It is also worth noting that this approach has also been shown to be applicable to SiN,[152, 156, 157] which

may be a useful alternative substrate material given its large refractive index. (< 1.95 at 1.55 μm)

5.3.2 Characterization of Functionalized Surfaces

The presence of a monolayer of the benzoate- and methacrylate- containing silane modifier, and thus the overall feasibility of the approach was determined by using X-ray photoelectron spectroscopy (XPS) and ellipsometry.

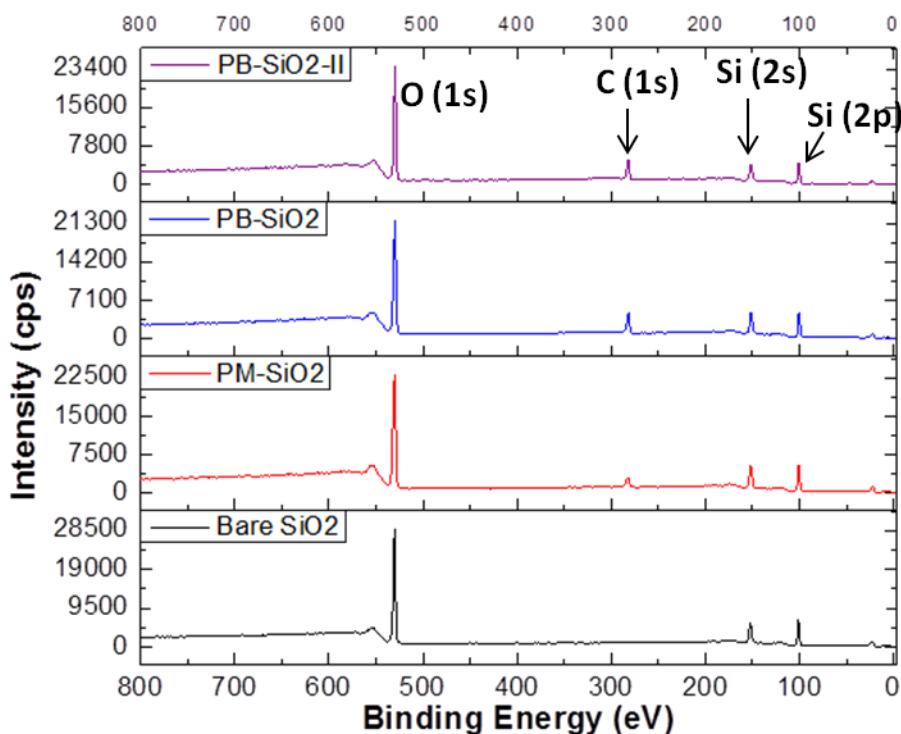


Figure 5.7. XPS spectra of fused SiO₂ surface modified with PB and PM layers

Figure 5.7 shows XPS spectra of three different modified surfaces – two obtained from the reactions with PB at varying concentrations and duration, and third modified with PM. Despite the visible differences from the spectra, direct comparison between the

integrated areas of C(1s) between PB and PM modified surfaces are not quantitatively meaningful as the number of carbons and the nature of hybridizations of their bonds are different. Therefore, the *relative* integrated peak areas of C(1s) against Si(2p) are used to confirm the presence, and extrapolate the thicknesses of these layers under the presumption of the same depths of X-ray penetration into Si, or SiO₂ substrate for each sample.

The thickness values are compared against the theoretically predicted ones obtained using inelastic mean-free path (IMFP) and those obtained from ellipsometry. (**Table 5.4**) The IMFP – an index of how far an electron can travel through a solid before losing energy – can be used to calculate the effective physical length of a single molecule, given information on the hybridization of the bonds that are involved in its structure.[158]

Table 5.4. Thicknesses of the self-assembled layers of the silane coupling agents on SiO₂ substrate

	Thickness (nm)		
	Theoretical IMFP	XPS	Ellipsometry
PB- Method I	1.01	1.03 ± 0.1	0.75 ± 0.3 ^a
PB- Method II	1.01	1.45 ± 0.2	1.2 ± 0.4
PM- Method I	0.79	1.59 ± 0.2	1.75 ± 0.3

^a Global minimum was not found in the fitting of the ellipsometric data. The MSE was large ranging from 2 to 3.

The greater percent error in the ellipsometric data arises from the difficulties in modeling due to the interference fringes of the fused silica substrates. The can be improved with the

use of reflective and less transparent substrate of similar nature as SiO₂, such as Si wafer. Nonetheless, the thicknesses obtained from all three samples suggest formation of near-monolayers of the silane coupling agents. Method II which involved a longer reaction time (12h) in a lower concentration solution (0.3 wt% PB in dry toluene) yielded slightly thicker layer with more consistent thickness measurements. Thus, this sample was chosen for AFM analysis shown below. When exposed to the same reaction conditions as PB-Method I, PM shows a formation of a thicker layer, possibly a bi-layer, with its total thickness comparable to twice the length of the molecule predicted by IMFP.

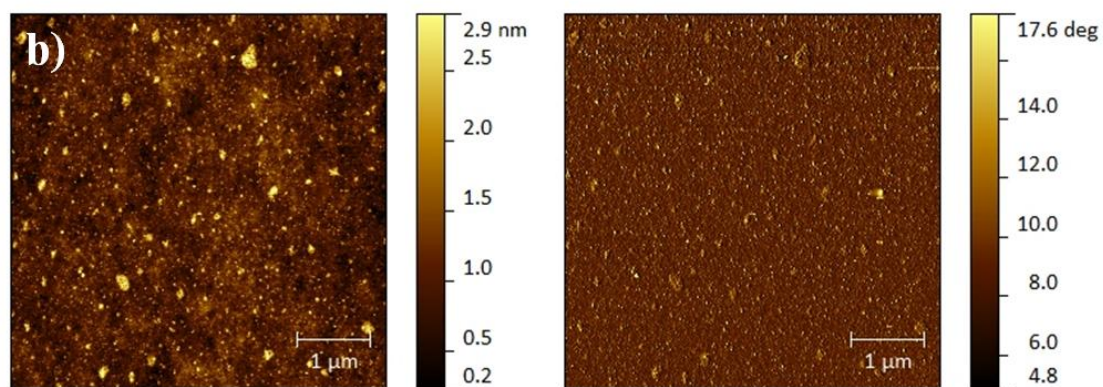
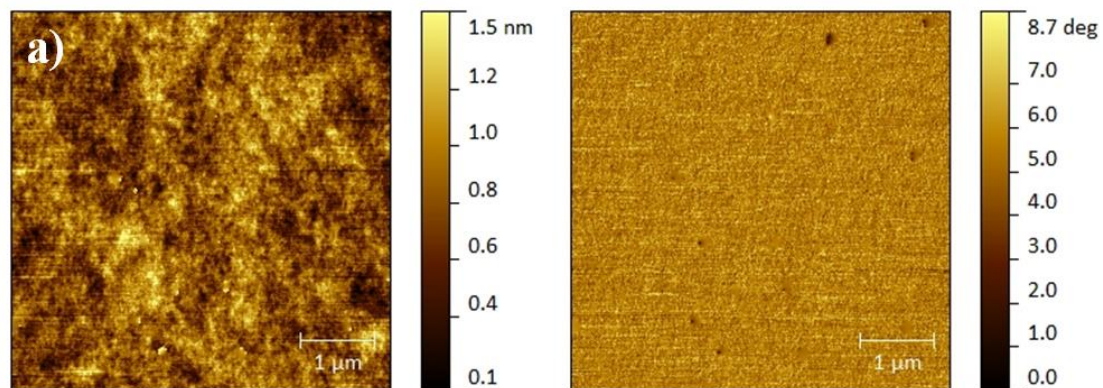


Figure 5.8. AFM topographical (left) image and phase image (right) from a $5 \times 5 \mu\text{m}$ area of a) oxygen-plasma etched, and b) benzoylpropyl trimethoxysilane (PB) modified fused silica substrate measured using amplitude-modulation mode

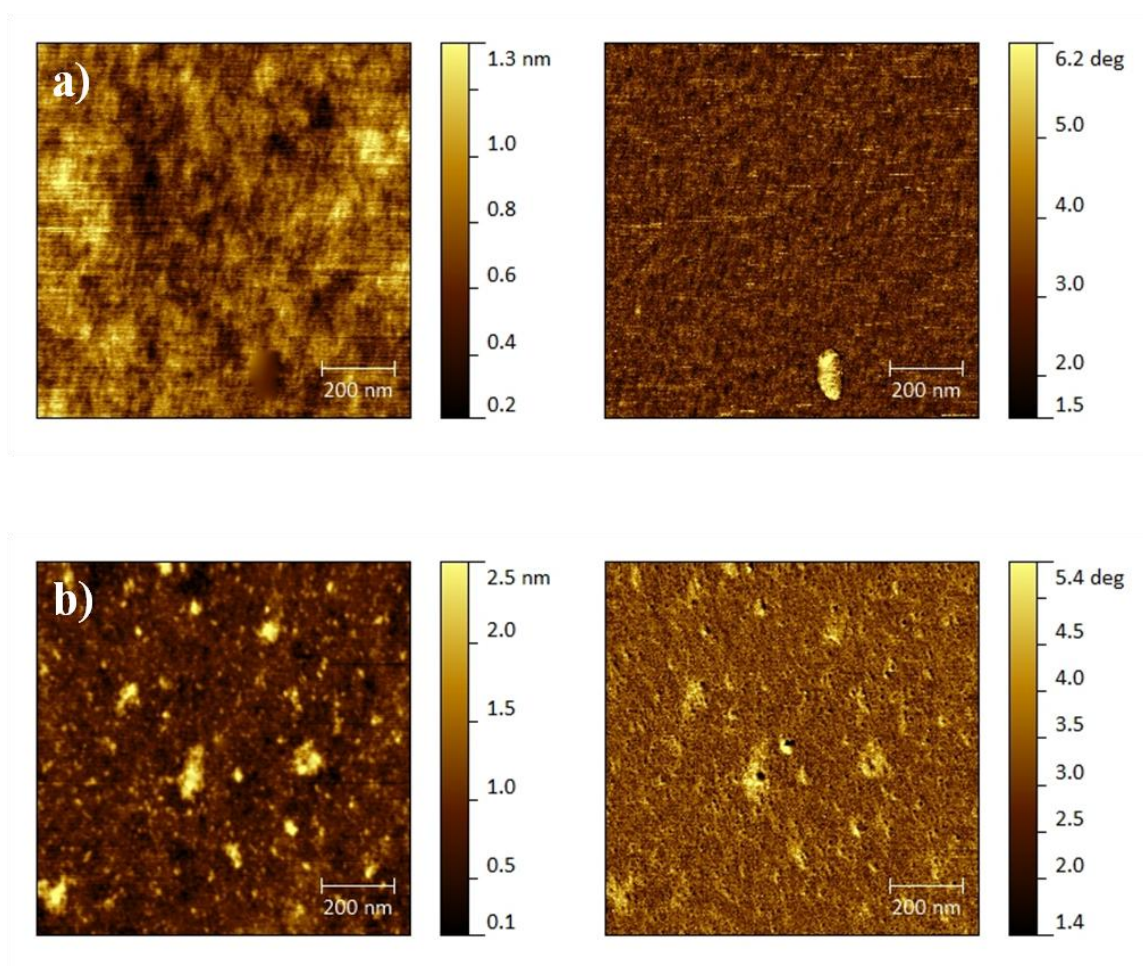


Figure 5.9. AFM topography (left) image and phase image (right) from a $1 \times 1 \mu\text{m}$ area of a) oxygen-plasma etched, and b) benzoylpropyl trimethoxysilane (PB) modified fused silica substrate measured using amplitude-modulation mode

Table 5.5. Root mean square (RMS) surface roughness, and phase of the bare, and PB modified substrate from AFM images

Sample	RMS roughness (nm)	Phase (°)
Bare SiO ₂	0.210	0.666
PB modified SiO ₂	0.367	1.48

Atomic force microscopy (AFM) reveals the quality and smoothness of the functionalized surfaces, both in terms of topography and friction/phase. Any significant difference in topography would indicate either the occurrence of polycondensation of silanes along the different locations on the substrate, or incompleteness of the coverage. Topographical images can be also supplemented by phase images obtained through the force modulation microscopy mode (tapping mode) of the AFM, as they represent the differences in the elasticity of the surface.[159]

As seen in the **Figure 5.8**, and **5.9**, the overall differences in the RMS roughness from the topographical images indicate that a noticeable increase in the surface roughness was introduced during the surface functionalization process. However, considering that typical features found in the strip or slot waveguides are hundreds of nanometer in height, we conclude that such increase ($< 0.2\text{nm}$) in the roughness can be considered negligible in the context. The phase image reveals a near complete coverage of the surface except for a handful of small spots ($< 20\text{nm}$ in diameter) that show the same phase as the bare SiO₂ substrate. The average increase of 0.8 degrees in phase suggests that the surface has indeed become more elastic.

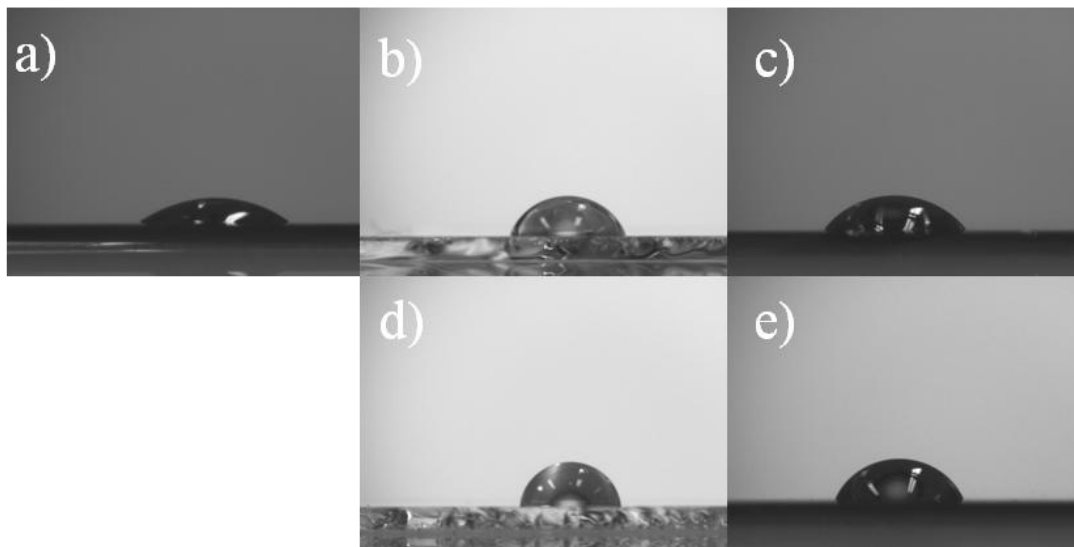


Figure 5.10. Images of distilled water droplets on various surfaces taken using contact-angle goniometer. a) Oxygen-plasma etched fused silica b) 1.6 μm thick APC film, c) 1.4 μm thick PMMA film, d) 3-(trimethoxysilyl)propyl benzoate (PB) modified surface, and e) 3-(trimethoxysilyl)propyl methacrylate (PM) modified surface

Table 5.6. Critical surface tensions of different substrate surfaces

Substrate	Contact Angle ^a (°)	Surface Tension (mJ/m ²)
Etched SiO ₂	40.9 ± 4.0	58.88
APC	84.9 ± 4.9	31.86
PB	64.9 ± 4.2	44.85
PMMA	71.5 ± 4.6	40.99
PM	53.8 ± 3.8	50.32

^a The errors bars are obtained from the standard deviation of the differences in the contact angles between the left and right tangents.

With the presence of the PB and PM monolayers confirmed, and their coverage examined, the changes to physical properties of the functionalized surfaces were investigated using contact-angle goniometry. Definition of a contact angle is given as the angle between the tangent at the juncture where liquid-vapor interface meets a solid surface and the normal of the said surface. In addition to the hydrophilicity/phobicity, this angle can be used to determine referentially the critical surface tension^{xxvi} (surface energy) of a solid substrate, given the critical surface tension of 73mJ/m² for water at 20°C. [153]

As summarized in **Table 5.6**, both PB and PM modified surfaces exhibit greater hydrophobicity compared to the oxygen plasma-etched bare SiO₂ surface evidenced by smaller contact angle and lowered critical surface tension. The surface energy mismatch between APC and the substrate was reduced from ca. 27 mJ/m² to 13 mJ/m² by the deposition of PB monolayer. The effect was less drastic for the PM modification as the mismatch was reduced from 18 mJ/m² to 10mJ/m². The smaller surface energy mismatch between PMMA and the SiO₂ surface even without the presence of PB coupling agent justifies the better adhesion properties seen in the SEM images of cladded waveguides. **(Figure 5.4)**

^{xxvi} Units \approx mJ/m², dyne/cm, mN/m



Figure 5.11. Optical micrographs of 50% wt. dye-APC blend cast on a) unmodified SiO₂ substrate, and b) 3-benzoylpropyl trimethoxysilane (PB) functionalized substrate. The scale bar is 100 μm and is the same for all frames.

Figure 5.11 shows 40× optical micrographs of micron-sized features on SiO₂ substrates clad with B6/APC blend. The optical quality of the cladding on the PB modified surface showed a noticeably improved optical quality with the lack of the unfiltered areas, bubbles or the granular features seen in the film cast on the unmodified surface, confirming the improvement in the coverage and infiltration of polymer layer.

5.4 Summary

The dispersion curves for the neat APC, PMMA films and chalcogenopyrylium-terminated dye **B6**/APC film blend were generated using prism coupling and spectral ellipsometry. The associated Sellmeier and Cauchy coefficients were obtained using the least squares fit functions. The dispersion of the neat APC and PMMA thin curves from these two distinct techniques films were in good agreement, with APC showing greater refractive index across all wavelengths as predicted. The results of these studies were communicated to the collaborating engineers to serve as guiding parameters for tailoring a second-generation of waveguide devices specifically designed to support single mode propagation through the 50 wt% chalcogenopyrylium-heptamethine/APC cladding.

Fused silica substrate surface was successfully functionalized with a benzoyloxy- and methacryl- group containing silane coupling agents. The formation of monolayers and quality of their coverage was confirmed by XPS and AFM. The surface energy mismatch between the neat polymer films, and the newly modified surfaces determined via contact angle goniometry was $\leq 13 \text{ mJ/m}^2$, near two-fold improvement. The optical micrographs of deposited film on the substrates containing micron-sized features show a significant improvement in both wetting properties and subsequent coverage corroborating the effectiveness of this approach.

5.5 Experimental Details

5.5.1 Preparation of Blade-cast Thick Films for Ellipsometry

Thick films of neat APC, PMMA polymers and B6 polymethine were blade-cast using 10, 13, and 12 wt% solutions in 1,1,2-trichloroethane, respectively. The blade height was set to 15 μm , was dragged manually ca. 1 cm/s. Resulting thicknesses of the neat films after drying in a sealed dark chamber were 2.0, 2.2, and 1.6 μm , respectively.

5.5.2 Prism Coupling Experiment on Thin Films

Laser diode sources for the 405nm, 830nm and 1300nm CW light were Thorlabs LPS-405SF10-FC/PC, 830-FC, and 1300-FC single mode pigtail fibers putting out ca. 10mW of optical power. 633nm CW light was provided by a built-in He-Ne laser from Metricon 2010 Prism Coupler. The laser diodes and TEC were driven by Thorlabs ITC4001 driver.

5.5.3 Preparation of Functionalized Surfaces

All fused silica substrates were ultrasonicated with acetone and isopropanol for 15 minutes prior to being etched with cold oxygen-plasma at 750 W for four minutes. Dry toluene was prepared by stirring with molecular sieve for 2 hours. The reaction solution for Method I and II were 2% v/v and 0.3% v/v benzoyloxypropyl trimethoxysilane in dry toluene, respectively. The reaction allowed to take place in a dark chamber containing the reaction solutions for 2 and 12 hours for Method I, and II, respectively. The washing and curing procedures for removing of the physisorbed layer are described by Reference [154].

5.5.4 Characterization Techniques for Functionalized Surfaces

The morphology of the films was investigated using Zeiss Ultra 60 Scanning Electron Microscope. All SEM images were taken with the help of Mr. Lucas Johnstone of the Perry group at Georgia Institute of Technology.

XPS measurements were carried out on a Kratos Axis UltraDLD spectrometer using a monochromatic Al(K α) source by Dr. O'neil L. Smith of the Marder/Perry group at Georgia Institute of Technology. All the measurements were acquired at take-off angle of 70° relative to the surface normal at pass energies of 160 eV and 20 eV for surveys and high resolution data, respectively.

The topographical and phase images of the functionalized silica substrates were taken with the help of Dr. Anthony Giordano from the Marder group at Georgia Institute of Technology using both the contact and tapping mode of the Agilent N9524B Atomic Force Microscope with the conical spike height of 200nm and 1nm radius.

All ellipsometric measurements and modeling were performed by Dr. Canek Fuentes from the Kippelen group at Georgia Institute of Technology using J.A. Woollam M-2000UI Spectroscopic Ellipsometer.

5.6 References

73. Hochberg, M., et al., *Terahertz all-optical modulation in a silicon–polymer hybrid system*. *Nature materials*, 2006. **5**(9): p. 703-709.
120. Barlow, S., et al., *Polymethine materials with solid-state third-order optical susceptibilities suitable for all-optical signal-processing applications*. *Materials Horizons*, 2014. **1**(6): p. 577-581.
127. Vallaitis, T., et al., *Optical properties of highly nonlinear silicon-organic hybrid (SOH) waveguide geometries*. *Optics Express*, 2009. **17**(20): p. 17357-17368.
129. Koos, C., et al., *Nonlinear silicon-on-insulator waveguides for all-optical signal processing*. *Optics Express*, 2007. **15**(10): p. 5976-5990.
137. Ramaswami, R., *Optical fiber communication: from transmission to networking*. *Communications Magazine, IEEE*, 2002. **40**(5): p. 138-147.
138. Mullner, P. and R. Hainberger, *Structural optimization of silicon-on-insulator slot waveguides*. *Photonics Technology Letters, IEEE*, 2006. **18**(24): p. 2557-2559.
139. Pogossian, S.P., L. Vescan, and A. Vonsovici, *The single-mode condition for semiconductor rib waveguides with large cross section*. *Lightwave Technology, Journal of*, 1998. **16**(10): p. 1851-1853.
140. Soref, R.A., J. Schmidtchen, and K. Petermann, *Large single-mode rib waveguides in GeSi-Si and Si-on-SiO₂*. *Quantum Electronics, IEEE Journal of*, 1991. **27**(8): p. 1971-1974.
141. Tong, L., J. Lou, and E. Mazur, *Single-mode guiding properties of subwavelength-diameter silica and silicon wire waveguides*. *Optics Express*, 2004. **12**(6): p. 1025-1035.
142. Thakur, M., et al., *Thin single crystal films of organics; waveguiding in PTS films*. *Synthetic Metals*, 1989. **28**(3): p. D595-D604.
143. Thakur, M. and S. Meyler, *Growth of large-area thin-film single crystals of poly(diacetylenes)*. *Macromolecules*, 1985. **18**(11): p. 2341-2344.
144. Kwon, S.-J., et al., *Large-area organic electro-optic single crystalline thin films grown by evaporation-induced local supersaturation with surface interactions*. *Crystal Growth and Design*, 2009. **9**(5): p. 2512-2516.

145. Jenkins, F.A. and H.E. White, *Fundamentals of Optics 4th edition*. Fundamentals of Optics 4th edition by Francis A. Jenkins, Harvey E. White New York, NY: McGraw-Hill Book Company, 1976, 1976. **1**.
146. Aspnes, D., J. Theeten, and F. Hottier, *Investigation of effective-medium models of microscopic surface roughness by spectroscopic ellipsometry*. Physical Review B, 1979. **20**(8): p. 3292.
147. Jellison Jr, G., M. Chisholm, and S. Gorbatkin, *Optical functions of chemical vapor deposited thin-film silicon determined by spectroscopic ellipsometry*. Applied Physics Letters, 1993. **62**(25): p. 3348-3350.
148. Tinga, W.R., W.A.G. Voss, and D.F. Blossey, *Generalized approach to multiphase dielectric mixture theory*. Journal of Applied Physics, 1973. **44**(9): p. 3897-3902.
149. Hoefler, C., K. Kirby, and L. DeShazert, *Thermo-optic properties of gadolinium garnet laser crystals*. JOSA B, 1988. **5**(11): p. 2327-2332.
150. Wood, D.L. and K. Nassau, *Optical properties of gadolinium gallium garnet*. Applied optics, 1990. **29**(25): p. 3704-3707.
151. Weber, M.J., *Handbook of optical materials*. Vol. 19. 2002: CRC press.
152. Yanez, J.A., et al., *The adsorption of tri alkoxy silane on silicon nitride for colloidal processing*. J. Eur. Ceram. Soc., 1998. **18**: p. 1493–1502.
153. Arkles, B., *Silicon Compounds: Silanes and Silicones, Gelest Catalogue, Gelest. Inc., Tullytown, 2000*.
154. Kim, J., et al., *Formation, structure, and reactivity of amino-terminated organic films on silicon substrates*. Journal of colloid and interface science, 2009. **329**(1): p. 114-119.
155. Mutin, P.H., G. Guerrero, and A. Vioux, *Hybrid materials from organophosphorus coupling molecules*. J. Mater. Chem., 2005. **15**: p. 3761-3768.
156. Awsiuksa, K., et al., *Protein adsorption and covalent bonding to silicon nitride surfaces modified with organo-silanes: Comparison using AFM, angle-resolved XPS and multivariate ToF-SIMS analysis*. Coll. Surf. B, 2013. **110**: p. 217–224.

157. Tsukruk, V.V. and V.N. Bliznyuk, *Adhesive and Friction Forces between Chemically Modified Silicon and Silicon Nitride Surfaces*. *Langmuir* 1998. **14**: p. 446-455.
158. Cumpson, P.J., *Estimation of inelastic mean free paths for polymers and other organic materials: use of quantitative structure–property relationships*. *Surface and interface analysis*, 2001. **31**(1): p. 23-34.
159. Schirmeisen, A., B. Anczykowski, and H. Fuchs, *Dynamic Modes of Atomic Force Microscopy*, in *Springer Handbook of Nanotechnology*, B. Bhushan, Editor. 2007, Springer Berlin Heidelberg. p. 737-766.

CHAPTER 6

CONCLUSIONS AND FUTURE OUTLOOK

By now, it is evident that the silicon deficiencies, mentioned in Chapter 1, are not the ones which have a quick, singular, all-encompassing solution. The body of work presented in this thesis provides a set of incremental, yet important advances that have been made in the field of chemistry, nonlinear optics, and material science for development of an optically active material that can produce efficiently a necessary phase shift in the propagating signal for ultrafast all-optical signal processing.

The aforementioned advances have been made on multiple fronts. On the molecular front, successful prevention of spontaneous symmetry breaking and aggregation has allowed preservation the favorable discrete molecular properties in the bulk material environment. Specifically, we have demonstrated that molecular and material figures-of-merit can be improved greatly through judicious substitutions of different groups directly onto the polymethine dyes themselves.

On the material front, a method to improve the optical qualities of anionic polymethine/polymer blend films has been established. The solid-state miscibility of the dyes in polymer matrix was greatly improved by modifying the counterions, circumventing the problems of aggregation and phase-separation. We have also found a possible method to restrict the electronic structures of polymethines such that is less susceptible to the overall number density in the environment.

On the device integration front, the dispersion curve of a potential cladding material have been elucidated, providing the guidelines for cross-sectional dimensions that will ensure single mode propagation. In addition, using silane coupling chemistry to modify the surface energetics, the coverage and infiltration of micro- and nano-features of silicon-organic hybrid (SOH) constructs were improved.

The future advances will also likely be made in all three fronts. Owing to its well-known processing methods and high refractive index, our investigation of the molecular and material properties thus far has predominantly been focused on the optical properties of dyes in amorphous polycarbonate blends. The most recent experiments conducted in a different host medium, however, suggests that APC may not be the most optimized host material for certain dyes, hence opening up the possibility of additional host material search. Another direction that can improve the material response would be establishing a method to enable ordered structuring of molecules to combat the inevitable reduction in the nonlinear response due to orientational averaging in an isotropic medium.

For a more facile integration of nonlinear optical materials into SOH, a wider range of surface modifiers can be investigated in the search for a chemical moiety that would reduce the surface energy mismatch to a greater degree. The ultimate test of the effectiveness of any modification procedure is whether the micro- or nano-slots can be successfully infiltrated by an NLO material. For this purpose, development of a more comprehensive cross-sectional imaging technique would also greatly aid in the effort.

It is also important to remember that polymethines or other cyanine-like organic molecules are not the only optically active materials that show great potential for phase-

based AOSP devices. Semiconductor-chalcogenide composite glasses such as $\text{Ge}_{15}\text{As}_{31}\text{S}_{54}$ and $\text{Ge}_{11}\text{As}_{22}\text{Se}_{67}$ have been shown to possess large 2P-FOMs, as high as for 28, with sufficiently large n_2 of 3.3×10^{-18} and $1.3 \times 10^{-17} \text{ m}^2/\text{W}$ and low linear loss at $1.55 \mu\text{m}$. [160-162] However, the processing of these materials onto Si architectures requires flame sealing of the container in high vacuum and exposing the substrate at a high temperature (>800 degrees) for 24-hours long in a rocking furnace. A design of a more facile integration method for these chalcogenide glasses can also bring about an alternate solution to the silicon problem.

The combined efforts in the development of molecules and materials discussed in the thesis have culminated into a successful identification and optimization of the polymethines dyes and their polymer blends as an active cladding material for all-optical signal processing. With additional research efforts into engineering of these materials for greater film thickness and homogeneous slot infiltration, along with the fabrication of the SOH waveguides specifically tailored for single mode operation, a successful demonstration of on-chip AOSP at terahertz speed is very much an imminent prospect.

6.1 References

160. Andriesh, A., et al., *Applications of chalcogenide glasses in integrated and fiber optics (review)*. Quantum Electronics, 1986. **16**(6): p. 721-736.
161. Nasu, H. and J.D. Mackenzie, *Nonlinear optical properties of glasses and glass or gel-based composites*. Optical Engineering, 1987. **26**(2): p. 262102-262102-.
162. Prasad, A., et al., *Properties of $\text{Ge}_x\text{As}_y\text{Se}_{1-xy}$ glasses for all-optical signal processing*. Optics express, 2008. **16**(4): p. 2804-2815.

APPENDIX

A.1 Third-order Susceptibilities of Amorphous Polycarbonate

Throughout this thesis, the third-order nonlinearities of the guest chromophore–host polymer blends have been extracted under the hypothesis that host polymers make negligible contributions to the overall the $\chi^{(3)}$ responses of the blends. This approximation is a reasonable one since the absorption resonances of most visible and near IR transparent polymers fall < 350 nm. APC, however, shows linear absorption band that stretches out to 400 nm, and possesses a small but non-negligible overtone absorption peak at 1670 nm that corresponds to the transition between anharmonic vibrational levels.[163] In addition, while numerous investigations on active NLO polymer blends have been reported, and the $\chi^{(3)}$ of APC at 1.55 μm has never been reported to our knowledge. To assess the validity of the approximation, the third-order susceptibility of an isotropic APC was determined.



Figure A.1. 5 μm thick melt-processed APC disk used for Z-scan measurements

To determine n_2 , and the resulting $\chi^{(3)}$, a thick, 500 μm disc of APC was melt-processed. The thickness was controlled using a spacer as shown in the **Figure A.1**. Large sample thickness was required to ensure a sufficient nonlinear response from an otherwise seemingly transparent sample. The Z-scan was performed at an irradiance range that is close to 30 to 300 GW/cm^2 in 54 GW/cm^2 increment. The sample plots at 210 GW/cm^2 are shown in **Figure A.2**.

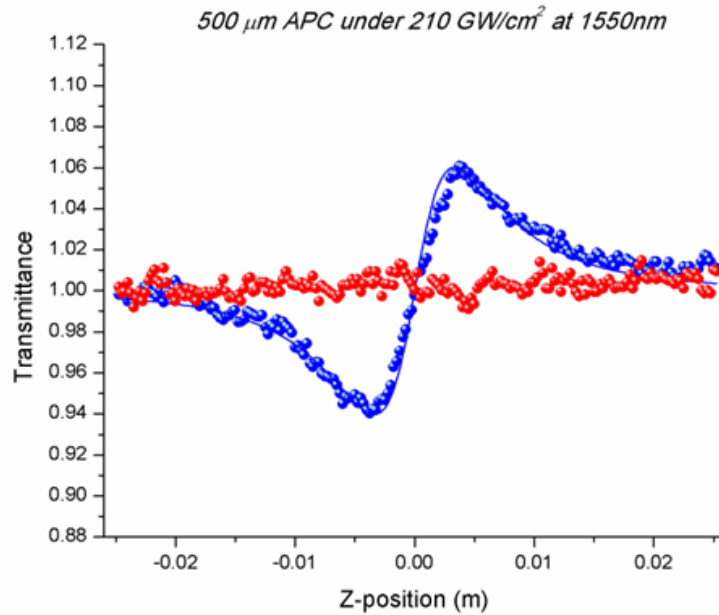


Figure A.2. Closed (following the division by open aperture scan) and open aperture Z-scans of 5 μm thick melt-processed APC disc 1550nm

Table A.1. Third-order nonlinearity of neat APC host polymer

	n_2 (m^2/W)	$\text{Re}(\chi^{(3)})$ (esu)
Amorphous Polycarbonate	1.06×10^{-19}	6.6×10^{-14}

The nonlinear refractive index of APC, while four times greater than that of the reference fused silica, exhibits a near-negligible level of contribution when compared to the overall $\chi^{(3)}$ of the dye/APC blends investigated in this thesis which have shown two to three orders of magnitude greater optical nonlinearity. (1.3×10^{-11} to 8.1×10^{-11} esu) Another polymer used in this thesis work, PMMA, could not be melt-processed into an optical quality thick disk due to emergence of small bubbles.

A.2 Third-Order Nonlinearities of Various Solvents in Liquid-core Optical Fibers (LCOF)

By detecting spectral broadening of pump laser via self-phase modulation in liquid-core optical fiber, the nonlinear refractive index, n_2 , of organic chromophores in solution can be measured. To extrapolate the n_2 contribution purely from the chromophores, the nonlinearities of the solvent systems must be known. Hence, Z-scans were performed on four different solvents used in LCOF applications.

Table A.2 Intensity-dependent refractive indexes and corresponding $\text{Re}(\chi^{(3)})$ s of solvents used in LCOF demonstration

	n_2 ($\times 10^{-20}$ m ² /W)	$\text{Re}(\chi^{(3)})$ ($\times 10^{-14}$ esu)
CCl₄	6.0	3.2
BrCCl₃	8.6	4.8
85:15% v/v BrCCl₃:CCl₄	6.8	3.6
CS₂	28	18

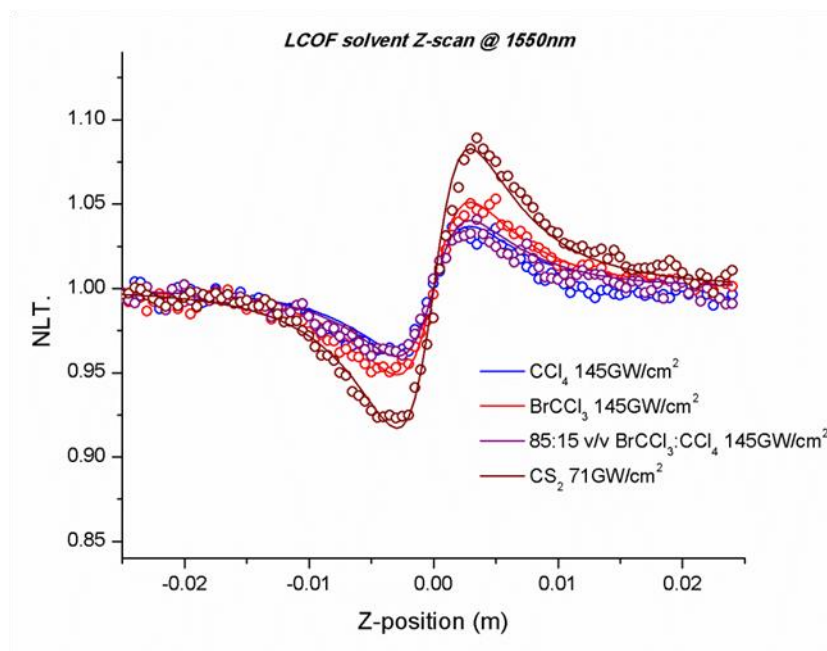


Figure A.3 Closed aperture Z-scans of various solvents

None of the solvents showed any open aperture response, hence the two-photon absorption coefficient, β , is considered vanishingly small. The nonlinearities of these solvents have never been reported with the exception of CS_2 whose n_2 at 0.532, 1.064, and 10.6 μm have been published.[88, 164] The nonlinear index n_2 of CS_2 is ca. $4 \times$ larger than other solvents. The n_2 of 85:15 v/v CCl_4 : BrCCl_3 behaves linearly with the solvent composition, indicating negligible solvent–solvent interaction. These values were published in Reference [165]

A.3 References

88. Sheik-Bahae, M., et al., *Sensitive measurement of optical nonlinearities using a single beam*. Quantum Electronics, IEEE Journal of, 1990. **26**(4): p. 760-769.
163. Mullen, P. and N. Searle, *The ultraviolet activation spectrum of polycarbonate*. Journal of applied polymer science, 1970. **14**(3): p. 765-776.
164. Ganeev, R., et al., *Nonlinear refraction in CS₂*. Applied Physics B, 2004. **78**(3-4): p. 433-438.
165. Shahin, S., et al., *Third-order nonlinear optical characterization of organic chromophores using liquid-core optical fibers*. JOSA B, 2014. **31**(10): p. 2455-2459.

VITA

HYEONGEU (ANSELMO) KIM

Anselmo Kim was born in Seoul, Korea. His family moved to New York suburb in 1993. He received his bachelor's degree from the City College of New York in 2007 before moving to Atlanta to obtain PhD in chemistry from Georgia Tech in the fall of 2008. He is investigating nonlinear optical properties of highly polarizable π -conjugated materials, and developing methods to integrate these candidate materials into photonic devices for all-optical signal processing (AOSP) application. He works closely in conjunction with researchers in collaborating groups at various institutions including Georgia Tech, U. Washington, U. Arizona, UCF and Cornell. Outside research, his passion is in motorsports as he spends most of his free time on high performance driving, and working on cars.